First ground based FTIR-TCCON measurements of CO2 in a European megacity : comparison with a rural site and validation of satellite measurements

Dmitry Koshelev

THÈSE DE DOCTORAT
DE SORBONNE UNIVERSITÉ

Spécialité : Physique

École doctorale : "Physique en Île-de-France"

réalisée

au Laboratoire d'Études du Rayonnement et de la Matière en Astrophysique et Atmosphères

présentée par

Dmitry KOSHELEV

pour obtenir le grade de :

DOCTEUR DE SORBONNE UNIVERSITÉ

Sujet de la thèse :

First ground based FTIR-TCCON measurements of CO_2 in a European megacity: comparison with a rural site and validation of satellite measurements

soutenue le 11ème Octobre 2018

devant le jury composé de :

Mme	ROTGER Maud	Rapporteur
M.	WARNEKE Thorsten	Rapporteur
M.	RAMONET Michel	Examinateur
Mme	DE MAZIERE Martine	Examinateur
Mme	PICON Laurence	Examinateur
M.	JANSSEN Christof	Directeur de thèse

Contents

I – Introduction

I.1 The Earth's atmosphere

The Earth's atmosphere is a thin layer of gases covering the Earth. The atmosphere can be divided into different layers determined by the vertical temperature profile and the associated temperature gradient (Fig.I.1).

The first atmospheric layer from the ground which exhibits a negative temperature gradient is the troposphere. It contains ∼75% of the atmospheric mass and is well mixed by convection. The major part of solar radiation heats the surface of the Earth and this, in turn,

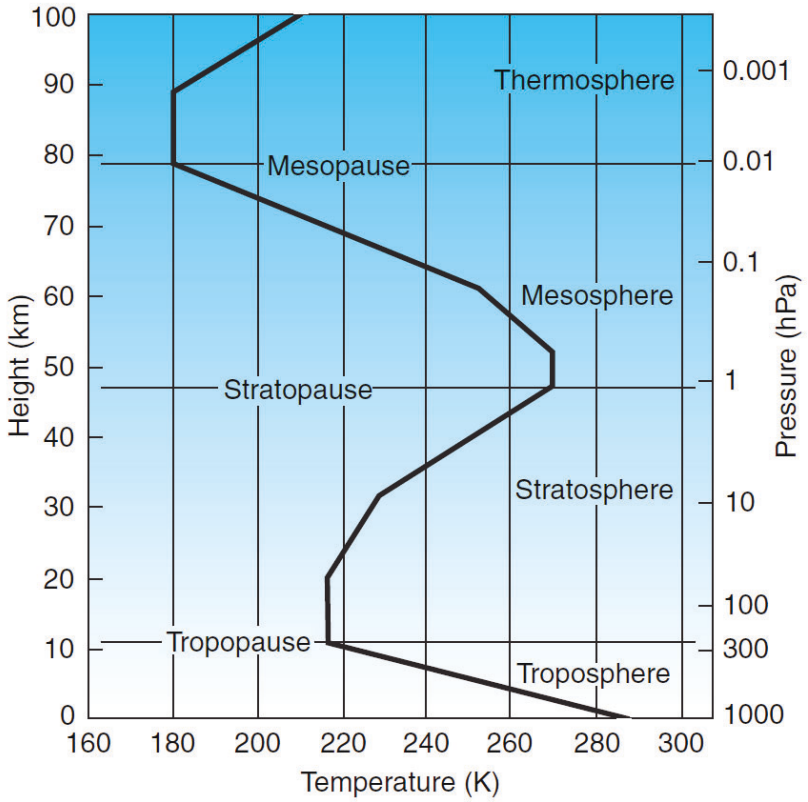

Figure I.1 – Structure of the Earth's atmosphere specified through the vertical temperature profile. Source: [1]

heats the directly overlying air, causing the convective mixing of the troposphere. The top of the troposphere is called tropopause (8-18 km, depending on the season and the latitude) where the temperature gradient (dT/dz) is zero. Between the tropopause and stratopause (50 km), the atmosphere is heated by the absorption of ultraviolet (UV) radiation by oxygen (O_2) and ozone (O_3), leading to a positive temperature gradient, is called the stratosphere. The next layer is mesosphere, characterised by a negative temperature gradient. The upper layer of the atmosphere is called thermosphere. It absorbs UV radiation of wavelength up to 175 nm above the mesopause (80-90 km) leading to ionisation and heating of the atmosphere. It is characterised by a positive temperature gradient with temperature reaching 1700°C at the height of 500 km.

The atmosphere is the smallest of the Earth's geological reservoirs. The mass of the atmosphere is 0.005×10^{21} kg, which may be compared to the second smallest reservoir hydrosphere which has a mass of 2.4×10^{21} kg. The dry air of atmosphere consists mostly of nitrogen (N_2, 78.08%) and oxygen (O_2, 20.95%). The remaining 0.97% of gases are called trace gases, which are argon (Ar, 0.93%), carbon dioxide (CO_2), neon (Ne), helium (He), methane (CH_4) and others. The amount of water (H_2O) in the atmosphere varies between 0 and 4% and depends on season and geographical location.

The atmosphere could also be separated into two layers: homosphere and heterosphere defined by the composition of air. The homosphere is a layer between the ground and 95 km, where the relative composition of the main gases (N_2, O_2 and Ar) does not change with altitude. It includes the troposphere, stratosphere, mesosphere, and the lowest part of the thermosphere. In the heterosphere (above 95 km) along with N_2 and O_2 molecules, there are atomic N and O, and the relative composition of the main gases changes with altitude. The transmission region between the homosphere and heterosphere is called turbopause.

The Earth's atmosphere is a key for life, it protects the surface from harmful UV radiation, and it leads to the greenhouse effect.

I.2 Greenhouse effect

To understand the greenhouse effect caused by the presence of the atmosphere, first, let's consider the Earth without the atmosphere. The incoming solar radiant power Φ on Earth is given by the solar constant ($G_{SC} = 1.3608$ kW/m^2) multiplied by Earth's cross Section:

$$\Phi = \pi R_E^2 \cdot G_{SC} = 173.4 \cdot 10^{15} \text{ W}$$

where $R_E = 6371$ km is the Earth's radius. Dividing Φ by the external surface of the Earth ($4\pi R_E^2$), we get the daily averaged power received by the Earth per surface which is equal to

$$j_{\text{received}} = \frac{\Phi}{4\pi R_E^2} = 340 \text{ W/m}^2 \tag{I.1}$$

Let's consider a thermodynamic equilibrium and the Earth as a black body. The amount of received and emitted energy should be in balance. The power radiated from the Earth is given by the Stefan-Boltzmann law:

$$j_{\text{radiated}} = \epsilon \sigma T_E^4 \tag{I.2}$$

where $\sigma = 5.6703 \times 10^{-8}$ $\mathrm{Wm^{-2}K^{-4}}$ is the Stefan Boltzmann constant, T_E is the temperature of the Earth and ϵ is emissivity ($\epsilon = 1$ for a black body). Then the Earth's black body temperature can be calculated by combining Eq.(I.1) and Eq.(I.2):

$$T_E = \sqrt[4]{\frac{G_{SC}}{4\sigma}} = 278.28 \text{ K } (4.85°\text{C})$$

Since the Earth has an albedo of about 0.3, meaning that 30% of the solar radiation is scattered back into space without absorption, the solar power absorbed by the Earth is $0.7 \times 343 = 240.1$ $\mathrm{W/m^2}$ (instead of 343 $\mathrm{W/m^2}$) and the Earth's temperature is equal to 254.5 K (-19.15 °C). The real Earth's surface temperature is 288 K (15 °C) which is much higher than 254.5 K. The difference of 33.5 °C is caused by the presence of the atmosphere.

The Earth is much colder (288 K) than the Sun (5778 K), it radiates at much longer wavelengths ($\lambda_{max} = b/T$, - Wien's displacement law, b is the Wien's displacement constant), essentially in the infrared part of the spectrum. Most of this thermal radiation emitted by the land and ocean is absorbed by the atmosphere, including clouds, and reradiated in all directions. Part of this radiation goes into space and part goes back to the Earth. This process conserves energy and increases the Earth's temperature and is called the greenhouse effect. Without the greenhouse effect, the average temperature at Earth's surface would be below the freezing point of water. Thus, Earth's greenhouse effect makes life as we know it possible.

The atmospheric gases that absorb and emit energy in infrared (IR) spectral regions are called greenhouse gases (GHGs). The major atmospheric absorbers are H_2O, CO_2, CH_4, O_3

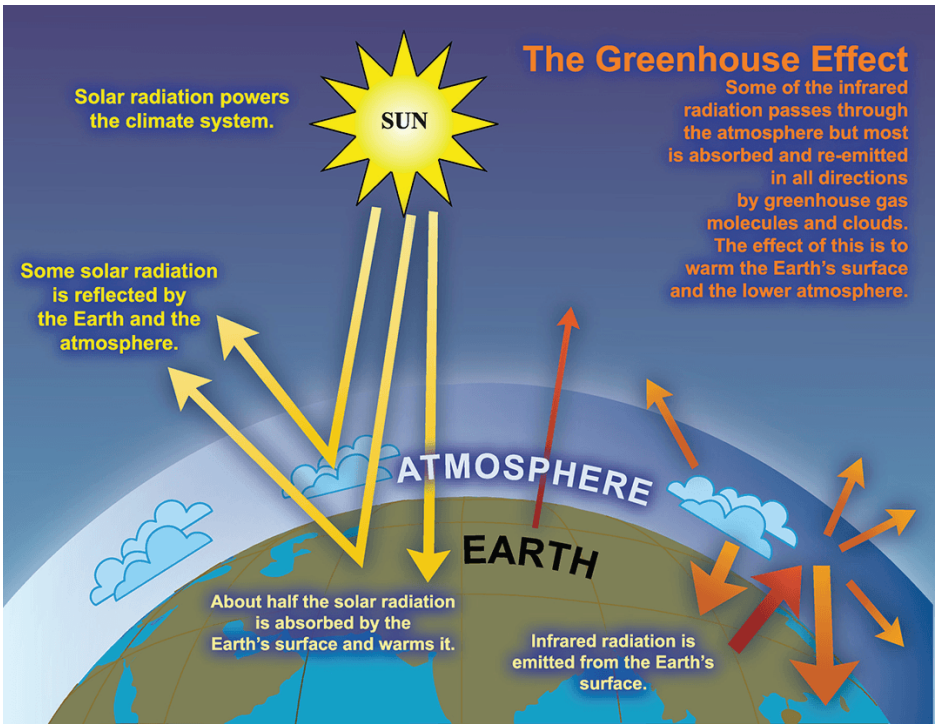

Figure I.2 – A schematic representation of the greenhouse effect. Source: [2], page 115.

and N_2O. In the atmosphere, H_2O is presented as water vapour and clouds (condensed water in ice and liquid forms). The radiative effect of H_2O (water vapour and clouds) and CO_2 (consider that other absorbers do not absorb) overall greenhouse effect is 95.1% [3]. CO_2 is the second most important gas contributing to the greenhouse effect.

Anthropogenic Greenhouse effect

Human activities, essentially the burning of fossil fuels and deforestation, have greatly intensified the greenhouse effect. Since the industrial revolution, CO_2 concentrations raised from 280 ppm in 1750 to 410 ppm in 2018 (see Section I.3.2). The CO_2 growth rate will be doubled within the next 50-100 years, referred to pre-industrial concentrations [4].

Adding more of greenhouse gases (for example CO_2) to the atmosphere intensifies the greenhouse effect, thereby warming Earth's climate. The amount of warming depends on various feedback mechanisms. For example, as the atmosphere warms due to rising levels of greenhouse gases, its concentration of water vapour increases, further intensifying the greenhouse effect. This causes more warming, which causes an additional increase in water vapour, in a self-reinforcing cycle. This water vapour feedback may be strong enough to approximately double the greenhouse effect due to the added CO_2 alone [2].

I.3 Carbon cycle

The carbon cycle is a complex of processes by which carbon is exchanged between different geochemical reservoirs. In the atmosphere, carbon is presented in two main forms: carbon dioxide (CO_2) and methane (CH_4).

I.3.1 Natural and anthropogenic sources and sinks

There are three primary sources and sinks for atmospheric CO_2: the land biosphere, the oceans and anthropogenic emissions from the burning of fossil fuels and other industrial activities. The land biosphere and the ocean reservoirs exchange CO_2 with the atmosphere in a balanced two-way transfer.

The land biosphere

In pristine conditions the land and the atmosphere reservoirs exchange around 120 GtC (Gigatons of Carbon) per year [2]. It is a two-way exchange. During one year 120 GtC move from the land to the atmosphere and the same amount from the atmosphere to the land. In spring and summer, when plants actively absorb atmospheric CO_2 during the photosynthesis process, there is a net flux of carbon from air to ground:

$$6\,CO_2 + 6\,H_2O \longrightarrow C_6H_{12}O_6 + 6\,O_2$$

In the reverse reaction of respiration and decay, carbon is released back into the atmosphere.

By contrast, in fall, spring and winter, when the respiration and decomposition of plants predominate over the processes of photosynthesis the net flux is into the air. Averaged over the year there is no net flux in either direction. The seasonal asymmetry in the up and down CO_2 fluxes explains the seasonal cycle of atmospheric CO_2. The amplitude of

seasonal variation tends to be greater in the northern hemisphere compared with the southern hemisphere because of the greater land area in the northern hemisphere.

Human activities in burning fossil fuel are primarily responsible for the annual increase in atmospheric CO_2, while biologically induced exchanges determine the seasonal pattern.

The oceans

As the land biosphere, the oceans also exchange large amounts of CO_2 with the atmosphere each year. In the unpolluted environment, the air to sea and sea to air fluxes are globally balanced, with about 90 GtC moving in both directions every year [2]. These up and down fluxes are driven by changes in the temperature of the surface water of the oceans, which alter the ocean's ability to dissolve CO_2, as well as by biological consumption and production of the gas resulting from photosynthesis and respiration/decomposition processes in near-surface waters. When dissolved in water, carbon dioxide reacts with water molecules and forms carbonic acid, which contributes to ocean acidity. It can then be absorbed by rocks through weathering. It also can acidify other surfaces it touches or be washed into the ocean. All of these processes can vary both seasonally and spatially by significant degrees. In general, the tropical oceans are net sources of CO_2 to the atmosphere, whereas at higher and particularly polar latitudes the oceans are a net sink.

I.3.2 The atmospheric record

The atmospheric concentration of CO_2 fluctuates slightly with the seasons, for the Northern Hemisphere it diminishes during the spring and summer as plants consume the gas and it rises during autumn and winter as plants go dormant or die and decay. The concentration also varies on a regional basis, most strongly near the ground with much smaller variations aloft. In urban areas concentrations are generally higher and indoors they can reach ten times background levels due to human respiration.

Figure I.3 shows values of the atmospheric concentration of CO_2 measured at Mauna Loa Observatory (Hawaii) from the late 1950s to up today. Over this period annual average of CO_2 has increased by 30% from 314.6 ppm in 1958 to 408.5 ppm in 2018. The extraction and analysis of bubbles of air trapped in ice cores collected from the polar ice-caps allow extending the CO_2 record up to 800 000 years b.c. (Fig. I.4). For 800 000 years, the CO_2 concentration did not increase above the 300 ppm value before the industrial revolution began.

Increases in atmospheric concentrations of CO_2 and other long-lived greenhouse gases such as methane, nitrous oxide and ozone have correspondingly strengthened their absorption and emission of infrared radiation, causing the rise in average global temperature. Carbon dioxide is of greatest concern because it exerts a larger overall warming potential than all of other gases combined (except H_2O) [3].

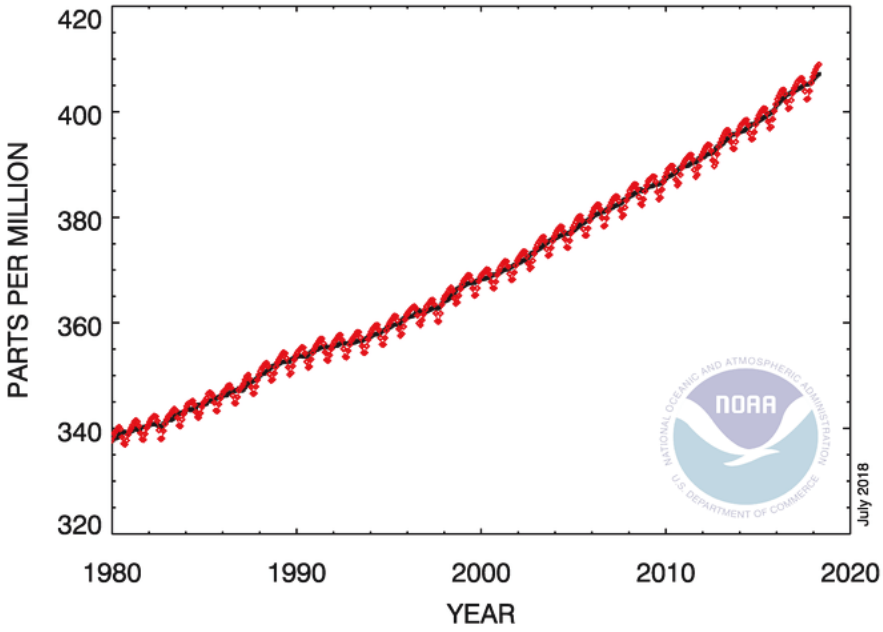

Figure I.3 – Atmospheric CO_2 time series recorded at Mauna Loa Observatory. - Source :[1]

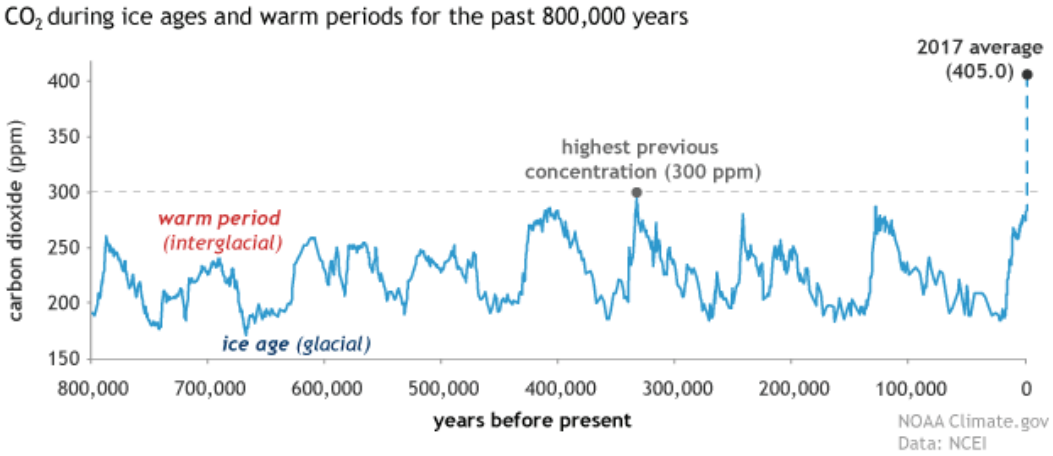

Figure I.4 – Atmospheric CO_2 record for the past 800000 years, based on ice core data. - Source :[2]

I.3.3 Anthropogenic CO_2 emissions

The concentration of CO_2 is mainly rising due to human activities [5]. CO_2 is the primary anthropogenic greenhouse gas released into the atmosphere due to fossil fuel combustion and land use. Fossil fuel combustion has a more significant contribution to historical emissions

[1] Source : https://www.esrl.noaa.gov/gmd/ccgg/trends/full.html
[2] Source : https://www.climate.gov

than the land use, accounting for ∼80% of anthropogenic CO_2 emissions. CO_2 emissions from fossil fuel combustion is about 8.7 GtC per year (in 2008 [5]).

Increasing concentrations of atmospheric greenhouse gases cause an increase in mean surface temperatures. Such an increase in mean surface temperature and associated climate variables such as precipitation could have a profound impact on ecosystems and human society.

Global networks are required to monitor the concentrations increase and to identify sources and sinks in order to understand global climate change. One such network is the international Total Carbon Column Observing Network.

I.4 TCCON network

The Total Carbon Column Observing Network (TCCON) is an international network (see Fig.I.5) of ground-based Fourier transform spectrometers (FTS) that measure column-averaged dry-air mole fractions of CO_2, CH_4, CO, N_2O, H_2O, HDO, and HF to the scientific and satellite validation communities [6]. The first TCCON dedicated instrument, located at Park Falls, WI, USA, was installed in May, 2004. Each TCCON site is outfitted with a solar tracker that actively tracks the centre of the sun and uses a Bruker IFS 125 HR to record interferograms in the near infrared.

The TCCON data is used for scientific investigations of the carbon cycle [7–13] and in the retrieval algorithm development and validation of satellite measurements [14–20].

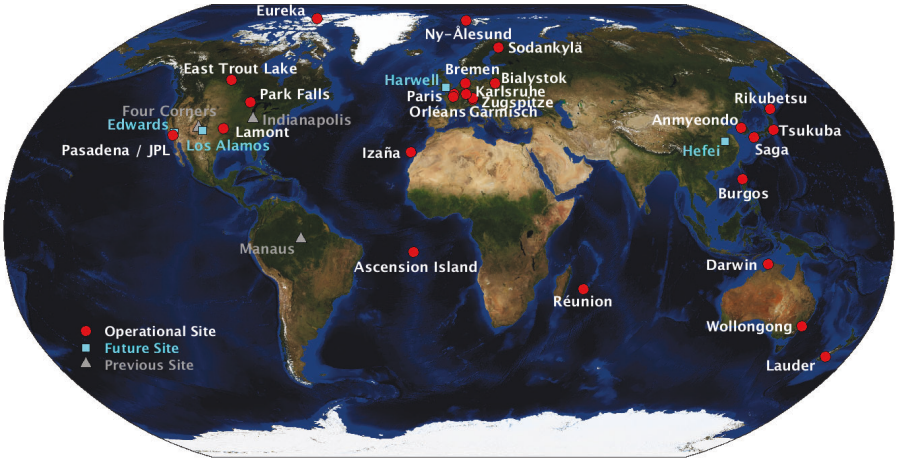

Figure I.5 – A map showing the locations of the TCCON stations. - Source :[3]

[3]Source : https://tccon-wiki.caltech.edu/

I.5 Outline of the thesis

TCCON-Paris is the first European TCCON site located in the centre of the megacity. This work is dedicated to the description of all activities of the TCCON-Paris site. Chapter 2 describes the FTIR principles and the TCCON-Paris instrumentation. The instrument performance is given in great details. The Instrumental Line Shape (ILS) of the spectrometer is studied by using HCl low pressure cell. For the interferometer alignment, we propose a new scheme for the observation of Haidinger fringes without using an external telescope.

In chapter 3, N_2O cell blind intercomparison exercise is described. The purpose of the exercise is to find a new stable gas cell. The results of our analysis has helped to identify an error in the reference measurements, which decreases the bias in the N_2O column between the Paris instrument and the reference measurement. The instrument stability is investigated by using the Allan variance approach on 1000 N_2O transmission spectra.

In chapter 4, a brief description of the radiative transfer and the inversion theory of C. D. Rodgers are given. The official TCCON retrieval package GGG is described in details. Chapter 5 describes the official data product of the TCCON-Paris site. We compare the precision of X_{CO_2} measurements of TCCON-Paris with other TCCON sites and improvements that have been made to improve the precision.

Chapter 6 discusses the accuracy of the TCCON-Paris measurements in the condition of the polluted boundary layer in Paris. The key idea of this study is to associate a model and real measurements (in situ and LIDAR) to generate a better suited a priori profiles of CO_2. A presumable impact on the validation of OCO-2 satellite mission is discussed.

Chapter 7 describes two short campaigns of collocated measurements of EM27/SUN (low resolution portable FTS) and TCCON. In the first campaign the EM27/SUN is used as transferable reference between TCCON-Orleans and TCCON-Paris. In the second campaign we compare TCCON-Paris operating at high and low resolutions with EM27/SUN.

II – Description of the TCCON-Paris instrument

The TCCON-Paris instrument consists of two main parts: the Bruker IFS 125HR FTIR spectrometer (denoted as Bruker 125HR) and the solar tracker. The theoretical basis of the FTIR spectroscopy is given in Section II.1 and is mainly based on [21]. The Bruker 125HR and the solar tracker are described in Section II.2. The instrumental line shape measurements of Bruker 125HR by the use of sealed HCl gas cell is presented in Section II.3. Section II.4 describes the interferometer alignment procedure and proposes a new system for the observation of Haidinger fringes.

II.1 FTIR principles

II.1.1 The Michelson interferometer

The main part of the Bruker 125HR is a Michelson interferometer. A scheme of the Michelson interferometer and its collimating system are shown in Fig.II.1. Collimated light enters the interferometer and is partially reflected by an ideal beamsplitter (point O) to the fixed mirror (point F) and partially transmitted to the movable mirror (point M). Both mirrors are considered to be perfect. After the reflection by fixed and movable mirrors, both beams travel back and are recombined at the beamsplitter with an introduced optical path difference (OPD) equal to $2(OM - OF) = \delta$. One part of the recombined beam then goes in the source direction and one part goes to the detector where it is converted into an electrical signal.

Let the plane incident wave be $A_0 e^{i\omega t - i2\pi\tilde{\nu}x}$, where A_0 is the peak amplitude of the source, $\omega = 2\pi f$, where f is a wave frequency, $\tilde{\nu} = \frac{1}{\lambda}$ is the wavenumber, where λ is wavelength and x is the traveled distance. In the case of perfectly collimated beam the amplitude of light in the direction of detector is:

$$A_{det} = \varepsilon A_0 e^{i\omega t}(e^{-i2\pi\tilde{\nu}D_1} + e^{-i2\pi\tilde{\nu}D_2})$$

where $D_1 = 2OF$ and $D_2 = 2OM$ are the distances travelled by each of the beams and ε is the beamsplitter efficiency (transmittance multiplied by reflectance). The energy reaching the detector is

$$E_{det} = |A_{det}|^2 = 2A_0^2|\varepsilon|^2(1 + cos(2\pi\tilde{\nu}(D_2 - D_1)))$$

The intensity at the detector depends on the difference $D_2 - D_1$, which is the optical path difference δ, defined above. The intensity of the beam at the detector is measured as a

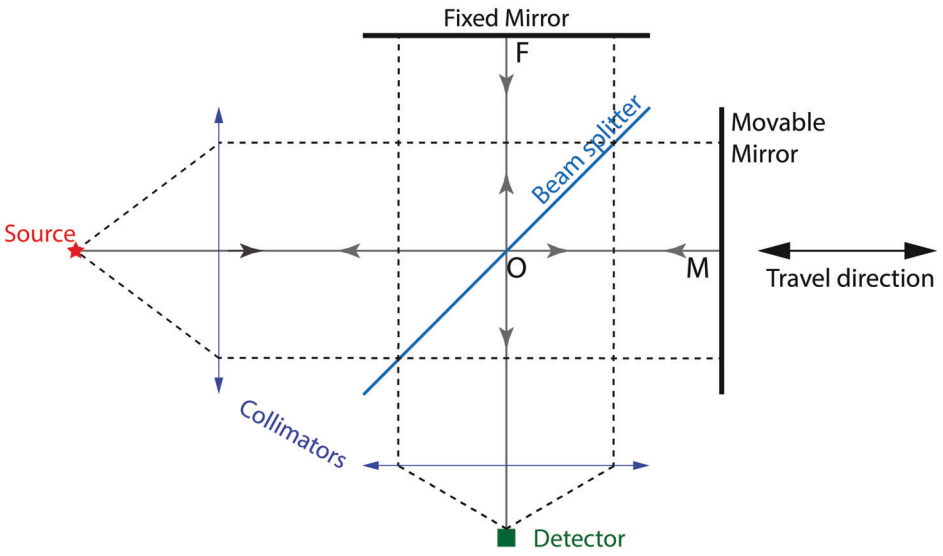

Figure II.1 – Schematic representation of the Michelson interferometer.

function of δ and is called an **interference pattern**. The varying part of the interference pattern (AC) called **interferogram**, $I(\delta)$, is given by

$$I(\delta) = 2A_0^2|\varepsilon|^2 cos(2\pi\tilde{\nu}\delta)$$

If the light source is not monochromatic but a continuum source of radiation, the interferogram is given by integration over all wavenumbers $\tilde{\nu}$:

$$I(\delta) = \int_{-\infty}^{\infty} S(\tilde{\nu}) cos(2\pi\tilde{\nu}\delta) d\tilde{\nu}$$

where $S(\tilde{\nu})$ is the intensity of the light source ($B(\tilde{\nu})$) modified by spectrometer characteristics: $S(\tilde{\nu}) = H(\tilde{\nu})B(\tilde{\nu})$, where $H(\tilde{\nu})$ is an instrument characteristics including beamsplitter efficiency, detector response, mirrors reflectivity and other. The recovery of the spectra is then achieved by taking the inverse Fourier transform (F^{-1}):

$$S(\tilde{\nu}) = \mathrm{Re}(F^{-1}(I(\delta))) = \int_{-\infty}^{\infty} I(\delta) cos(2\pi\tilde{\nu}\delta) d\tilde{\nu} \tag{II.1}$$

Or, when written in the transcendental exponential form:

$$I(\delta) = \mathcal{F}(S(\tilde{\nu})) = \int_{-\infty}^{\infty} S(\tilde{\nu}) e^{-i2\pi\tilde{\nu}\delta} d\tilde{\nu} \tag{II.2}$$

$$S(\tilde{\nu}) = \mathcal{F}^{-1}(I(\delta)) = \int_{-\infty}^{\infty} I(\delta) e^{i2\pi\tilde{\nu}\delta} d\delta \tag{II.3}$$

where $\mathcal{F}$ is the complex Fourier transform, $\mathcal{F}^{-1}$ is the complex inverse Fourier transform.

II.1.2 Effect of finite retardation

So far we have discussed the ideal instrument, in practice, the optical path difference (δ) is limited by the value $\delta_{max} = \Delta$ (maximum path difference) determined by the interferometer design. The effect of measuring the signal over a limited retardation can be mathematically described as a multiplication of the infinite interferogram $\mathrm{I}_{inf}(\delta)$ by a boxcar truncation function $D(\delta)$

$$D(\delta) = \begin{cases} 1 & \text{if } \delta \leq |\Delta| \\ 0 & \text{else} \end{cases}$$

By using Eq.(II.1), the measured spectrum in this case can be presented by

$$\begin{aligned} S(\tilde{\nu}) &= \mathcal{F}^{-1}(I(\delta) \cdot D(\delta)) \\ &= \mathcal{F}^{-1}(I(\delta)) \otimes \mathcal{F}^{-1}(D(\delta)) \\ &= S_{inf}(\tilde{\nu}) \otimes f(\tilde{\nu}) \\ &= S_{inf}(\tilde{\nu}) \otimes 2\Delta\,\mathrm{sinc}(2\pi\tilde{\nu}\Delta) \end{aligned}$$

where $\otimes$ is the convolution operator and $\mathrm{sinc}(x) = \sin(x)/x$. The inverse Fourier transformation of the boxcar function $D(\delta)$ is equal to $f(\tilde{\nu}) = 2\Delta\mathrm{sinc}(2\pi\tilde{\nu}\Delta)$. $f(\tilde{\nu})$ is called **instrumental line shape** (ILS) function. The convolution of the single spectral line ($B(\tilde{\nu}_1)$) with the ILS sinc function gives

$$S(\tilde{\nu}) = 2\Delta B(\tilde{\nu}_1)\,\mathrm{sinc}\,2\pi(\tilde{\nu}_1 - \tilde{\nu})\Delta$$

This function is shown in Fig.II.2. The width of the sinc-function defines the spectral resolution, where the full width at half maximum (FWHM) is $0.6035/\Delta$.

However, the sinc function may not always be convenient for infrared spectroscopy applications due to its fairly large amplitudes at wavenumber well away from $\tilde{\nu}_1$. The first

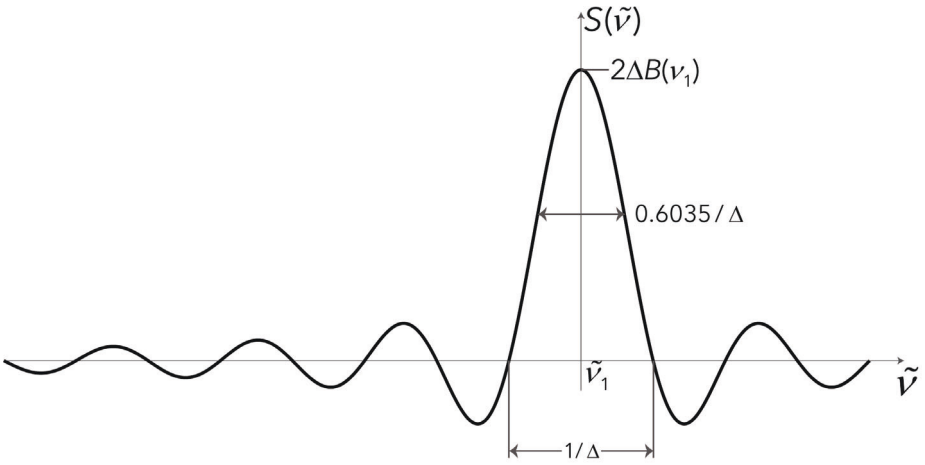

Figure II.2 – Fourier transform of the sinusoidal interferogram generated by a monochromatic line at wavenumber $\tilde{\nu}_1$ and truncated by Δ.

minimum reaches below zero by an amount that is 22% of the height at $\tilde{\nu}_1$. If a second weak line happened to be present in the spectrum at the wavenumber of this minimum, it would not be seen in the computed spectrum. One method to circumvent the problem of these secondary minima is the use of **apodization** procedure.

II.1.3 Apodization

If instead of using the boxcar function we use a simple triangular truncation function $A_1(\delta)$

$$A_1(\delta) = \begin{cases} 1 - |\frac{\delta}{\Delta}| & \text{if } \delta \leq |\Delta| \\ 0 & \text{else} \end{cases}$$

the $f_1(\tilde{\nu})$ function would be the Fourier transform of $A_1(\delta)$:

$$f_1(\tilde{\nu}) = \mathcal{F}^{-1}(A_1(\delta)) = \Delta \text{sinc}^2(\pi\tilde{\nu}\Delta)$$

It is shown in Fig.II.3 (c).

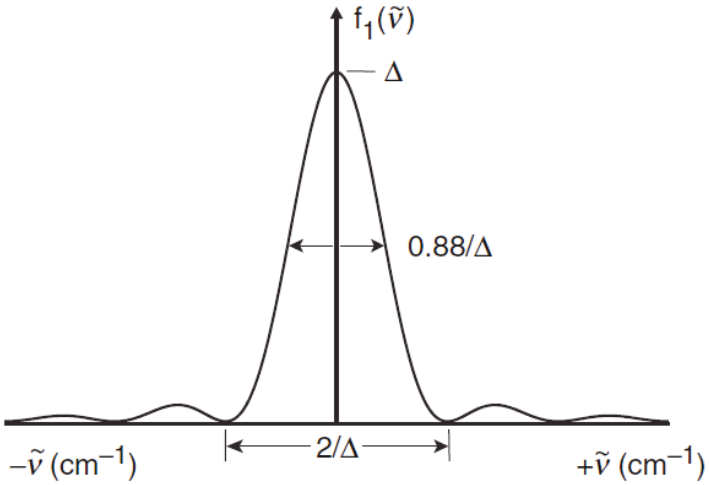

Figure II.3 – The sinc^2 ILS computed for a triangularly apodized interferogram. Source: [21]

When the interferogram is not apodized, the lines will have a sinc shape. Triangular apodization leads to the lines shape to be sinc^2. The set of commonly used apodization function and corresponding ILS are presented on Fig.II.4.

In general, it is advisable to use some type of apodization for FTIR spectrometry when the spectrum contains features that are narrower than the nominal resolution. When the bandwidths of the spectral lines are broader than the resolution, apodization serves as a smoothing function but otherwise degrades the spectral quality, because of the loss in resolution.

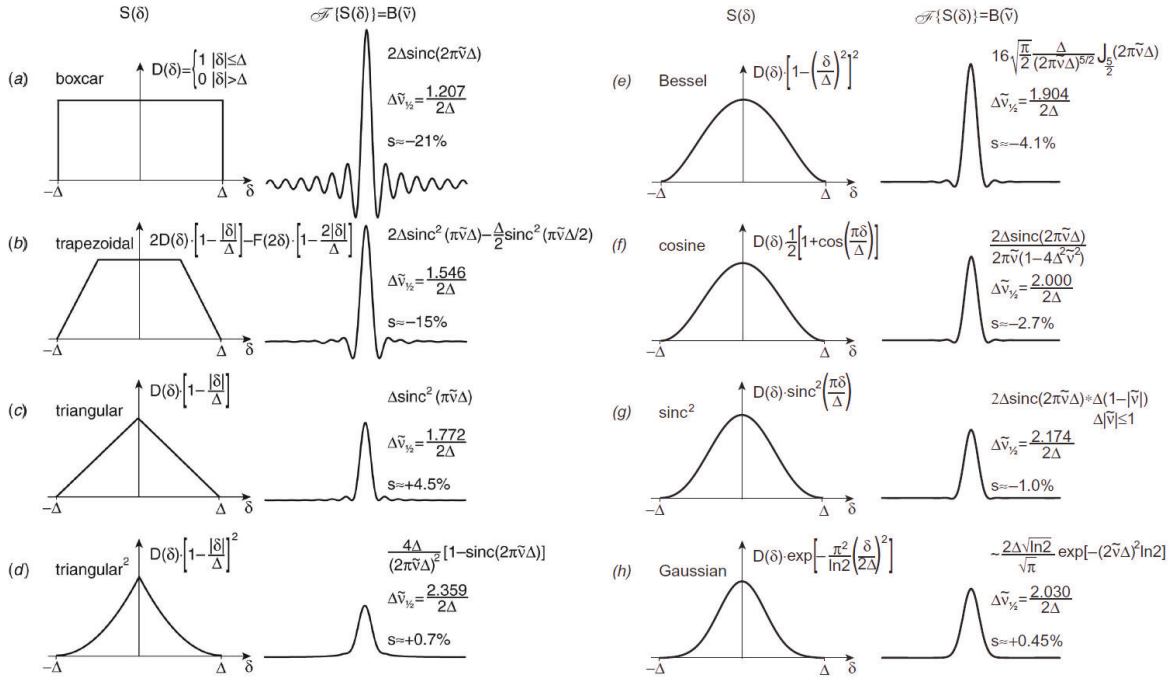

Figure II.4 – Series of apodization functions and their corresponding instrumental line shape functions: In each case the equations representing the shapes of the apodization and ILS functions are given, together with the FWHM ($\Delta\tilde{\nu}_{1/2}$, and the amplitude of the largest sidelobe (s), as percentage of the maximum excursion. Source: [21]

Self-Apodization

The beam that passes through the interferometer should be perfectly collimated. A perfectly collimated beam can be created by using a source of infinitely small size that would lead to no signal measured by the detector otherwise the source must have infinite brightness. In practice the source has a finite size and the beam is not collimated perfectly.

In order to investigate the effect of imperfect collimation, we consider the effect of a non-collimated beam of monochromatic light of wavelength λ passing through the interferometer with a divergence of half-angle α. The path difference Δ for the off axis ray introduced by the displacement l of movable mirror is equal to

$$\Delta = 2l\cos\alpha$$

The path difference (x) between the central (on axis) and off axis rays is

$$x = \Delta = 2l(1-\cos\alpha) \approx l\alpha^2$$

With increasing l, the path difference x between central and off axis rays could achieve $1/2\lambda$ when two rays are out of phase and the interferogram has no information at the central part of the source image:

$$l\alpha^2 = \frac{1}{2}\lambda = \frac{1}{2\tilde{\nu}}$$

Displacement l gives the retardation of $2l$ with the highest resolution $\Delta\tilde{\nu}$ defined as $\frac{0.6035}{2l}$ (for boxcar truncation function), defining the maximum value of half angle α_{max}

$$\alpha_{max} = \sqrt{\frac{1}{\tilde{\nu}2l}} = \sqrt{\frac{\Delta\tilde{\nu}}{0.6035\tilde{\nu}}}$$

To achieve the resolution of $\Delta\tilde{\nu}$ at all wavenumbers between 0 and $\tilde{\nu}$, the values of half angle α should be less than α_{max}.

II.1.4 Discrete interferogram sampling

The recorded interferogram is neither infinite nor continuous. Instead, it is sampled discretely at a constant retardation interval (h, cm) determined by the Nyquist criterion: if the signal is digitized with a small enough interval between data points, no information from the analog signal is lost. The maximum sampling interval h is given by

$$2h = (\tilde{\nu}_{max} - \tilde{\nu}_{min})^{-1}$$

where $\tilde{\nu}_{max}$ and $\tilde{\nu}_{min}$ are the highest and the lowest wavenumbers that reach the detector.

Let the retardation at any sampling point be given by kh, where k is an integer, and let I_k be the value of the interferogram measured at this point. Then, we can replace the integral of equation (II.3) by a summation:

$$S(\tilde{\nu}) = \sum_{k=1}^{N} I_k e^{-i2\pi\tilde{\nu}kh}$$

where N is the total number of measured points.

II.1.5 Phase correction

When a recorded interferogram is transformed to produce a spectrum, there could be errors caused by the zero path difference position determination due to the interferogram sampling and by the electronic filters. The measured interferogram $I(\delta)$ is transformed into a spectrum $S'(\tilde{\nu})$ by the Fourier transform (Eq.II.3). $S'(\tilde{\nu})$ is a complex function that could be presented as a sum of real and imaginary parts:

$$S'(\tilde{\nu}) = \mathrm{Re}(S'(\tilde{\nu})) + i\mathrm{Im}(S'(\tilde{\nu}))$$

or with the use of exponential form:

$$S'(\tilde{\nu}) = \sqrt{\mathrm{Re}(S'(\tilde{\nu}))^2 + \mathrm{Im}(S'(\tilde{\nu}))^2} \cdot e^{i\theta_{\tilde{\nu}}} = |S'(\tilde{\nu})| \cdot e^{i\theta_{\tilde{\nu}}}$$

where $\theta_{\tilde{\nu}} = \arctan(\mathrm{Im}(S'(\tilde{\nu}))/\mathrm{Re}(S'(\tilde{\nu})))$ is a phase angle. The complex spectrum $S'(\tilde{\nu})$ contains all the spectral information, but it lies in complex manifold. The spectrum magnitude $|S'(\tilde{\nu})|$ is a real (in the complex sense) representation of the spectrum, but it is only an absolute value of that representation. The object of the phase correction is to produce the true spectrum $S(\tilde{\nu})$. For the phase correction procedure the phase angle is calculated with the use of low resolution spectrum (only the part of interferogram which is close to zero path

difference is used) in order to have less structure and variation (caused by absorption lines). The true spectrum $S(\tilde{\nu})$ contains only the real terms, and is calculated by

$$S(\tilde{\nu}) = \mathrm{Re}(S'(\tilde{\nu}) \cdot e^{-i\theta_{\tilde{\nu}}}) = \mathrm{Re}(S'(\tilde{\nu}))\cos\theta_{\tilde{\nu}} + \mathrm{Im}(S'(\tilde{\nu}))\sin\theta_{\tilde{\nu}} \tag{II.4}$$

Eq.(II.4) represents a phase correction algorithm.

II.2 TCCON-Paris instrumentation

The TCCON-Paris site uses a typical TCCON configuration for the measurements and analysis of solar absorption spectra. The TCCON-Paris instrument consists of two main components: high resolution spectrometer Bruker 125HR, described in Section II.2.1 and a solar tracker, described in Section II.2.2. The station also includes the standard meteorological measurements of pressure, temperature, humidity, wind speed and direction. The pressure measurements are performed with a barometer, which is regularly calibrated by the French National Metrology Laboratory (LNE).

II.2.1 Bruker 125HR

Bruker 125HR is a commercial high resolution spectrometer, manufactured by Bruker company (www.bruker.com). The spectrometer consists of the following main compartments: source, interferometer, sample and detector compartments (see Fig.II.5). The configuration of different Bruker 125HR can slightly differ. For example, another arrangement of compartments that does not affect the recorded spectra, or the absence of source or sample compartments.

Figure II.5 – A top view of the TCCON-Paris spectrometer. Different compartments are coloured in different colours: grey - source compartment, violet - interferometer compartment, green - sample compartment and blue - detector compartment.

a) Source compartment

The source compartment can operate in two modes: the first mode uses internal built-in light sources and the second mode uses an external light source (solar radiation), Fig.II.6. In both modes the light is focused on an aperture wheel. The aperture wheel contains circular holes of different diameter ranging from 0.5 to 12.5 mm. A switch between two modes is triggered by a movable mirror. There are two built-in light sources: a quartz tungsten halogen lamp (NIR) and a Globar (MIR). Both light sources are connected to a water cooling system for protection against overheating while operating in vacuum conditions.

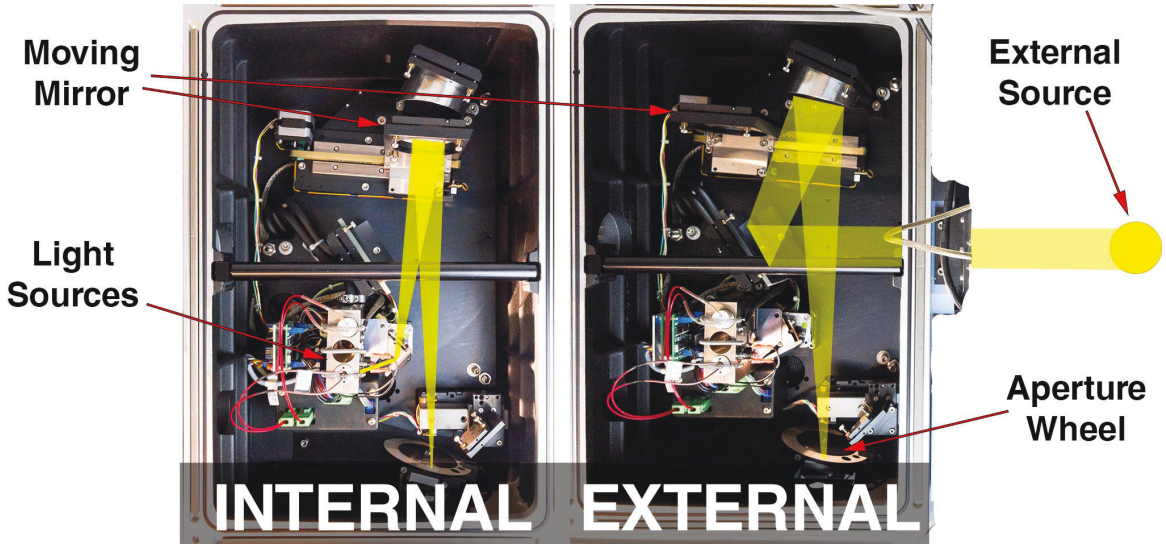

Figure II.6 – Photo of the source compartment operating in the two modes. The right picture illustrates the external light source mode. Left shows the internal light source mode. The light path for both modes is shown in yellow colour.

The built-in light sources are used for the gas cells measurements (see Section II.3). The NIR source is also used for the optical alignment procedures, such as a verification of the gas cell placement and to check the optical alignment of the spectrometer components, while the MIR source is invisible to the naked eye. From the source compartment the light passes through the aperture to the interferometer compartment.

b) Interferometer compartment

The light from the source compartment enters to the interferometer compartment through the circular aperture and is then collimated by a parabolic mirror (Fig. II.7). The interferometer compartment includes a permanently-aligned interferometer with two cubecorner retroreflectors and a beamsplitter. One cubecorner retroreflector is fixed and one is installed on a hybrid bearing that can travel over two bars reaching the maximum path difference of 258 cm. The optical path difference is exactly determined by a stabilized 632.9 nm HeNe laser.

The beamsplitter has a 30° angle of incidence, which reduces polarization effects and uses the beamsplitter more efficiently. The design of the interferometer allows to manually change the beamsplitter in order to optimize the signal in different spectral regions.

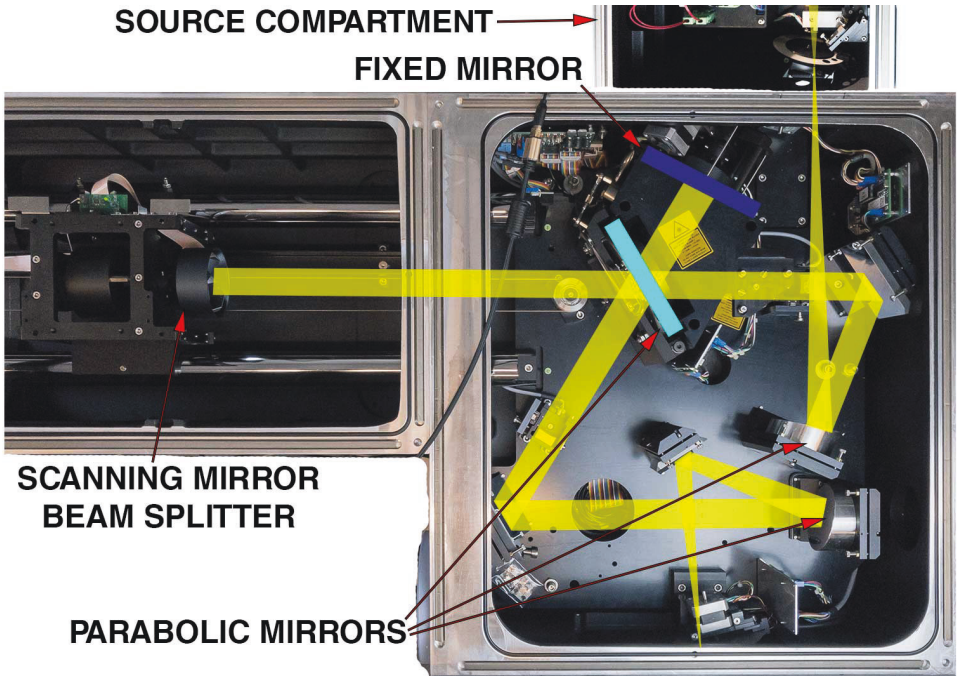

Figure II.7 – The interferometer compartment. Cubecorner retroflectors are denoted as fixed and scanning mirrors. The light path is shown in yellow.

The TCCON-Paris instrument uses two beamsplitters: one made of CaF_2 (used for TCCON measurements) and another made of KBr (used for NDACC short terms measurement campaigns). From the interferometer compartment the light passes through the sample compartment to the detector compartment.

c) Sample compartment

The sample compartment is used for holding different sample cells. Two different light paths can be selected in the compartment. One path is reserved for TCCON measurements and contains a permanently installed HCl gas cell used for ILS measurements (See section II.3). The second path is used for NDACC measurements (no cell incorporated into the beam) and, when installed occasionally, for other gas cell measurements (like HBr or N_2O).

d) Detector compartment

The detector compartment contains three detectors that cover different spectral regions: InGaAs, InSb and MCT (see Table II.1) and two filter wheels. The InGaAs detector is used for TCCON measurements with metallic mesh filter (in order to attenuate the signal intensity and to avoid detector saturation). InSb and MCT detectors are used for NDACC measurements with different optical filters.

Table II.1 – Detectors and their spectral regions.

Detector	Spectral Range, cm^{-1}	Operating temperature
InGaAs	4000-12800	Room temperature
InSb	1850-9600	Liquid-nitrogen cooled
MCT	600-12000	Liquid-nitrogen cooled

II.2.2 Solar Tracker

The solar tracker is the second major component of the FTS-Paris instrument. It is installed on the roof terrace at Jussieu campus of Sorbonne Université, 60 m above sea level (a.s.l.) (see Fig. II.8). The solar tracker consists of two plane mirrors that rotate along an azimuth and elevation axis driven by two stepper motors. One mirror is fixed on the base that can rotate around he vertical axis to follow the azimuth of the Sun and the second mirror can rotate around the horizontal axis to follow the elevation position of the Sun. The arrangement of mirrors guarantees that the solar light is always reflected downward into the spectrometer, independent of the solar position.

a) Optical feedback

The solar tracker can operate in two modes: in the first mode the orientation of the solar tracker mirrors is calculated from the time and geographical position of the solar tracker, the second mode is the tracking mode which is used for solar measurements. The tracking mode is controlled by an optical feedback system. There are two commonly used optical feedback systems: a quadrant photodiode and a Camtracker, both being described below.

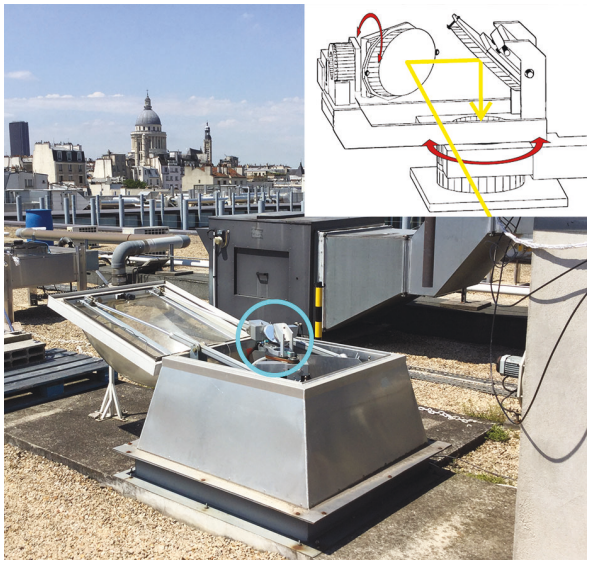

Figure II.8 – A photo of the Solar Tracker of the FTS-Paris instrument. Top right is a schematic setup of the tracker, the picture is taken from [22].

Quadrant photodiode. A small fraction (∼10%) of the incoming solar beam is focused onto a Si quadrant photodiode. Each of four parts of the photodiode measures the solar intensity and the signals are fed into the control loop which decides how to orient the solar tracker by equilibrating the signals of the four quadrants. FTS-Paris has used the quadrant photodiode system until January 2018. At this days it is replaced by a Camtracker.

Camtracker. The Camtracker is a camera based system that was developed in a collaboration of Karlsruhe Institute of Technology (KIT) and Bruker company [22]. The camera is installed inside the source compartment (Fig. II.9). It observes the image of a solar disc centered around the aperture. The recorded images are then evaluated by the Camtracker's software in real-time, which determines the position of the solar disk. The software separates the bright area illuminated by the Sun from the non illuminated dark area (Fig.II.9(a), red curve), and fits the bright area with a circle (green curve). Then it orients the solar tracker to match the center of the circle and the center of the aperture whole (shown as a green cross), Fig.II.9(b).

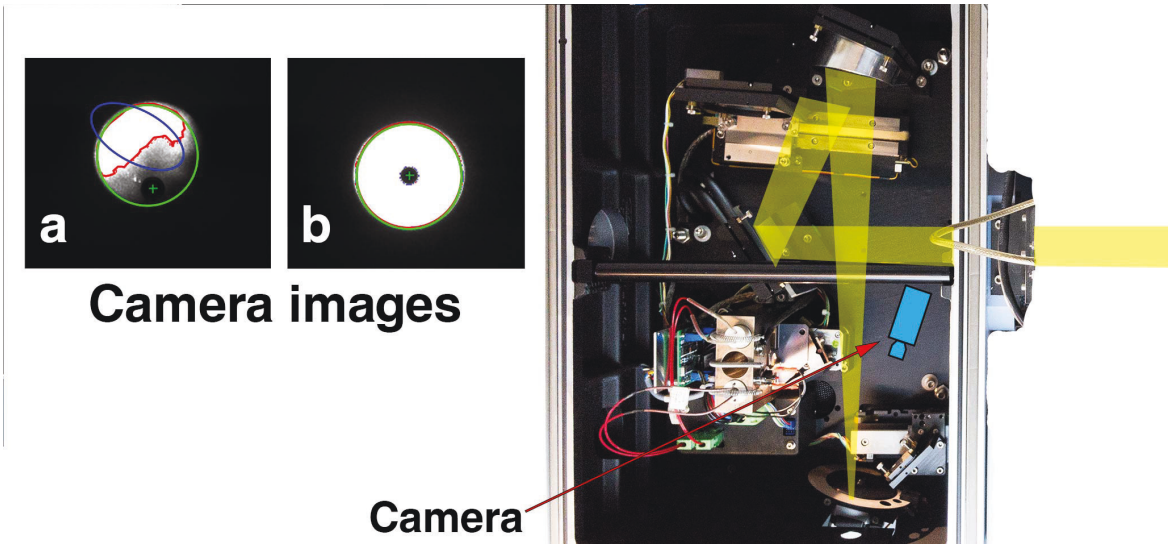

Figure II.9 – The Camtracker system. Right picture shows the source compartment with the installed camera inside. Two left pictures are images observed by the Camtracker: a) in tracking mode during a cloud passage b) in tracking mode with clear sky. The center of the solar disk matches the center of the aperture(green cross).

II.3 Instrumental Line Shape measurements

FTIR spectrometers are highly precise and stable devices, and if carefully aligned, the instrumental line shape (ILS) might not too differ from the ideal ILS (sinc function). However, their alignment can change due to mechanical degradation over time. The TCCON retrieval code GGG2014 (described in Section IV.3) assumes an ideal ILS in spectra retrieval, and the maximum ILS degradation is prescribed as 5% for the modulation efficiency (ME) amplitude.

The ILS is the Fourier transform of the weighting function applied to the interferogram. This weighting consists of two parts: an artificially applied part to change the calculated spectrum and an unavoidable part which is due to the fact that the interferogram is finite in length (box car function) and the divergence of the beam is non-zero (due to the non-zero size of the entrance aperture, see self apodization in Section II.1.3).

The instrumental line shape of the FTIR spectrometer can principally be determined by two different methods: 1) direct ILS measurements with the use of a strictly monochromatic laser, but the ILS is calculated only for the laser wavelength and could be different at other wavelengths; 2) through the use of thermal source in combination with the suitable gaseous absorber (well known molecular gas). In this work we are using the second method (gas cell measurements).

II.3.1 ILS retrievals from low pressure HCl gas cell measurements

The HCl lines are spectrally so narrow that the ILS characteristics become recognizable. Performing the analysis on several lines (either MWs or a single broad MW) improves the ILS reconstruction. The relative intensities of the HCl lines depend on the temperature, which therefore can also be retrieved.

A low pressure HCl gas cell ($\sim$ 5hPa) is included in most TCCON instruments in order to continuously monitor the ILS and the instrument stability. The spectra of HCl gas cell are recorded with the use of NIR source. An example of the HCl gas spectrum is shown in Fig.II.10

The HCl gas spectra are analyzed with the use of the LINEFIT software developed by F. Hase [23, 24]. LINEFIT calculates the deviation of the measured ILS from the ideal ILS. LINEFIT determines the ILS by performing a constrained fit of parameters which describe the interferometer's modulation efficiency (ME) in the interferogram domain. The ME is a complex function of the optical path difference (OPD), which is represented by a ME amplitude and a phase error (PE). The ME amplitude is connected to the width of the ILS, while the PE quantifies the degree of ILS asymmetry. For a perfectly aligned spectrometer, it would meet the ideal nominal ILS characteristics and thus have a ME amplitude of unity and a PE of zero along the whole interferogram. However, if the FTIR spectrometer was a subject to misalignment, the ME amplitude would deviate from unity and the PE would deviate from zero. At zero optical path difference (ZPD) the modulation efficiency is assumed to be one. If the ME amplitude growth with increasing OPD, it means that at ZPD Haidinger fringes (interference pattern of the Michelson interferometer from the extended source of monochromatic light) are less centered in compare with bigger OPD. If the ME amplitude decreases (goes below unity) with bigger OPD then Haidinger fringes are less centered (see Section II.4).

Fig.II.11 shows an example of ME amplitude and ILS before (05/02/2016) and after

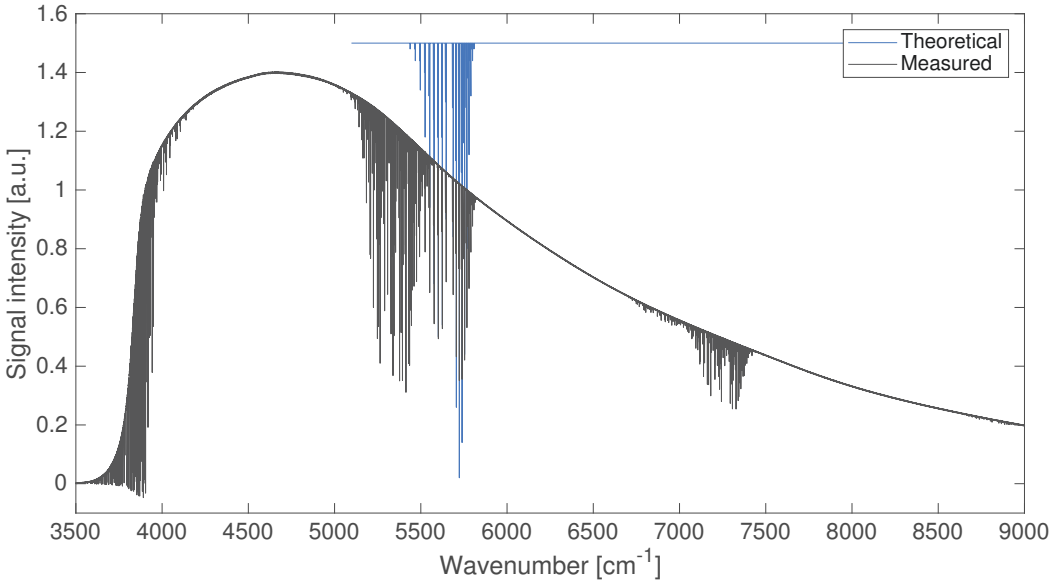

Figure II.10 – An example of HCl spectrum (black line) measured by the TCCON-Paris instrument and a theoretical spectrum (blue line).

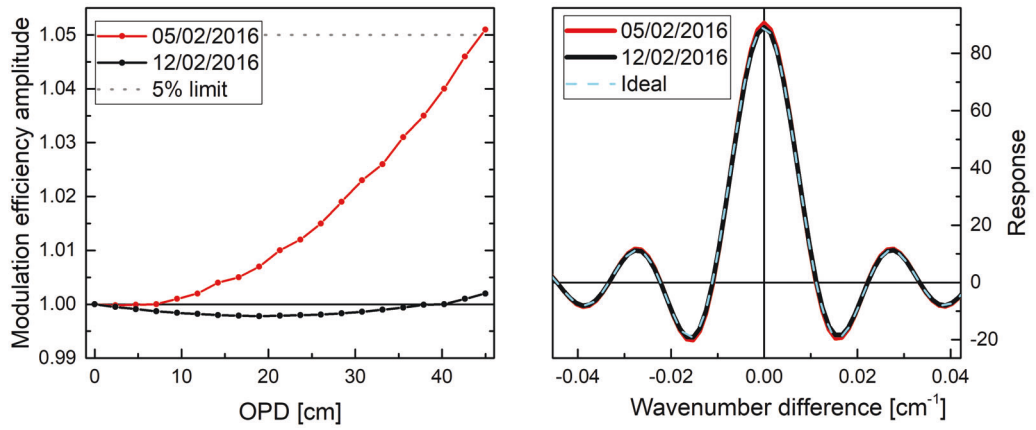

Figure II.11 – Modulation efficiency amplitude (left) and ILS (right) calculated by LINEFIT before and after optical alignment of the FTS-Paris instrument.

(12/02/2016) optical alignment of the FTS-Paris instrument. Before the optical alignment the ME amplitude has achieved the limit of 5% (red curve) then the optical alignment procedure was made and the ME amplitude become close to unity.

HCl cell measurements are performed once every month in order to monitor the instrument's stability and to keep the instrument well aligned by performing the alignment procedure when it is needed. The time series of ME amplitude is presented in Fig.II.12. After the alignment procedure in February 2016, the instrument stays well aligned and the ME amplitude stays within ±2%.

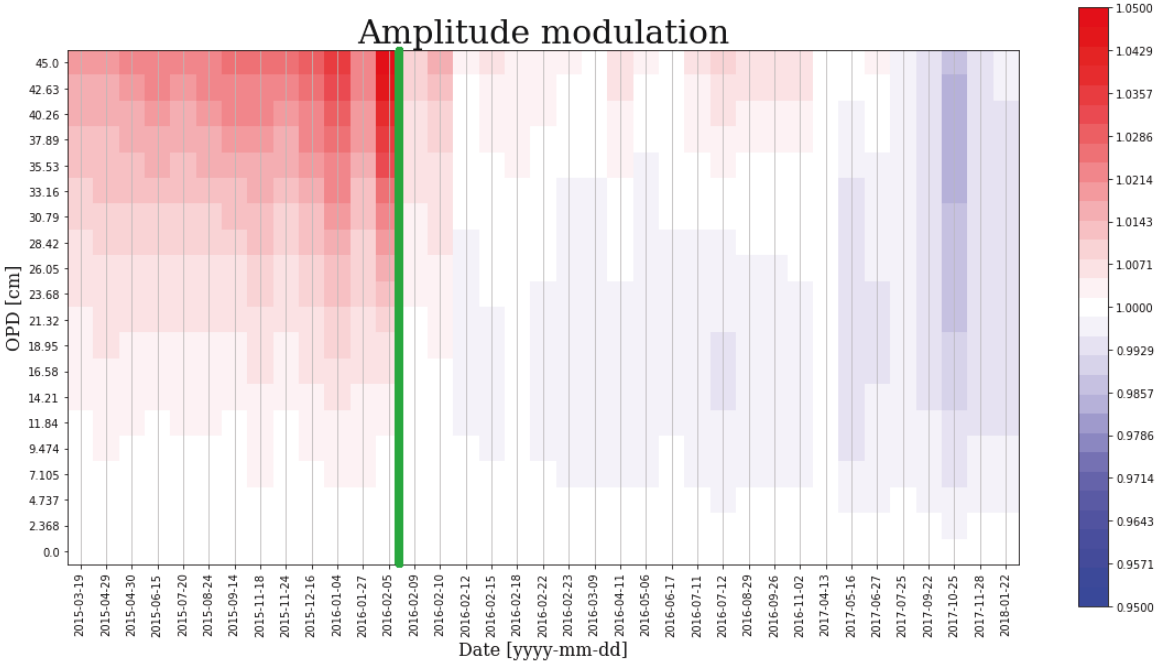

Figure II.12 – Time series of ME amplitude measurements for the FTS-Paris instrument. The green line indicates the optical realignment procedure.

II.4 Interferometer Alignment

In order to reduce the error caused by imperfect ILS, the ILS of every TCCON instrument should be kept as close as possible to the ideal ILS, and the TCCON specifications require that the ILS should be measured on a monthly basis with the use of low pressure HCl cell as described above. When the fluctuation of the modulation efficiency exceeds the 5% limit, the optical realignment procedure should be performed. In this section, we discuss the alignment procedure of the interferometer.

If the light from an extended monochromatic source is passed through the Michelson interferometer, circular interference fringes, known as Haidinger fringes, are produced in the plane of the source image. If the interferometer is perfectly aligned, the centre of the Haidinger fringes will match the centre of the source image (see fig.II.13 left). If the interferometer is misaligned than the centres do not match (see fig.II.13 right).

This means that for the perfectly aligned interferometer the centre of Haidinger fringes stays at the same position for different OPD. If the interferometer is misaligned and has defects (such as uneven bars along which moving cubecorner retroreflectors slides), then the centre of Haidinger fringes will be different for different OPD. The primary goal of the interferometer alignment is to get the Haidinger fringes as close as possible to the centre for different OPDs.

The commonly used setup for observing the Haidinger fringes is shown in Fig.II.14. An external HeNe laser placed into the source compartment is used as a monochromatic light source. The telescope is used to observe the Haidinger fringes. The position of the Haidinger fringes is changed by tilting the fixed cubecorner retroreflector. The final tilt of the fixed

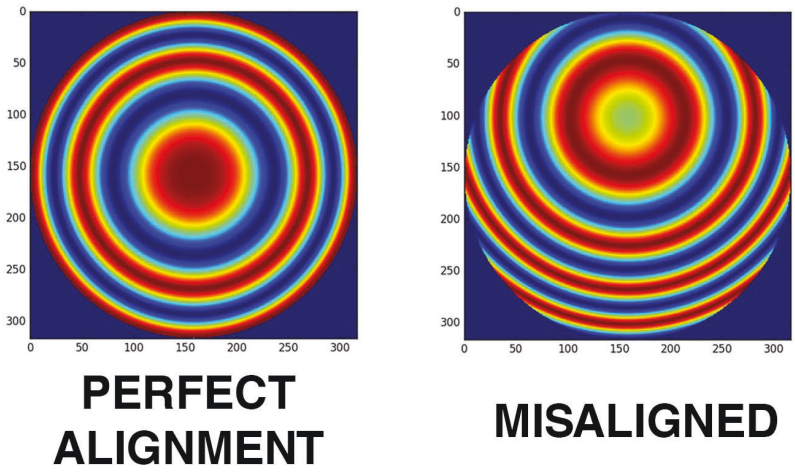

Figure II.13 – Simulation of the Haidinger fringes for the perfectly aligned and misaligned interferometers at MPD. Source: [25]

cubecorner is achieved when the position of the Haidinger fringes is close to the centre at all OPDs. The alignment of the interferometer is then verified by the HCl cell measurements and ME amplitude variability (it should stay close to unity), as it was shown in the previous section.

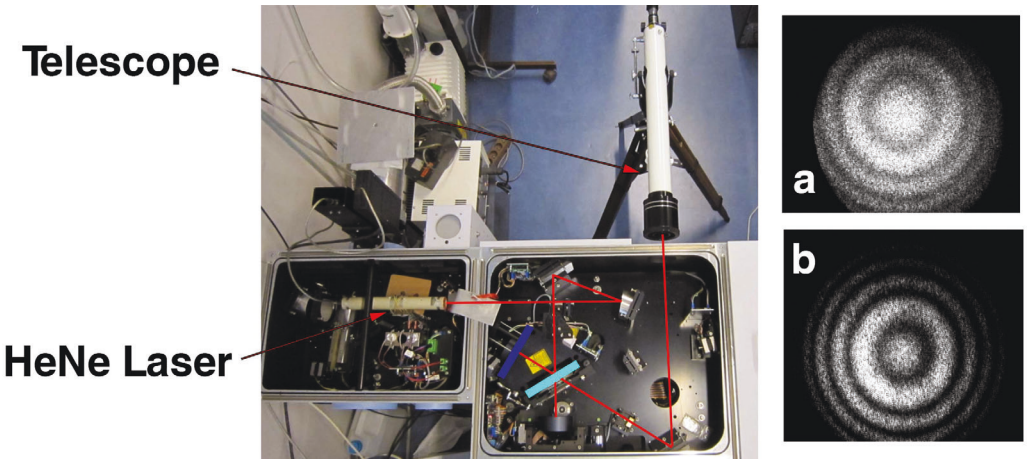

Figure II.14 – Left picture is a commonly used setup for observing Haidinger fringes. Right pictures: Haidinger fringes recorded at OPD = 80 cm before (a) and after (b) alignment.

II.4.1 New setup for the observation of Haidinger fringes

The standard setup uses a telescope for the observation of Haidinger fringes. In this section, we propose a new and more convenient setup, presented in Fig.II.15. Let's consider the path of the collimated beam (it is coloured in red) sorting from the interferometer (1). In the telescope setup, the beam after the reflection by a plane mirror (2) passes to the telescope's entrance window (7) and a parabolic mirror (3) should be removed. The parabolic mirror

has the focal length of 80 mm and used to focus the beam on the aperture (behind (5)). In the proposed setup the parabolic mirror (3) is not removed, instead, it is used to form the image of the Haidinger fringes. The focused beam after the reflection by a plane mirror (4) is reflected by an introduced plane mirror (5) on the CCD matrix of the camera (6). The camera is mounted on the adjustable holder which allows finding a focal point.

On the presented setup the beam is reflected upward because the camera is installed above, but the camera could be also installed on the right side of the mirror (5). Installing the camera inside of the interferometer compartment would allow to use it remotely and under vacuum conditions.

Advantages of the proposed setup are: 1) There is no need in the telescope. 2) There is no need to remove the parabolic mirror (3). 3) It could be operated in the vacuum conditions and remotely controlled, which could be useful for remote sites. 4) It is very fast to install (∼5 minutes) and does not require any additional space.

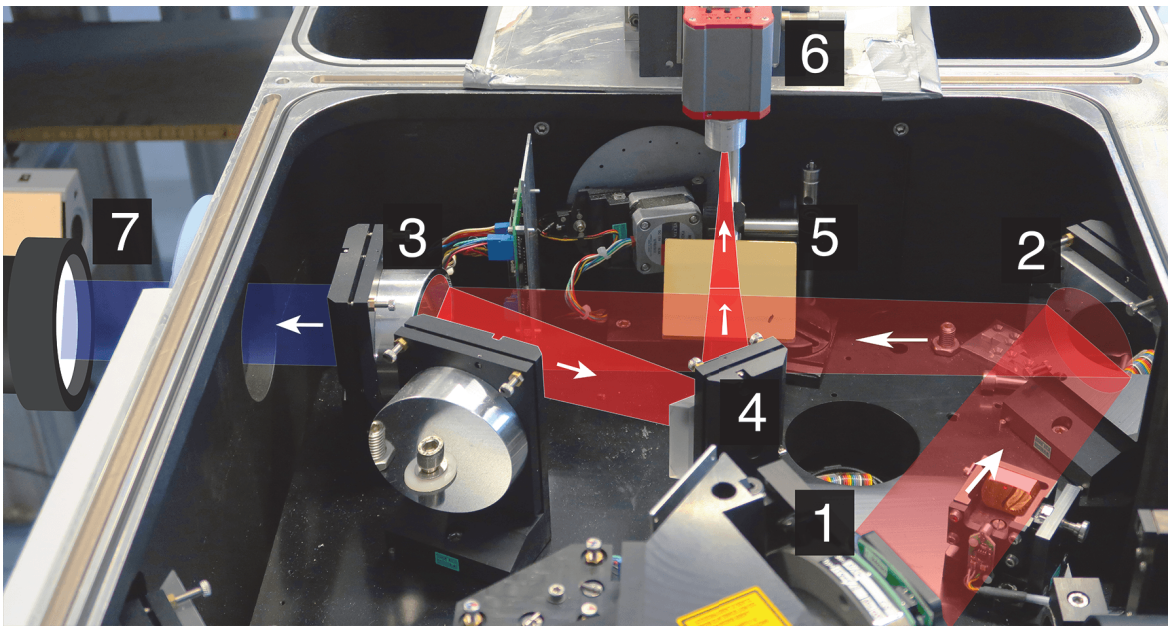

Figure II.15 – The new setup for the observation of Haidinger fringes: 1) Beamsplitter, 2) Flat mirror 3) Parabolic mirror 4) Flat mirror 5) Added flat mirror 6) CCD matrix 7) telescope.

III – N_2O cell intercomparison exercise

The FTS-Paris instrument is not only used for TCCON measurements, but also for measurements in the frame of the NDACC-IRWG network. The Infrared Working Group represents a network of infrared Fourier-transform spectrometers that is part of the Network for the Detection of Atmospheric Composition Change (NDACC, [26]). NDACC-IRWG measurements are performed in the MIR at the spectral resolution of 0.005 cm^{-1}. They cover the absorption bands of O_3, HNO_3, HCl, HF, CO, N_2O, CH_4, HCN, C_2H_6 and $ClONO_2$. While TCCON uses HCl gas cell for the monitoring of the ILS, the NDACC-IRWG network relies on low pressure HBr gas cell measurements for monitoring of the ILS and the stability of the instrument. The instrument stability is determined by continuous analysis of the HBr column in a sealed cell. However, the stability test is compromised by slow decomposition of the reactive HBr in the cell, likely due to a chemical reaction with residual contaminations on the walls of the cell [24].

This chapter describes an intercomparison exercise of a set of new low pressure N_2O gas cells, which are intended to replace currently used HBr cells. The major aim of this first N_2O cell exercise is whether the different NDACC sites obtain reproducible N_2O columns.

III.1 Description of the gas cell exercise

The exercise was organised and led by Frank Hase (Karlsruhe Institute of Technology (KIT), Karlsruhe, Germany). Like the HBr cells, the N_2O cells were produced by a private company (NDS) under the supervision of the NDACC-IRWG lead at UCAR (University Corporation for Atmospheric Research). The sapphire cell bodies all have a length of 20 mm and a diameter of 20 mm. They are equipped with wedged windows made from sapphire. After inspection, all 35 gas cells were filled with pure N_2O gas at the same low pressure by the UCAR group and sent to KIT, where reference measurements of all cells have been made using the NDACC instrument at KIT. The gas cells were then distributed to the different sites, where each team should determine the N_2O column in a blind study. The results had to be communicated to KIT. The Paris cell was labelled number 26 (# 26) and received in April 2016.

III.1.1 N_2O gas column blind test measurements

The N_2O cell was supplied with a set of recommended measurement parameters, to guarantee consistent measurement setups: spectra had to be recorded with a maximum optical path difference (MPD) of 180 cm (resolution of 0.005 cm^{-1}) and with the use of a GLOBAR source. An example of a measured spectrum (in black) and a simulated N_2O transmission spectrum (in green) is shown in Fig.III.1.

In order to measure the transmission spectrum, the measured absorption spectrum needs to be normalised by a background spectrum. Ideally, the background spectrum is obtained

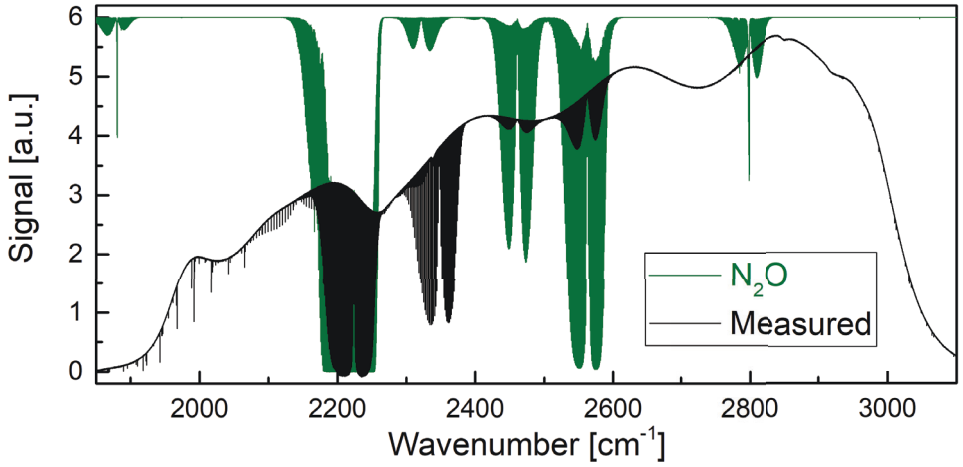

Figure III.1 – An example of measured N_2O gas spectrum (the black curve). The green curve is a theoretical transmission spectrum of N_2O, scaled to 6.

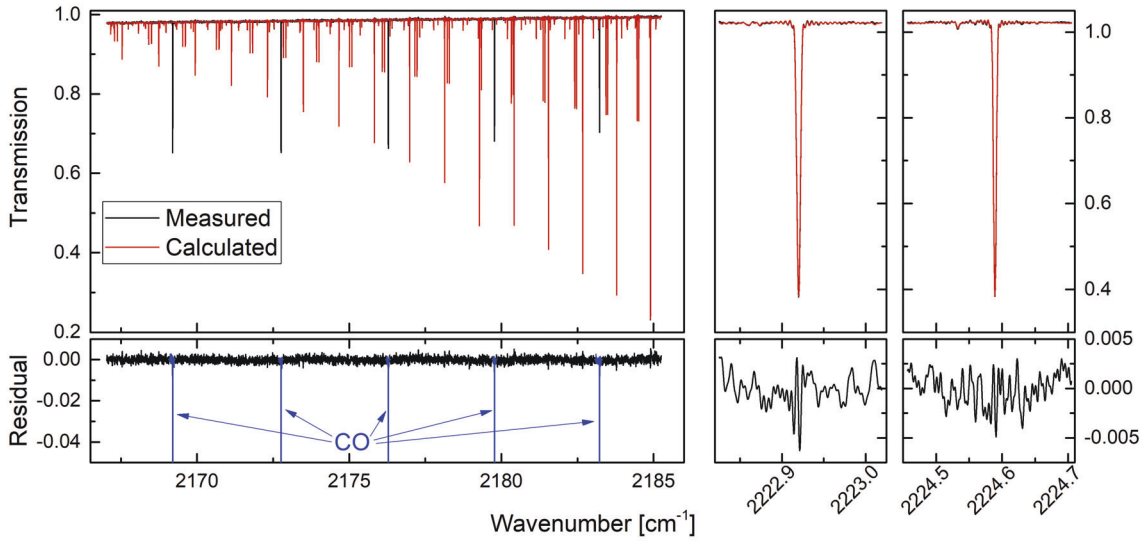

Figure III.2 – Three microwindows used for the analysis of N_2O transmission spectra. Top panels are calculated (red) and measured (black) transmission spectra. Bottom panels are residuals (measured - calculated).

with an empty cell. As this cannot be realised with our sealed cell, the background measurement is approximated by performing a measurement without the cell. The background spectrum was recorded at the resolution of 0.01 cm^{-1}. The transmission spectrum is obtained by measuring 8 spectra (each contains 20 scans: 10 forward and 10 backward) which are then averaged and divided by the background spectrum.

It was agreed to use the LINEFIT software [23, 24] for the analysis of N_2O transmission spectra. We have selected all three proposed microwindows: two very narrow microwindows which contain one isolated N_2O line each. They are centred at 2222.9 cm^{-1} and 2224.6 cm^{-1}, respectively. The third microwindow is about 20 cm^{-1} wide and has its centre around 2175 cm^{-1} (Fig.III.2).

All measurements are performed in the evacuated spectrometer. A first evaluation of the N_2O spectra has shown that apart from N_2O molecules, CO molecules are present (Fig.III.2, blue lines in residual). This is caused by air leaking into the spectrometer because the vacuum pump has been stopped during the measurements to avoid mechanical vibrations. The CO background problem has been judged so severe that it was decided to register the spectra without stopping the vacuum pump. The N_2O column for the blind intercomparison could thus be obtained without CO.

III.1.2 Results of the intercomparison test

The evaluation of the Paris cell with the LINEFIT software yielded a N_2O column value of 4.549×10^{20} molecules per m^2. The results of the first round of intercomparison was communicated to KIT and compared to the reference values determined there. Fig.III.3

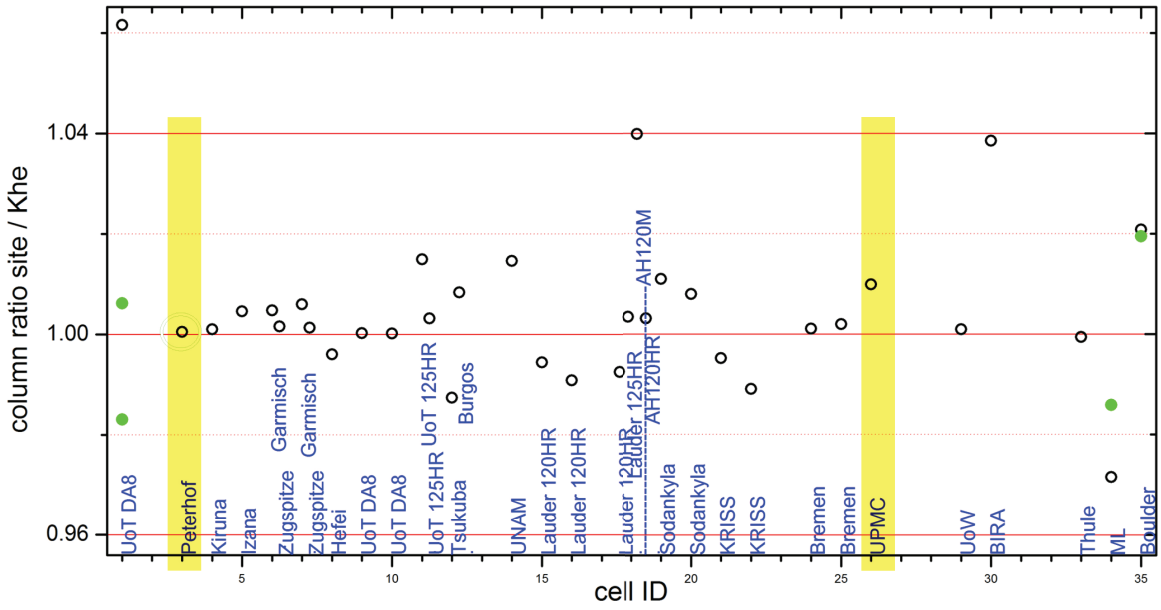

Figure III.3 – The N_2O column ratios calculated by different sites for the intercomparison exercise. The figure reports the ratios of N_2O columns calculated by sites to the reference N_2O columns calculated by KIT. Two yellow rectangles highlight the Paris (denoted UPMC) and Peterhof N_2O cells. Source: [27].

gives the relative deviation of the first round results with respect to the reference values.

The observed deviations of all sites are between -3% and +5%. The Paris instrument has a 1% deviation whereas some selected sites (Peterhof, Kiruna, Izana and others) agree perfectly with the results from KIT. While the 1% deviation is within the nominal ±4% NDACC-IRWG limit, it was expected that the measurements were more accurate than that and further tests have been made.

III.1.3 Origin of the bias between N_2O columns measured by FTS-Paris and KIT instruments.

Several experiments have been made to find the origin of the Paris - KIT bias. Some of them, linked to interference with background CO absorption, which gave consistent results on the Paris measurement are described in Sections III.2 and III.3. The reference measurements of the N_2O cell #26 were therefore revisited by F. Hase at KIT. At this occasion a problem with the KIT spectra of cell #26 has been identified: the retrievals of the modulation efficiency amplitude contained an unphysical jump near ZPD (OPD=0 cm), which remained unnoticed during the first reference analysis (Fig.III.4, the red curve). This jump is observed between ZPD and the first fitted value (OPD = 9.5 cm). The a posteriori prescription of a smooth ILS leads to a smooth modulation efficiency (blue curve in Fig.III.4). The reference column of N_2O with the smoothed ILS is 4.537×10^{20} m^{-2} instead of 4.503×10^{20} m^{-2} obtained with the artefact. This reduces the relative bias between Paris and KIT measurements from 1.0% to 0.26%, bringing the deviation well in the expected range.

Currently, all other reference spectra are being checked for the presence of the same artefact.

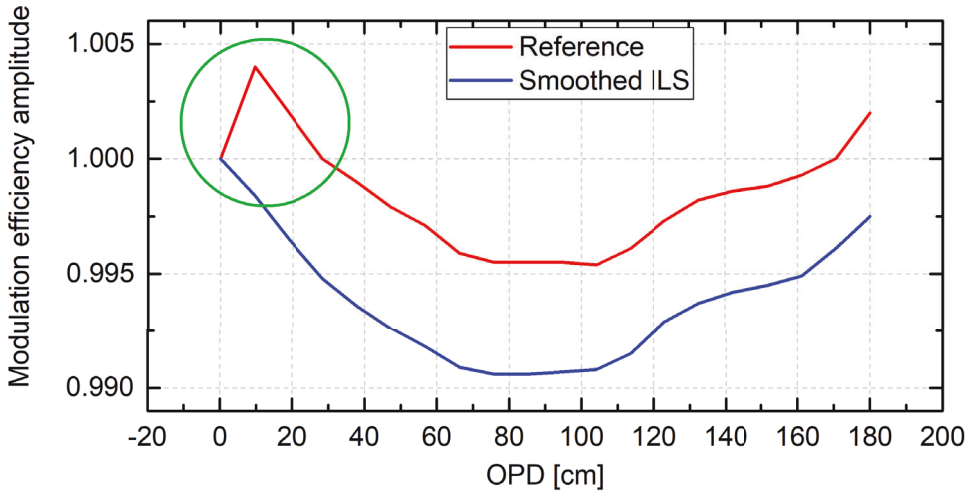

Figure III.4 – The modulation efficiency amplitude for the reference measurements of N_2O cell #26. The red curve is ME amplitude affected by the artefact, the green circle indicates the artefact, the blue curve is ME amplitude obtained with prescribed smooth ILS.

III.2 Comparison of Peterhof and Paris FTS instruments.

During the annual joint IRWG and TCCON meeting 2017 in Paris, M. Makarova (St. Petersburg State University, St. Petersburg, Russia) has brought the N_2O cell #3 for the intercomparison between Paris and Peterhof instruments. The N_2O column of cell #3 measured by the Peterhof instrument is biased by 0.06% from reference N_2O column measured by KIT. Fig. III.5 shows the transmission spectrum of N_2O cell #3 measured by Peterhof instrument. As in the case of Paris instrument, CO lines are presented in the residual.

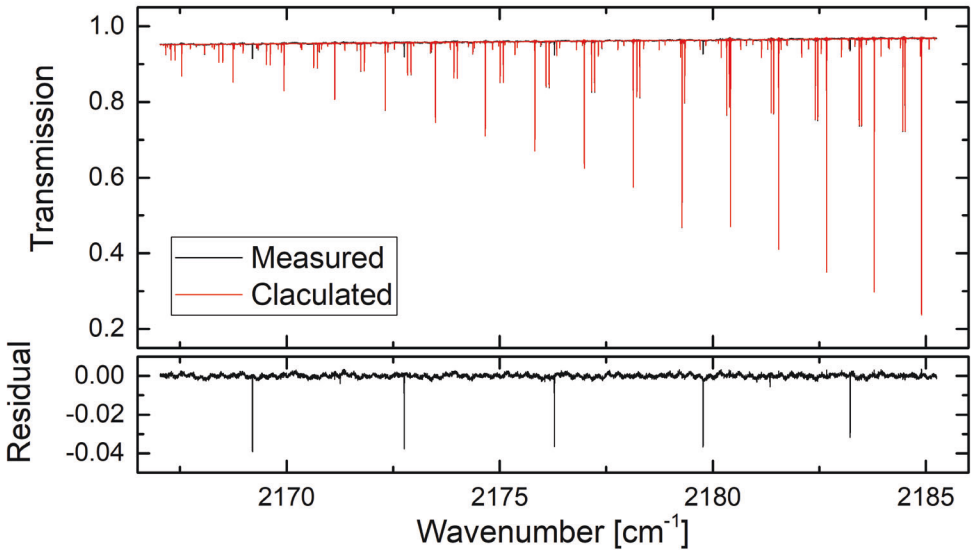

Figure III.5 – The transmission spectrum of the N_2O cell #3 measured by the Peterhof instrument.

The reported N_2O column for the cell #3 measured by Peterhof instrument is 4.4635×10^{20} m^{-2} which is 0.06% above the reference values measured by KIT which is 4.4610×10^{20} m^{-2}. The N_2O cell #3 was measured by the FTS-Paris instrument by the use of the same acquisition setup that was used for the Peterhof instrument. Both acquisition setups differ only in the number of scans, 300 scans were used instead of 180. The column of the N_2O cell #3 measured by the FTS-Paris instrument is 4.4815×10^{20} m^{-2}. This value is 0.46% above the reference value, which gives a Peterhof - Paris bias of the same magnitude.

From private communication with Maria Makarova it turned out that the CO lines in the residual of the Peterhof measurements went unnoticed and were not deweighted in the analysis. By comparing the analysis of the Peterhof and Paris spectra of the cell #3 it was find out that the channeling effect (oscillations of the signal level caused by interferences inside of the optical element, such as filters or beamsplitter) was not accounted for in the analysis of the Peterhof transmission spectra (see the small oscillations in the residual of Fig.III.5).

We therefore compared retrievals for cases when the CO lines were deweighted and when they were not. The effect of deweighting CO lines alone leads to an increase in the N_2O

column by +0.41%. When the channeling effect is accounted for, the N_2O column decreases by 0.05%. The combined effect of channeling and CO deweighting leads to a +0.52% on the N_2O column. If these effects are taken into account the Peterhof results requires a correction by +0.52%, reducing the previously mentioned Peterhof-Paris bias to below 0.1%. This means that the two instruments don't have a systematic bias. However, the Peterhof result is now about 0.5% higher that the KIT reference value.

III.3 Stability tests of the Paris instrument

In September 2017, we made a stability test of the FTS-Paris instruments using the N_2O cell. The goal is to quantify the stability of the instrument and to determine the optimal number of scans for N_2O cell measurements or other comparable exercises.

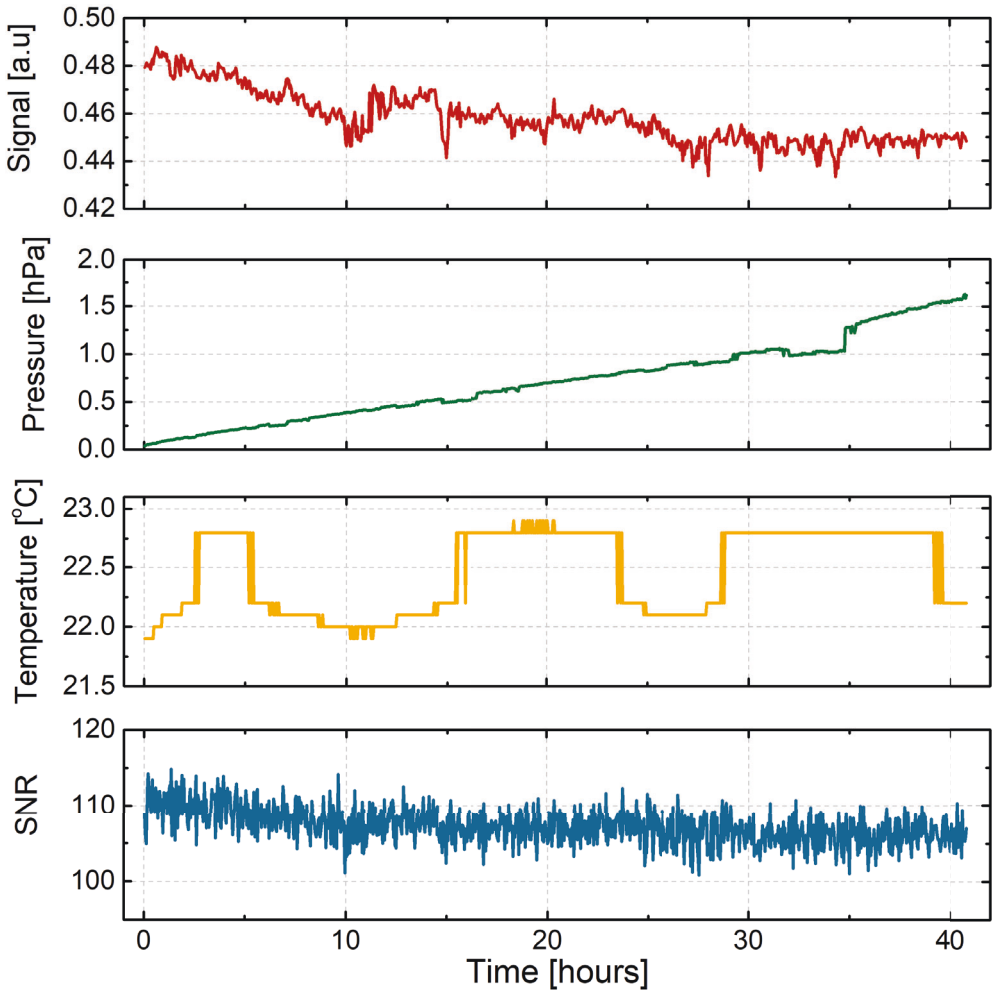

Figure III.6 – From top to bottom: 1) The signal (in arbitrary units, a.u.) measured around 2220 cm^{-1}; 2) the pressure and 3) the temperature inside the instrument; 4) the signal to noise ratio around 2220 cm^{-1} for each spectrum. All data are given as a function of measurement time.

We thus measured 1000 spectra of N_2O cell, each spectrum contains 2 scans: 1 forward and 1 backward. The instrument has been pumped down to the pressure of 0.04 hPa (which has been measured by the built in pressure sensor). During the measurements, the vacuum pump has been stopped and pressure has raised up to 1.61 hPa at the end of the acquisition. The temperature stayed between 21.8 and 22.9 °C. The signal and the signal to noise ratio (SNR) of each spectrum are measured around 2220 cm^{-1}. During the first 10 hours the signal shows an initial decrease from 0.48 to 0.45 a.u. and then stays in the range between 0.43 and 0.47 a.u. The SNR decreases correspondingly from 110 to 105.

All spectra are analysed using LINEFIT by two different methods. In the first method each spectrum is analysed separately. In the second method spectra are first progressively averaged, i.e 1st = 1st spectrum; 2nd = mean of 1st and 2nd; 3rd = mean of 1st, 2nd and 3rd; ... 1000th = mean of all spectra, and the averages are then analysed.

Stability of the N_2O column values

The N_2O columns (average for three microwindows) measured by the two methods are presented in Fig.III.7. The black points are individual spectra and the red curve is the moving average over black points (bin width of averaging is 100 points). The blue curve is the progressively averaged spectra.

The signal from a perfectly stable instrument could be averaged infinitely (reducing the noise), but real systems are stable only for a limited period of time (because of the drifts). We use the Allan variance as a measure of the instrument stability. The detailed description of Allan variance could be found in [28]. Briefly, the Allan variance is calculated by

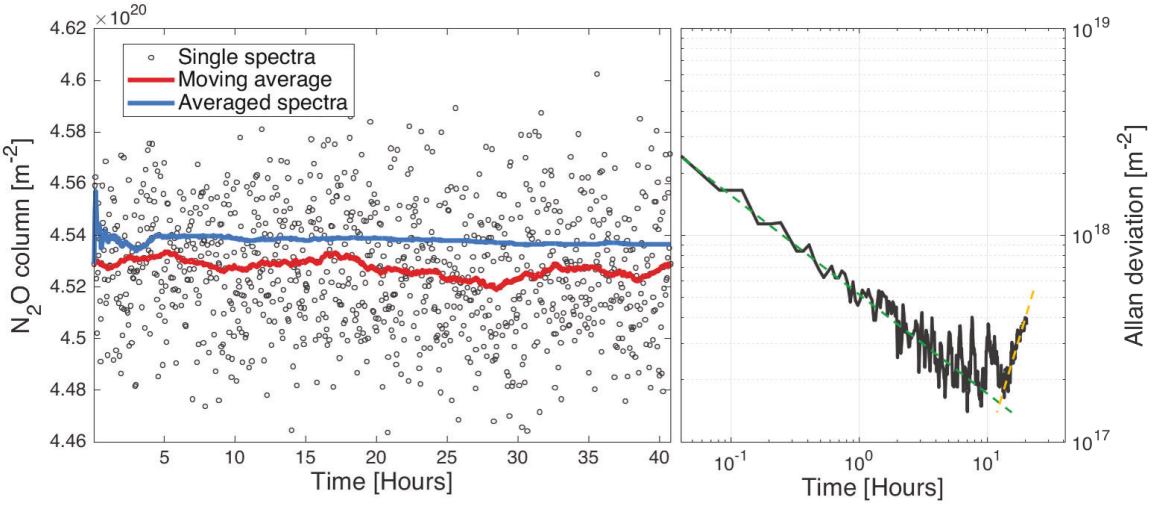

Figure III.7 – The left panel is the measured column of N_2O. Black points are the results for individual spectra, the red curve is the moving average of the N_2O columns. The blue curve shows the N_2O column of the progressively averaged spectra. The right panel shows the Allan plot of the individual spectra (black points). The green and yellow dashed lines are the supposed contributions from white noise and linear drift, respectively.

$$\sigma_y^2(\tau) = \left\langle \frac{(\bar{y}_{n+1} - \bar{y}_n)^2}{2} \right\rangle$$

where $\bar{y}_n$ is nth measurement obtained as an average over time τ, and $\langle ... \rangle$ is the expectation operator. The right panel of Fig.III.7 shows the Allan deviation (σ_y) plot of black points, where the Allan deviation has been calculated as the square root of the Allan variance (σ_y^2). The decreasing green dashed line shows the theoretically expected behaviour of a drift free instrument, i.e contribution of white noise is dominating over the drift. The increasing yellow dashed line shows the domain where the linear drift sets in. The minimum of the Allan plot gives the optimal integration time. The optimal time for the N_2O column averaging is ~ 9 hours, which corresponds to 440 scans. This means that for the N_2O cell intercomparison test the integration time (3.2 hours) could still be prolonged. A more accurate result would have been obtained after integration over 9 hours.

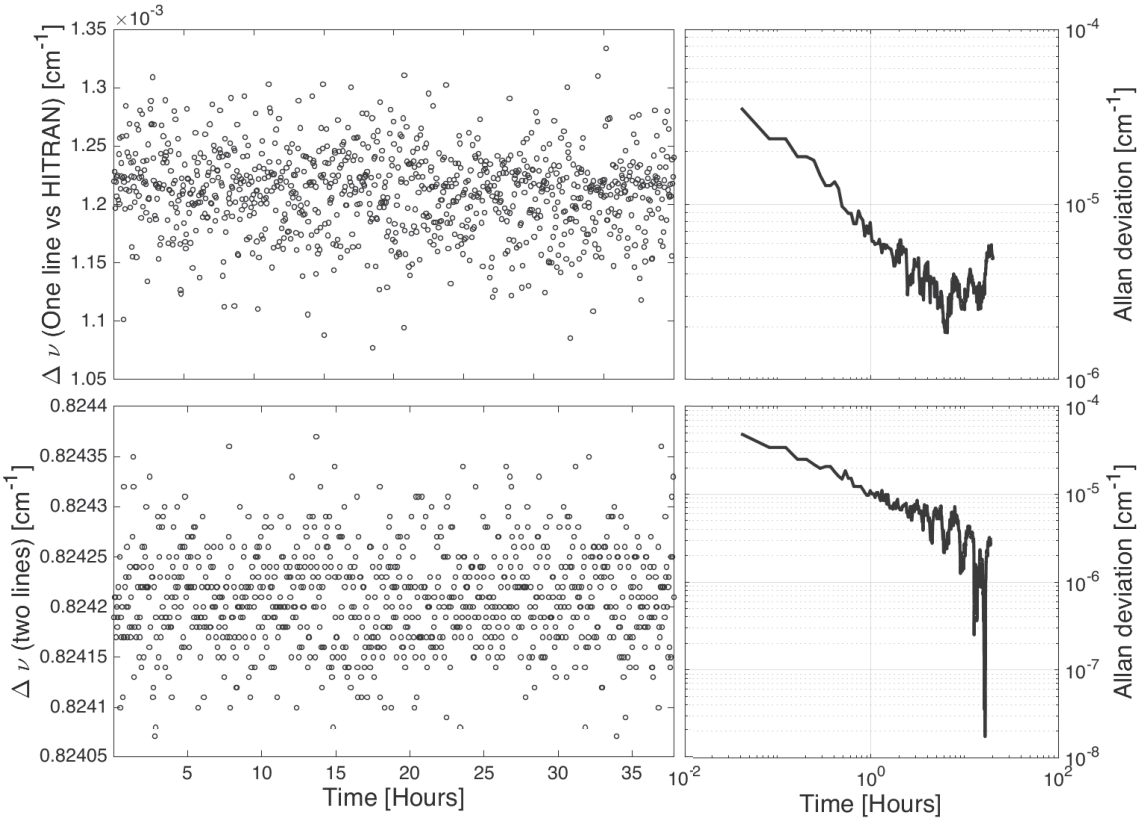

Figure III.8 – Top panels: the left panel shows the position of the 2222.918 cm^{-1} line relative to the HITRAN 2016 line position (2222.91875 cm^{-1}). The right is the corresponding Allan deviation. Bottom panels: on the left the difference in line position between two lines (2222.078 and 2222.918 cm^{-1}) is shown. The right panel shows the Allan deviation.

Stability of the N_2O line position

From the previous exercise we expect the instrument stability of 9 hours at least. In order to verify the stability of the absorption lines positions, we took the two N_2O absorption lines centred at 2222.078 and 2222.918 cm^{-1} and calculated the centre of each line using a center-of-gravity method, described in [21].

The top left panel of Fig.III.8 shows the position of the 2222.918 cm^{-1} line relative to the HITRAN 2016 position, and the bottom left panel shows the difference in positions between the two N_2O lines (2222.078 and 2222.918 cm^{-1}). The time series (on the left side of Fig.III.8) do not show any apparent drift in both measurement values. From the Allan deviation plot on the top right panel, however, one can see that the position is stable for the period of 6.1 hours before a drift sets in. On the contrary, the line position difference remains stable over the entire measurement period, as shown by the Allan deviation in the bottom right panel. During the evaluation with the LINEFIT software spectra are fitted with the variable wavenumber offset. Column measurements therefore correspond to the situation in the lower panels, which explains why the column density measurements were stable for more than 6 hours.

Conclusion

For integration times smaller than 6 hours the instrumental drifts play no role. If one sums up spectra obtained over a period longer than 6 hours (equivalent to 300 scans) one would obtain sum spectra with artificially broaden lines (see Fig. III.9). However, if spectra are averaged and evaluated on a shorter time scale one could repeat measurements up to 9 hours, for example two spectra measured over 4.5 hours each.

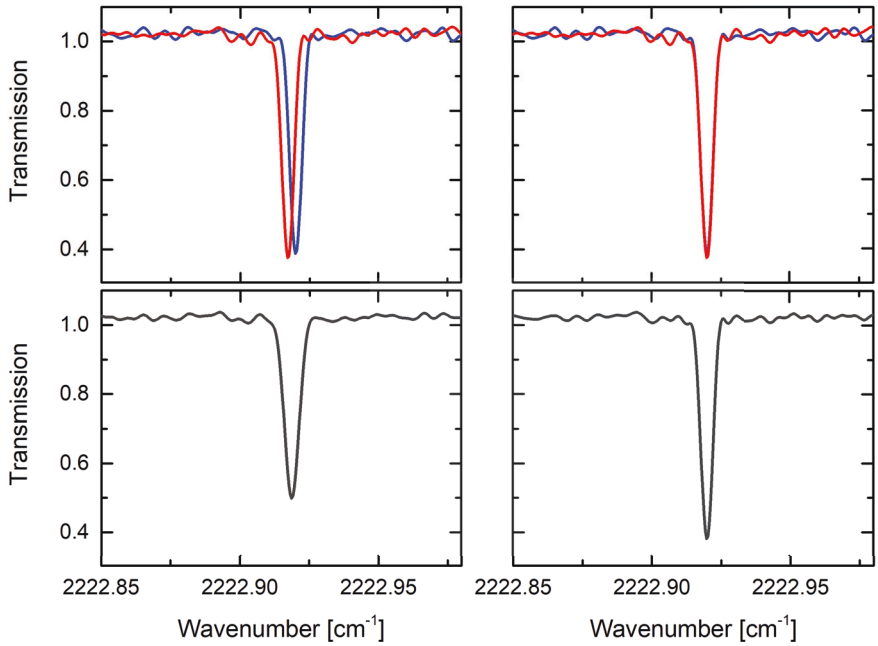

Figure III.9 – Two example of two absorption lines averaging. The top left panel shows two absorption lines (blue and red) that are affected by a position drift. The bottom left panel shows the result of averaging of two lines (black). The top right panel shows two absorption lines that are not affected by the position drift and the bottom right shows the result of two lines averaging.

IV – Retrieval codes

In this chapter, we describe the official TCCON software package GGG used for the analysis of the solar absorption spectra. Section IV.1 describes the principles of the radiative transfer. Section IV.2 describes the inverse method used to solve the radiative transfer numerically. Section IV.3 describes the GGG software package.

IV.1 Principles of Radiative transfer

A beam of radiation travelling through a layer of the atmosphere loses energy by absorption, gains energy by emission and redistributes energy by scattering. Here scattering processes will be ignored. Let the radiance of the beam at wavenumber $\tilde{\nu}$ at point s be $L_{\tilde{\nu}}$. Consider a thin layer of atmosphere of thickness ds. A differential equation describing radiative transfer in the absence of scattering is given by

$$\frac{dL_{\tilde{\nu}}}{ds} = p \cdot k_{\tilde{\nu}} \cdot (J_{\tilde{\nu}} - L_{\tilde{\nu}})$$

where $k_{\tilde{\nu}}$ is an absorption cross section of the air, ρ is the air density, $J_{\tilde{\nu}}$ is the emission function at wavenumber $\tilde{\nu}$.

The solution of radiative transfer equation for the beam travelling from point s_0 to point s through the atmosphere is given by

$$L_{\tilde{\nu}}(s) = \boxed{L_{\tilde{\nu}}(s_0) \cdot T_{\tilde{\nu}}(s_0, s)} + \boxed{\int_{s_0}^{s} J_{\tilde{\nu}}(s') \cdot T_{\tilde{\nu}}(s', s) \cdot \alpha_{\tilde{\nu}}(s') \cdot ds'} \tag{IV.1}$$

where

$L_{\tilde{\nu}}(s)$ is the beam spectral radiance at point s.

$L_{\tilde{\nu}}(s_0)$ is the beam spectral radiance at point s_0.

$T_{\tilde{\nu}}(s_0, s)$ is the atmospheric transmission between s_0 and s.

$J_{\tilde{\nu}}(s')$ is the source function at point s'.

$\alpha_{\tilde{\nu}}(s')$ is the absorption coefficient of the medium at point s' at wavenumber $\tilde{\nu}$.

In the condition of local thermodynamic equilibrium the source function $J_{\tilde{\nu}}(s)$ equals to the Planck function which is a black body spectral radiance at temperature T. The first term of

eq(IV.1) (left box) represents the radiance transmitted by the atmosphere and the second term (right box) represents the atmospheric emission. For the ground based solar absorption measurements the atmospheric emissions are negligibly small compared to the solar emission. The atmospheric transmission can be expressed as

$$T_{\tilde{\nu}}(s_0, s) = \exp(-\tau_{\tilde{\nu}}(s_0, s))$$

where $\tau_{\tilde{\nu}}(s_0, s)$ is the optical depth of the air between s_0 and s. The optical depth can be defined as the integral over absorption coefficient ($\alpha_{\tilde{\nu}}(s')$)

$$\tau_{\tilde{\nu}}(s_0, s) = \int_{s_0}^{s} \alpha_{\tilde{\nu}}(s')ds'$$

The $\alpha_{\tilde{\nu}}(s)$ could be represented as a sum of individual absorption coefficient of each atmospheric species.

Spectral line shape

The energy that molecule absorbs or emits is not continuous, since the molecule's energy states are discrete, and it is not infinitesimally narrow since different velocity components and interactions between molecules lead to line broadening. Natural line broadening (caused by the not infinite lifetime of excited states) has a Lorentz line shape, which is negligible for atmospheric conditions where the primary sources of line broadening are Doppler and pressure broadenings. Doppler broadening is caused by thermal motion of molecules which leads to the Doppler effect. Doppler broadening has a Gaussian line shape ($f_D(\tilde{\nu})$). Pressure broadening is caused by the collision of molecules, which leads to the shorter lifetime of excited states and as the Natural line broadening has the Lorentz line shape ($f_L(\tilde{\nu})$). Both Doppler and pressure broadening have to be taken into account for the analysis of atmospheric spectral lines. For this purpose, the Voigt profile ($f_V(\tilde{\nu})$) is used, which includes both broadening mechanisms. It is defined as a convolution of Gaussian and Lorentzian line shapes:

$$f_V(\tilde{\nu}) = \int_{-\infty}^{\infty} f_D(\tilde{\nu}')f_L(\tilde{\nu} - \tilde{\nu}')d\tilde{\nu}'$$

The analysis of transmission spectra is based on the inverse method, described below.

IV.2 Inverse method

The inverse method described in this section is based on the inversion theory of C. D. Rodgers [29]. Let the measured spectrum be represented by a vector $\mathbf{y}$ and the quantities to be retrieved by a vector $\mathbf{x}$ (for example the volume mixing ratio of the gases). The relationship between $\mathbf{y}$ and $\mathbf{x}$ is described by a forward model $\mathbf{F(x)}$:

$$\mathbf{y} = \mathbf{F(x)} \tag{IV.2}$$

The inverse method starts with the use of the first guess value $\mathbf{x}_0$ which is close to $\mathbf{x}$:

$$\mathbf{y}_0 = \mathbf{F}(\mathbf{x}_0)$$

then by subtracting $\mathbf{F}(\mathbf{x}_0)$ from Eq.(IV.2), and linearizing the forward model $\mathbf{F}(\mathbf{x})$ about $\mathbf{x}_0$ we get:

$$\mathbf{y} - \mathbf{F}(\mathbf{x}_0) = \mathbf{F}(\mathbf{x}) - \mathbf{F}(\mathbf{x}_0) = \frac{\partial \mathbf{F}(\mathbf{x})}{\partial \mathbf{x}}(\mathbf{x} - \mathbf{x}_0) = \mathbf{K}(\mathbf{x} - \mathbf{x}_0)$$

where $\mathbf{K}$ is a Jacobian matrix (it is also called the weighting function or kernel). Then Eq.(IV.2) can be rewritten as

$$\mathbf{y} = \mathbf{K}\mathbf{x}$$

The solution $\mathbf{x}$ can be found by minimising the sum of squares of the difference between the measurements $\mathbf{y}$ and calculations from the forward model $\mathbf{F}(\mathbf{x})$. This is done by linearisation about some estimate of the solution $\mathbf{x}_i$ and using the resulting equations to improve the solution, by using iteration method, where $\mathbf{x}_{i+1}$ is defined by

$$\mathbf{x}_{i+1} = \mathbf{x}_i + (\mathbf{K}_i^\intercal \mathbf{K}_i)^{-1} \mathbf{K}_i^\intercal [\mathbf{y} - \mathbf{F}(\mathbf{x}_i)]$$

where $\mathbf{K}_i$ is $\mathbf{K}$ calculated for ith iteration. For the first iteration step $\mathbf{x}_i$ is equal to the first guess value $\mathbf{x}_0$. The inverse method described above is implemented in the retrieval program call GFIT, used by TCCON for the analysis of solar transmission spectra.

IV.3 GGG - TCCON retrieval package

The GGG package of software tools [30] has been developed at Jet Propulsion Laboratory (California Institute of Technology, Pasadena, CA, USA) to determine the abundances of atmospheric trace gases from infrared solar absorption spectra. Each TCCON site uses the same version of GGG and the processing procedure is consistent from site to site.

The GGG package includes different programs: the most important of them are discussed in Sections IV.3.1-IV.3.3.

IV.3.1 Interferogram to spectrum (I2S)

The measured interferograms are converted to the spectra by the GGG program **I2S**. The interferogram processing includes a solar intensity variation correction, a laser sampling error correction, a phase correction and the fast Fourier transform. For the InGaAs detector, nonlinearity correction is not required because of its sufficiently linear response.

If the intensity of the received solar radiation varies during the acquisition of an interferogram (due to clouds or aerosols in the path between the FTS-Paris and the Sun), the resulting spectrum will be distorted, since the continuum level of the interferogram will vary for different optical path differences. The I2S corrects this variation by using a method developed by Keppel-Aleks [31]. In this method the interferogram is divided by smoothed DC-coupled detector signals. For interferograms containing less than 10 per cent solar intensity variation, the standard deviation of the retrieved O_2 columns between scans is reduced from 2.5 to 0.25 per cent. This correction allows TCCON instruments to measure accurately through light clouds and aerosols.

IV.3.2 GFIT

GFIT is a non-linear least-squares spectral fitting algorithm designed for the analysis of FTS absorption spectra. It consists of a "forward model", which computes an atmospheric transmittance spectrum for a prescribed set of parameters, and an "inverse method", which compares the calculated spectrum with the measured, and decides how best to adjust the retrieved parameters to achieve a better match.

GFIT calculates one set of the absorption coefficients for each day of measurements, based on the pressure and temperature conditions provided by a meteorological model. The calculated absorption coefficients are then reused for each spectrum acquired on that day, instead of recalculating the absorption coefficients for each spectrum based on the daily changes of pressure and temperature conditions. The use of one set of absorption coefficients per day speeds up the calculations, but it can introduce the error due to the diurnal variation of the temperature near the ground.

GFIT uses a profile-scaling approach instead of a full profile retrieval: It assumes that the volume mixing ratio (VMR) profiles of the gases are known and simply scales these profiles to generate forward-modeled spectra that best fit the data. The results of this scaling approach are volume mixing ratio scale factors (VSFs) for the various fitted gases. This method is faster and simpler than the full profile retrieval and it is also less sensitive to certain types of systematic errors in the shapes of the calculated spectral lines (e.g. ILS, spectroscopic line widths, zero-level offsets, collision narrowing, line mixing), but it could lead to errors when the real atmospheric conditions are very different from what is assumed in the a priori data.

IV.3.3 Gas a priori profiles

A priori profiles of pressure, temperature, geopotential height, and water vapor are generated by the GGG based on the National Centers for Environmental Protection and National Center for Atmospheric Research (NCEP/NCAR) reanalysis [32]. Other gas profiles are generated by subroutine "GSETUP" using empirical models based on the measurements from balloon-borne platforms (MkIV [33], AirCore [34], OMS [35], aircraft (HIPPO [36], START-08 [37], INTEX-NA [38], IMECC [39, 40]), and satellites (ACE-FTS [41], ATMOS [42]). The empirical functions include a secular increase, interhemispheric gradient, seasonal cycle, and stratospheric decay based on the age of air. Fig.IV.1 shows an example of a priori profiles calculated for the Paris site.

IV.3.4 Column-averaged dry-air mole fractions (DMF)

The total vertical column (molecules/cm^2) of a gas G (column$_\mathrm{G}$) is defined as the integral of the mole fraction of the gas $f_G(z)$, multiplied by the total number density $n(z)$, from the surface altitude z_s to the top of the atmosphere:

$$\mathrm{column_G} = \int_{z_s}^{\infty} f_G(z) \cdot n(z) \cdot dz \tag{IV.3}$$

We now give the differential hydrostatic balance equation and, to do so, we consider a thin layer of atmosphere. The pressure difference (dp) between the top and bottom of the layer

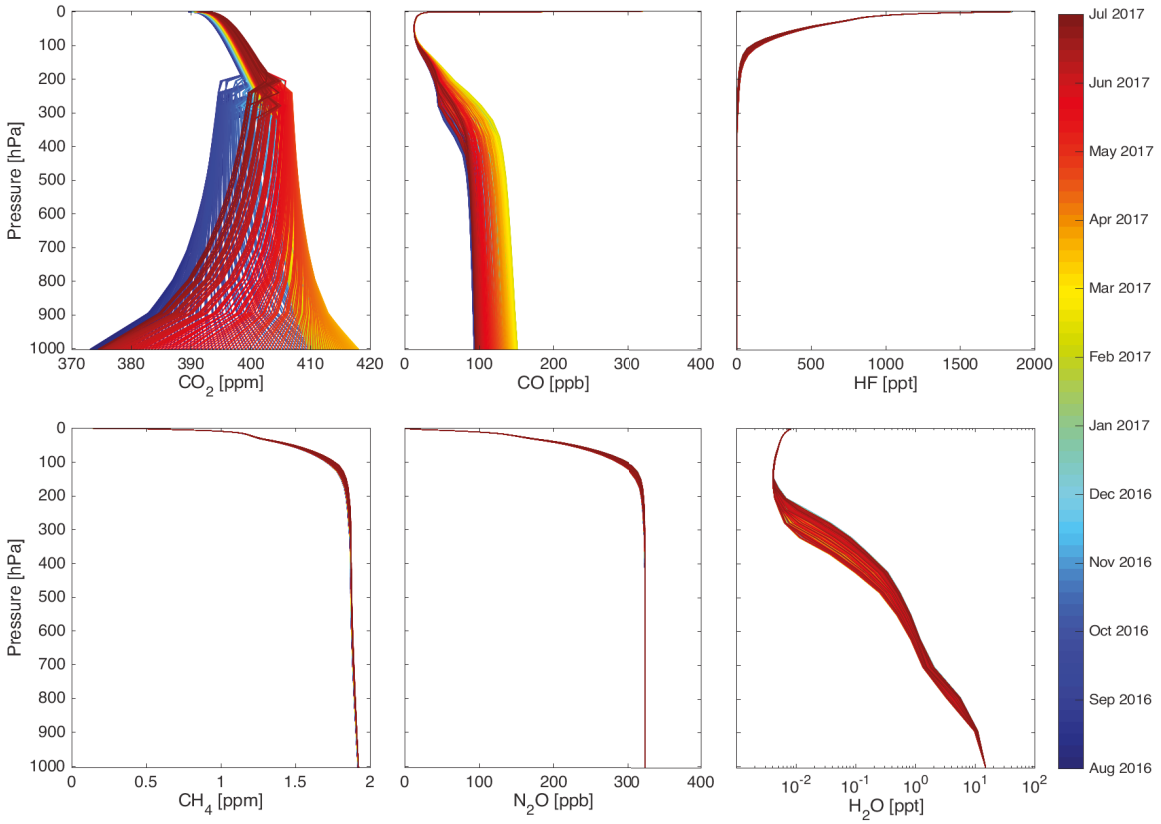

Figure IV.1 – A prior volume profiles calculated for the Paris site. The colour represents the time of year.

is simply the mass per unit area of all the molecules within the layer multiplied by the gravitational acceleration (g):

$$dp = -g \cdot m \cdot n \cdot dz$$

where m is the mean molecular mass (molar mass/N_A, where N_A is the Avogadro constant). Using this equation, Eq.(IV.3) can be re-written as an integral over the pressure

$$\text{column}_\text{G} = \int_0^{p_s} \frac{f_G}{g \cdot m} dp$$

where $p_s = p(z_s)$ is a surface pressure.

As mentioned previously, the VSFs calculated by GFIT for the gas G (VSF_G) are multiplied by the a priori vertical column to get the retrieved vertical column:

$$\text{column}_\text{G}^\text{retrieved} = \text{VSF}_\text{G} \int_0^{p_s} \frac{f_G^\text{a priori}}{g \cdot m} dp \tag{IV.4}$$

The retrieved vertical column amount of a gas G (VC_G) is sensitive to variations in

surface pressure and atmospheric water vapor content, because from:

$$f_G + f_{N_2} + f_{\mathrm{O}_2} + f_{\text{other gases}} = 1 - f_{H_2O}$$

we can derive the dry VMR profile of gas G, $f_G^{dry} = f_G/(1-f_{H_2O})$, easily by dividing through $(1 - f_{H_2O})$:

$$f_G^{\text{dry}} + f_{N_2}^{\text{dry}} + f_{\mathrm{O}_2}^{\text{dry}} + f_{\text{other gases}}^{\text{dry}} = 1$$

Column-averaged dry-air mole fractions (DMF; denoted $\mathrm{X_G}$) are less sensitive to variation in surface pressure and water vapor than vertical columns. DMFs permit direct comparisons of the trace gas measurements during different seasons and between sites. To calculate the DMF, the total vertical column of the gas G is divided by the total vertical column of the dry air:

$$\mathrm{X_G} = \frac{\mathrm{column_G}}{\mathrm{column_{dry\ air}}} \tag{IV.5}$$

The total vertical column of dry air can be determined by two methods. The first method uses the surface pressure (p_s) and the total column of water ($\mathrm{column_{H_2O}}$):

$$\mathrm{column_{dry\ air}} = \frac{P_S}{g_{air} \cdot \mu_{air}^{dry}} - \mathrm{column_{H_2O}} \cdot \frac{\mu_{\mathrm{H_2O}}}{\mu_{air}^{dry}} \tag{IV.6}$$

where $m_{air}^{dry} = 28.964 \times 10^{-3} kg/N_A$ is the mean molecular mass of dry air, $m_{\mathrm{H_2O}} = 18.02 \times 10^{-3} kg/N_A$ is the molecular mass of water and g_{air} is a column averaged gravity, defined by $g_{\text{air}}^{-1} = p_s^{-1} \int_0^{p_s} \frac{dp}{g}$. The second possibility to determine the dry air column is to use the total column of $\mathrm{O_2}$ calculated from the FT spectrum and divide it by the known DMF of $\mathrm{O_2}$, which is equal to 0.2095:

$$\mathrm{column_{dry\ air}} = \frac{\mathrm{column_{O_2}}}{0.2095} \tag{IV.7}$$

The latter option (eq.(IV.7)) is used by TCCON for DMFs calculation because of its advantages as compared to the first option (eq.(IV.6)), such as that errors common to the target gas ($\mathrm{CO_2}$, $\mathrm{CH_4}$, etc) and to $\mathrm{O_2}$ will generally cancel in the column ratio. Finally, by combining (IV.5) and (IV.7) the dry air column averaged mixing ratio of the gas G is obtained

$$\mathrm{X_G} = 0.2095 \frac{\mathrm{column_G}}{\mathrm{column_{O_2}}}$$

IV.3.5 TCCON spectral windows

TCCON FTS instruments record spectra in the near infrared region (NIR) covering the spectral range from 4000 to 11000 $\mathrm{cm^{-1}}$. Fig.IV.2 shows an example of FTS solar absorption spectrum (black) and synthetic transmission spectra of different atmospheric molecules scaled to 0.16 (in order to fit the spectrum scale).

Instead of fitting the whole transmission spectrum, GFIT uses only small spectral regions (microwindows) containing the absorption lines of the target gases. Two $\mathrm{CO_2}$ microwindows (centered at 6220 and 6339 $\mathrm{cm^{-1}}$) and one $\mathrm{O_2}$ microwindow (centered at 7885 $\mathrm{cm^{-1}}$) are

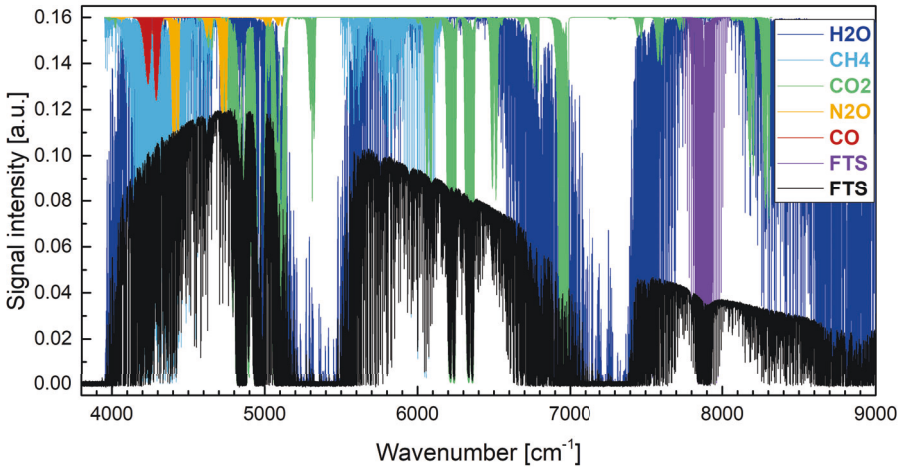

Figure IV.2 – An example of the FTS measured spectrum (dark blue) and theoretical absorption lines of different gases, scaled to 0.16.

used by GFIT for CO_2 DMF retrievals, see Figs.IV.3 and IV.4 respectively. In these figures, calculated (Tc, black) and measured (Tm, gray) absorption spectra overlap. Colored curves are offset and indicate either interfering species (see Fig. legends) or solar lines (Solar, green). The upper panels show fit residuals (Tm-Tc).

GGG uses different spectroscopic line lists to fit the measured spectra. It employs the atmospheric line list, called atm.101 [43], based on the combination of different HITRAN database versions [44–46]. The atmospheric line list is used to generate transmission spectra of the atmospheric gases. The solar line list (called solar_merged.108, [47]) is utilized to generate a solar pseudo-transmission spectrum.

The spectral microwindows for every molecule used by GFIT for gas retrievals are pre-

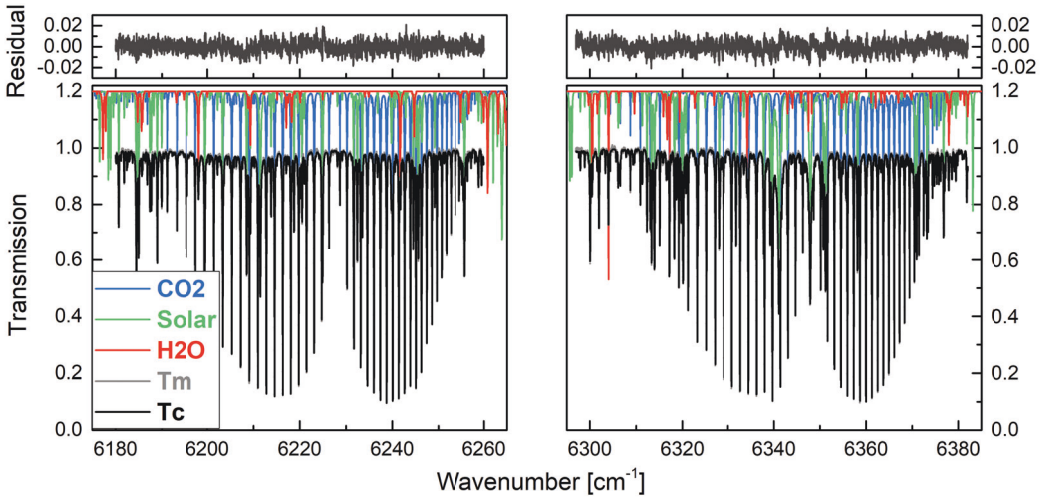

Figure IV.3 – Two CO_2 microwindows used by GFIT for the calculation of CO_2 total column. Measured (Tm) and calculated spectra (Tc) are overlapped, the residuals are shown in the top panels.

Table IV.1 – TCCON spectral windows.

Molecule	Central wavenumber cm^{-1}	Window Width cm^{-1}	Interfering Species
CO_2	6220.00	80.0	H_2O, HDO, CH_4
	6339.00	85.0	H_2O, HDO
CO	4233.00	48.6	CH_4, H_2O, HDO
	4290.40	56.8	CH_4, H_2O, HDO
CH_4	5938.00	116.00	CO_2, H_2O, N_2O
	6002.00	11.10	CO_2, H_2O, HDO
	6076.00	138.00	CO_2, H_2O, HDO
N_2O	4395.20	43.40	CH_4, H_2O, HDO
	4290.40	23.60	CH_4, H_2O, HDO, CO_2
	4290.40	23.60	CH_4, H_2O, CO_2
O_2	7885.00	240.00	H_2O, HF, CO_2
HF	4038.95	0.32	H_2O
H_2O	4565.20	2.50	CO_2, CH4
	4571.75	2.50	
	4576.85	1.90	CH_4
	4611.05	2.20	CH_4
	4622.00	2.30	CO_2
	4699.55	4.00	CO_2, N_2O
	6076.90	3.85	CH_4, HDO, CO_2
	6099.35	0.95	CO_2, HDO
	6125.85	1.45	CO_2, HDO, CH_4
	6177.30	0.83	CO_2, HDO, CH_4
	6255.95	3.60	CO_2, HDO
	6301.35	7.90	CO_2, HDO
	6392.45	3.10	HDO
	6401.15	1.15	H_2O, HDO
	6469.60	3.50	CO_2, HDO
HDO	4054.60	3.30	H_2O, CH4
	4116.10	8.00	H_2O, CH_4
	4212.45	1.90	H_2O, CH_4
	4232.50	11.00	H_2O, CH_4, CO
	6330.05	45.50	H_2O, CO_2
	6377.40	50.20	H_2O, CO_2

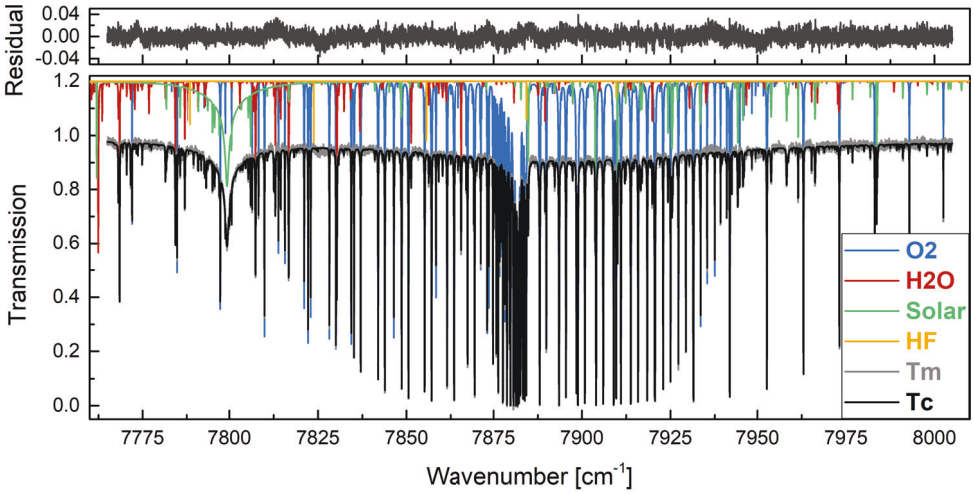

Figure IV.4 – O_2 microwindow used by GFIT for the calculation of O_2 total column. Measured (Tm) and calculated spectra (Tc) are overlapped, the residuals are shown in the top panels.

sented in Table IV.1. If a single molecule is retrieved in multiple windows, the results from the individual windows are averaged.

IV.3.6 Averaging Kernels

Following the approach of Rodgers [29], the retrieved VMR profile ($\mathbf{x}_r$) is related to the true VMR profile ($\mathbf{x}_t$) by

$$\mathbf{x}_r = \mathbf{x}_a + \mathbf{A}(\mathbf{x}_t - \mathbf{x}_a)$$

where $\mathbf{x}_a$ is the a priori used in the retrievals of $\mathbf{x}_r$ and $\mathbf{A}$ is the averaging kernel matrix. The averaging kernel matrix represents the change in the retrieved VMR profile at level i due to a perturbation to the true VMR profile at level j. A perfect measurement would have an averaging kernel equal to the unit identity matrix. But for real measurements with limited vertical resolution, a pertubation at level j will change the retrieval not just at level j, but also at adjacent levels. The i-th row of $\mathbf{A}$ can be regarded as a smoothing function for the altitude corresponding to i. It should be a peaked function, the width of the peak qualitatively describing the vertical resolution of the retrieval.

Since GFIT does a profile scaling retrieval, a perturbation to the true profile at a particular altitude will have the same impact on the retrieval at all altitudes. For example, if we increase the true VMR profile by 50% at 10 km altitude, the retrieved profile might increase by 1% at every retrieval altitude. This means that for profile scaling retrieval, the rows of the averaging kernel matrix all have the same shape and only the amplitudes of the rows differ. Thus the N×N averaging kernel matrix contains only N pieces of information. It therefore makes sense to represent the averaging kernel matrix as a N-vector, defined by the equation

$$a_j = \sum_{i=1}^{N} A_{ij} \frac{\Delta p_i}{\Delta p_j}$$

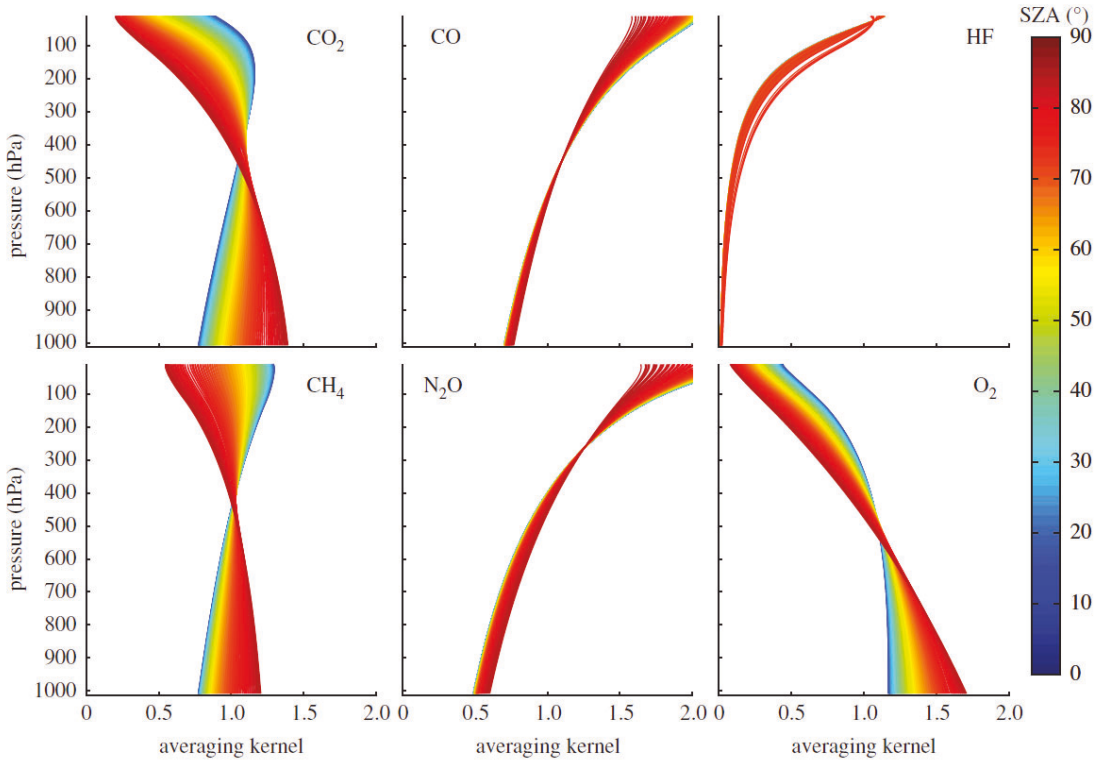

Figure IV.5 – Examples of column averaging kernels, plotted as a function of pressure. The colours represent the solar zenith angle. Source: [6].

where a_j is the column averaging kernel produced by GFIT, A_{ij} are elements of averaging kernel matrix $\mathbf{A}$, Δp_i and Δp_j are the effective thickness of the i'th and j'th pressure levels. So a_j represents the sensitivity of the retrieved total column to a perturbation of the partial column at level j.

In general, the column averaging kernels do not differ much from one spectrum to another (for the same solar zenith angle) and every TCCON site has very similar column averaging kernels. GFIT does not routinely calculate column averaging kernels, because it takes significant amount of calculation time and the resulting kernels would be nearly identical. The column averaging kernels calculated for the Lamont site (Oklahoma, USA) are shown in Fig.IV.5.

IV.3.7 TCCON Calibration to WMO standards

To use the TCCON measurements for investigating regional and global scale carbon science questions and for providing a transfer standard between the in situ network and the satellite retrievals of total column CO_2, TCCON retrievals must be placed on the same absolute calibration scale as the in situ network, the World Meteorological Organization (WMO) scale.

To tie the TCCON measurements to the WMO gas standard scale, precise and accurate in situ instruments are flown on airborne platforms above the TCCON stations, and measure

profiles of the gases of interest while the TCCON station is measuring the total column amounts. The in situ profiles ($\mathbf{x}_h$) are then smoothed using TCCON averaging kernels ($\mathbf{A}$) and the scaled TCCON a priori profiles ($\mathrm{VSF} \cdot \mathbf{x}_a$), as described in [48]:

$$\mathbf{x}_s = \mathrm{VSF} \cdot \mathbf{x}_a + \mathbf{A}(\mathbf{x}_h - \mathrm{VSF} \cdot \mathbf{x}_a) \tag{IV.8}$$

where $\mathbf{x}_s$ is the smoothed in situ profile. Then Eq.(IV.8) is integrated vertically:

$$\mathbf{c}_s = \mathrm{VSF} \cdot \mathbf{c}_a + \mathbf{a}^\intercal(\mathbf{x}_h - \mathrm{VSF} \cdot \mathbf{x}_a)$$

where $\mathbf{c}_s$ is the smoothed column-averaged DMF, $\mathbf{c}_a$ is the column-averaged DMF from integrating the a priori profile and $\mathbf{a}$ is a vector containing the FTS dry pressure weighted column averaged kernel. For more details see [48].

There are more than 30 independent profile measurements of CO_2 above TCCON sites. Fig.IV.6 shows the comparison of TCCON X_{CO_2} with X_{CO_2} obtained from in situ profile measurements. It includes different aircraft and AirCore campaign measurements at different TCCON sites. The data is fitted with a linear least squares and is forced to the origin (see Fig.IV.6). The consistency between TCCON calibrations at the different sites and for different seasons is excellent.

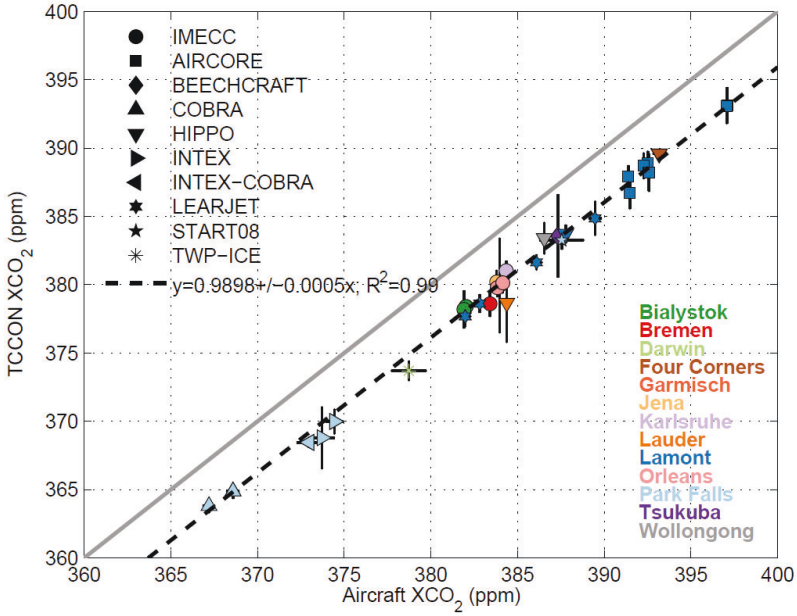

Figure IV.6 – The TCCON calibration curve for X_{CO_2}. Source: [30]

The calibration factors for different molecules are presented in the table IV.2. Thus, the reported TCCON column averaged DMFs are produced by dividing the retrieved columns by scaling coefficient factors.

For each version of the GGG spectroscopy, which is updated about once in four years, new scaling factors is need to be calculated and applied to the TCCON data.

Table IV.2 – TCCON scale factors.

Molecule	Scale factor ($X_{gas}^{TCCON}/X_{gas}^{aircraft}$)	Scale factor error
CO_2	0.9898	0.001
CO	1.0672	0.02
CH_4	0.9765	0.002
N_2O	0.9638	0.01
H_2O	1.0183	0.01

IV.3.8 Correction of the airmass dependent artefact

All TCCON X_{CO_2} data have the airmass dependent or solar zenith angle (SZA) dependent artefact that causes the retrievals to be up to 1 % larger at 20° than at 80° SZA [6]. The airmass dependence arises from the variation in retrieved O_2 and CO_2 columns. The airmass dependent changes in X_{CO_2} occur at clean air sites (Park Falls, Darwin and Lauder) and at times of the year when there is no vegetation growth and therefore no cause for a real diurnal change of X_{CO_2}.

The physics based solution of this artefact is not found yet, it is probably resulting from the spectroscopic inadequacies and instrumental problems. Meanwhile, the airmass dependent artefact (ADA) is corrected empirically. We assume that, on a given day, any variation in X_{CO_2} that is symmetrical about noon is an artefact and any variation that is antisymmetric is real. Fig.IV.7(left panel) shows an example of uncorrected X_{CO_2} (expressed as X_{CO_2} daily anomalies: the differences between the X_{CO_2} values and the daily median values) calculated for the Lamont site.

The correction of the ADA for is performed by

$$X_{gas}^{corrected} = \frac{X_{gas}^{uncorrected}}{1 + \beta S(\theta_i)}$$

where $\beta S(\theta_i)$ represents the airmass dependent artefact. $S(\theta_i)$ is defined by

$$S(\theta_i) = \left(\frac{\theta_i + \theta_0}{90 + \theta_0}\right)^3 - \left(\frac{45 + \theta_0}{90 + \theta_0}\right)^3$$

The parameter β is defined for each gas, for CO_2 it is equal to -0.0068. Fig.IV.7(right panel) shows an example of corrected X_{CO_2} daily anomalies. In order to verify, that the ADA correction works properly for the TCCON-Paris site, we have calculated the X_{CO_2} anomalies for our dataset (see Fig.IV.8). No SZA dependence has been found, X_{CO_2} anomalies are stable over whole range of SZA and uniformly distributed over zero ppm. Thus, the ADA correction works well for the Paris data.

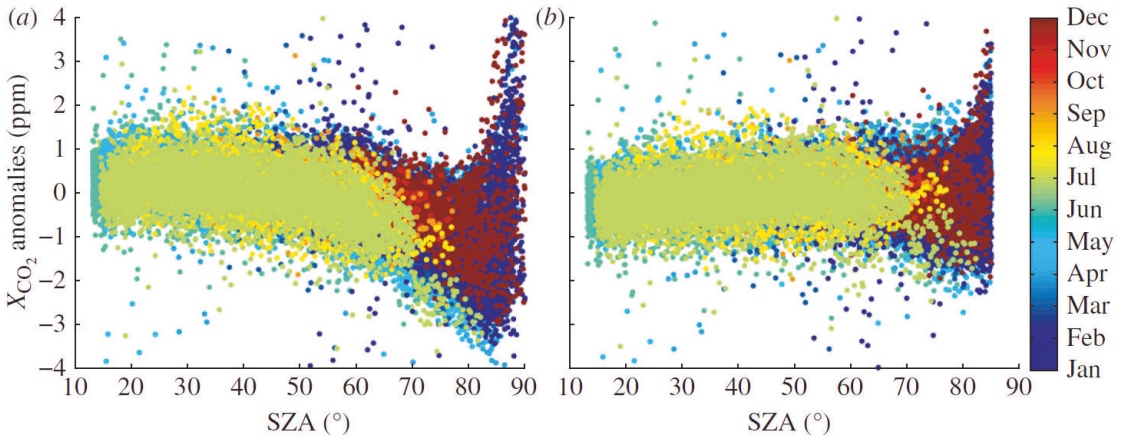

Figure IV.7 – The X_{CO_2} anomalies calculated for Lamont site. The left panel shows X_{CO_2} anomalies without the airmass dependent artefact correction, and the right panel with the airmass dependent corrected. Source: [6].

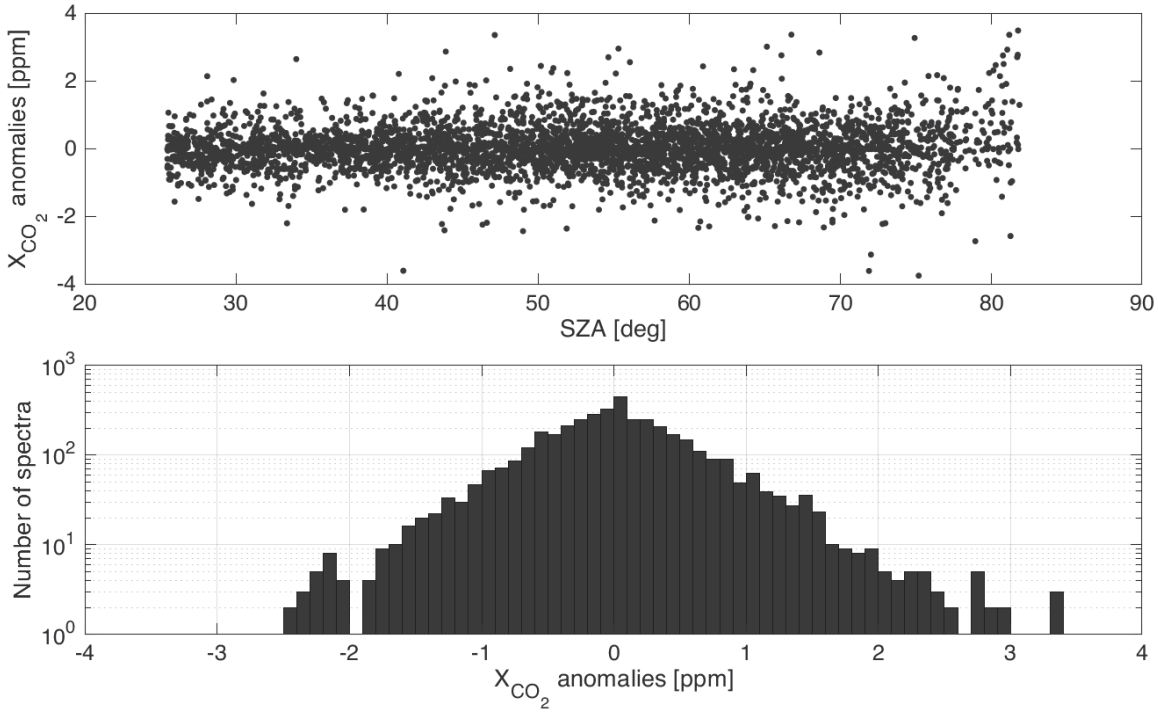

Figure IV.8 – The top panel shows the X_{CO_2} anomalies calculated for the Paris site for three years of measurements. The bottom panels shows the distribution of the X_{CO_2} anomalies.

V – TCCON dataset and Quality control

The Total Carbon Column Observing Network (TCCON) was established in 2004 with only few operational sites. Since then the network has grown to 25 operational sites (in 2017) around the globe. Each site uses the same type of instrument and follows the same optical alignment procedure of the instrument, data acquisition setting and protocol, data processing and analysis software, and calibration traceable to the World Meteorological Organization's gas scale. The datasets from each site are available at the Caltech Library Research Data Repository: https://tccondata.org.

This chapter is dedicated to the description of data produced by TCCON station in Paris (TCCON-Paris). Section V.1 describes the Paris dataset available from the TCCON data archive. Section V.2 describes GGG data filters and quality control steps. The improvements of the X_{CO_2} measurement precision and steps towards reaching the goal of 0.4 ppm are discussed in section V.3 and V.4.2. The TCCON-Paris solar tracker has been updated in May 2018. Its new performance is discussed in section V.4. With the update of the solar tracker, a phase correction problem has appeared (see section V.5).

V.1 TCCON Paris dataset

FTS measurements at the Paris site have started in 2007 [49]. Only in September 2014, however, the requirements for TCCON measurements have been fulfilled. Since then, TCCON-Paris has become an official TCCON site and its data products can be found at the TCCON archive. Measured spectra are analyzed using the TCCON software package GGG (see Section IV.3) three months after their acquisition. The entire output of the GGG retrieval is delivered to the TCCON data archive (https://tccondata.org) where they are converted into the netCDF (NCDF) format. The delay between measurements and data submission to the archive usually does not exceed 12 months and is usually between 6 and 12 months.

NCDF files contain the time series of the retrieved values of dry air column-averaged mixing ratios (X_{gas}) of CO_2, CO, N_2O, CH_4, H_2O, HDO and HF, Fig. V.1. It also contains auxiliary data used for X_{gas} retrievals including surface pressure, temperature and a priori profiles. GGG does not calculate averaging kernels (AK) for each spectrum, instead NCDF files include a set of AK calculated for Lamont site, because AK varies slightly between sites and seasons, and depend mainly on the solar zenith angle.

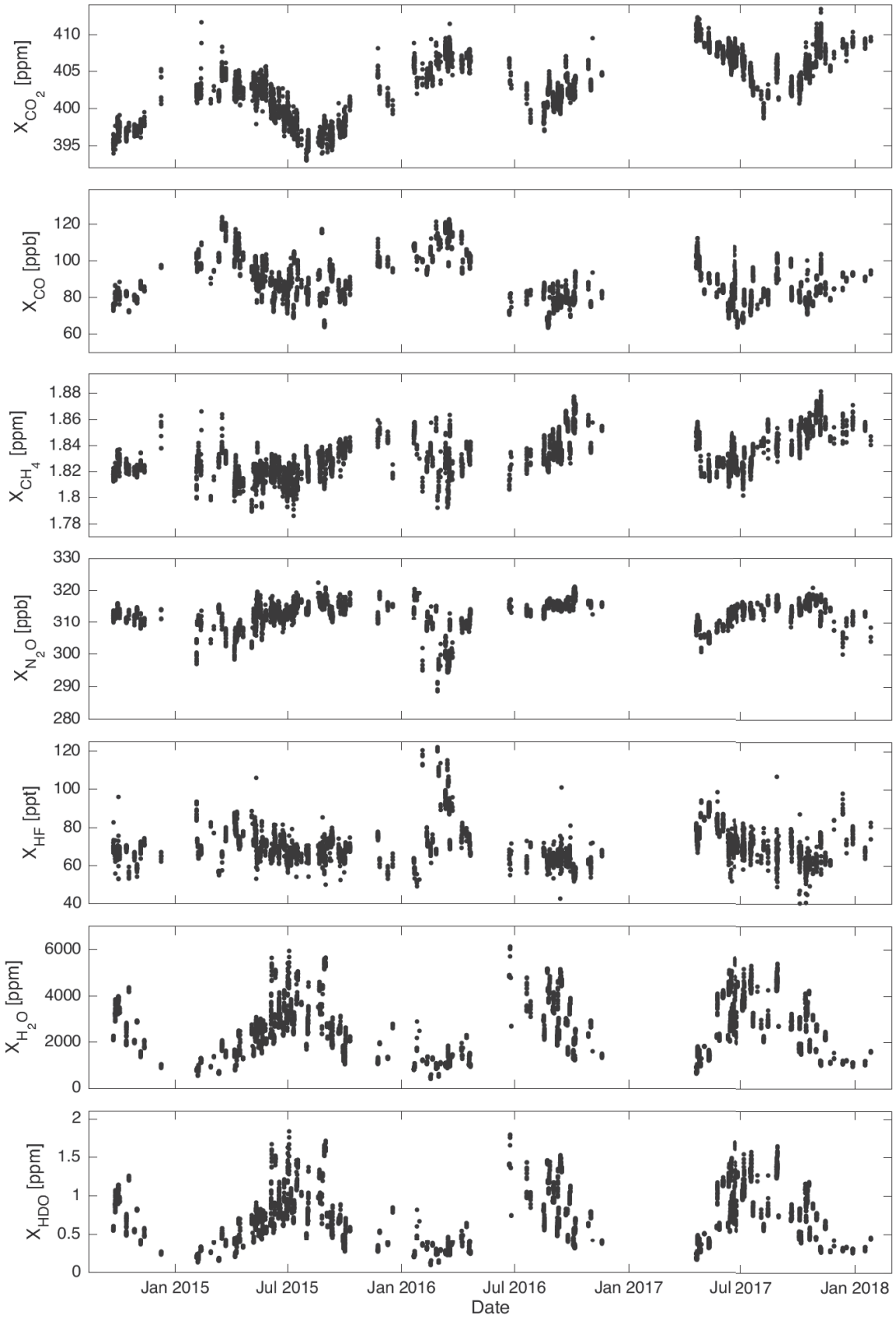

Figure V.1 – Entire TCCON-Paris data set until January 2018, available at the TCCON data archive.

V.2 Data quality control

The TCCON Paris data passes through a series of quality control filters and a visual check identifying the presence of measurement artefacts.

V.2.1 Preliminary filtering and spectra storage

TCCON has currently no centralized storage of measured spectra because this would take too much of storage space: one spectrum takes ∼9 MB on the hard drive, and there are more than 3.6 million of data points at the TCCON archive, so in order to store all network spectra, it would take 3160 TB on the hard drive, which does not seem feasible in the near future.

Our spectra storage routine includes four computers (PC) intended for different purposes:

- PC 1 controls the spectrometer and the solar tracker. All of the measured spectra (TCCON, NDACC and cells) are recorded on this computer. Recorded spectra are stored only one year, and at the beginning of each year, they are suppressed.
- PC 2 reads all spectra from PC 1 (via an ethernet connection) and creates a list of "bad" and "good" spectra. "Bad" spectra are either corrupted or suffer from low signal to noise (currently, a low signal to noise threshold of 50 is used). The remaining spectra are classified "good". The "good" spectra are then saved on PC 2, where they are stored and used for the creation of input files for GGG.
- PC 3 is used as a storage of all 'good' spectra and auxiliary data (pressure, temperature etc.). It is also used for the analysis of NDACC spectra by PROFFIT.
- PC 4 is operated under Linux and is used for the analysis by the GGG software. The results of the GGG calculations are copied to PC 3 for storage and backup.

All data is also copied and stored on an external hard drive. The need for such a large number of copies is due to the value of the spectra. The release of a new version of GGG is accompanied by a reanalysis of all spectra i.e. creating a new version of the data. If for some reasons the spectra are lost, then the release of the new data version will be impossible and the old data version will be not consistent within the network.

V.2.2 Flag filter

Within the GGG package, there is a subroutine which marks the spectra with a flag index. It takes each spectrum and checks all of the auxiliary (pressure, temperature, solar zenith angle and others) and retrieved parameters (gas columns, X_{gas} and errors). If one of the parameters lies out of the permitted range, it will be marked by a flag index. For each spectrum, the standard flag value is zero if all of the parameters are within the permitted range. If one parameter is outside the range a non zero flag value is assigned (if there are several parameters out of range, the smallest index will be indicated). The time series of flag indexes for TCCON Paris data is presented in Fig.V.2. In the figures of this chapter the grey colour represents spectra with a flag value 0 and blue points represent flagged spectra.

Table V.1 gives a statistics of the flag index obtained for our data set and the range of allowed values. The total number of measured spectra between September 2014 and January

2018 is 28750, 1427 of them (4.96%) are flagged, half of them (721 points) are flagged because of the fractional variation of solar intensity (see section V.2.4). The description of each flag is presented in Table V.1.

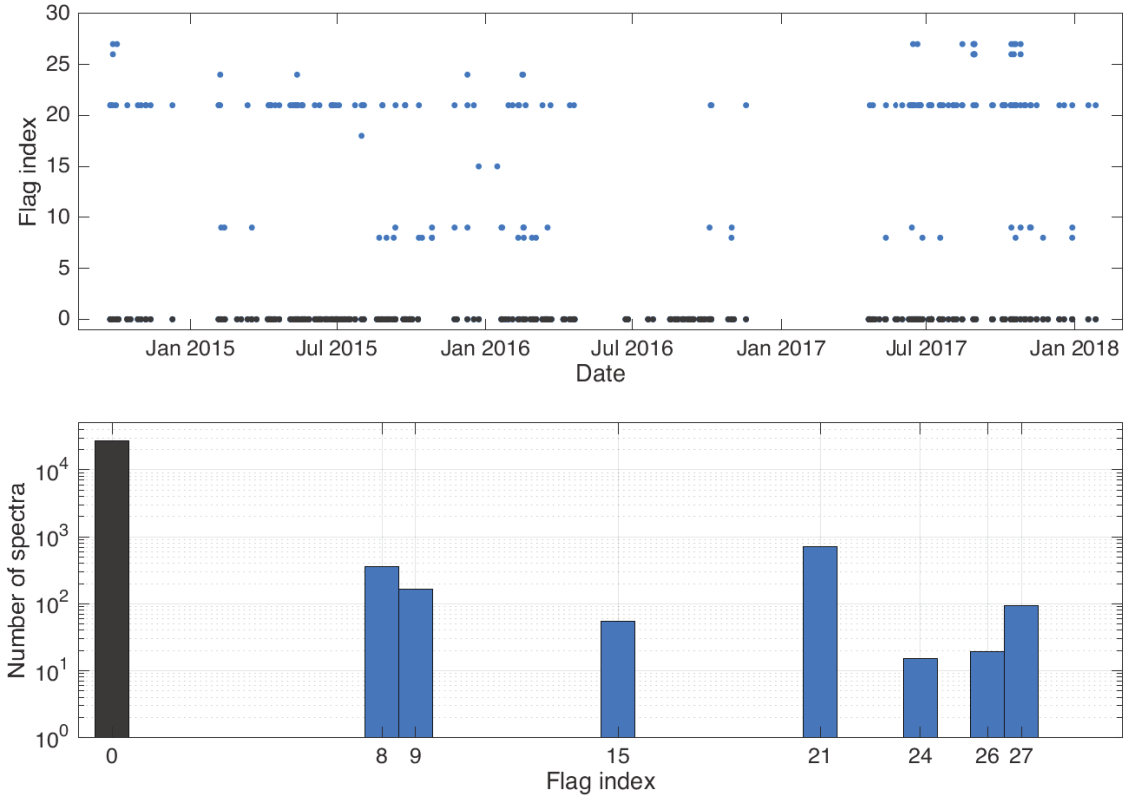

Figure V.2 – Top panel is the time series of flag values for the TCCON Paris datasets. The bottom panel shows the number of spectra corresponding to the different flag indexes.

Table V.1 – Flag indexes obtained for TCCON Paris data between September 2014 and January 2018.

Flag index	Description	Allowed range	Number of flags
0	Good spectra	-	27323
8	Pressure derived altitude	0-0.9 [km]	358
9	Solar Zenith Angle	0-82 [deg]	166
15	Internal Temperature	15-35 [°C]	154
21	Fractional Variation of Solar intensity	0-5 [%]	721
24	X_{air}	0.96-1.04	15
26	X_{HF}	0-500 [ppt]	19
27	$X_{HF\ error}$	0-500 [ppt]	93

V.2.3 X_{air} - instrument stability indicator

The control parameter X_{air} is calculated by GFIT as an indicator for instrument stability. It is not part of the official TCCON data product and calculated by

$$X_{air} = 0.2095 \frac{\text{column}^{p_s}_{\text{dry air}}}{\text{column}_{O_2}}$$

where $\text{column}^{p_s}_{\text{dry air}}$ is the column of dry air calculated from the surface pressure measurements (p_s) and the column of water (column_{H_2O}):

$$\text{column}^{p_s}_{\text{dry air}} = \frac{p_s}{g_{air} \cdot \mu_{\text{dry air}}} - \text{column}_{H_2O} \frac{\mu_{H_2O}}{\mu_{\text{dry air}}}$$

where $\mu_{\text{dry air}}$ is the molar mass of dry air, μ_{H_2O} is the molar mass of water and g_{air} is a column averaged gravity acceleration defined by

$$\frac{1}{g_{air}} = \frac{1}{p_s} \int_0^{p_s} \frac{dp}{g}$$

where g is the gravity acceleration as a function of pressure altitude.

For an O_2 measurement with accurate spectroscopy, surface pressure, and H_2O retrievals, X_{air} would have a value of 1.0. However, the typical X_{air} value for TCCON measurements is about 0.98 and exhibits a small diurnal variation because the O_2 spectroscopy is an airmass dependent [50]. Large (1%) deviations from 0.98 indicate problems such as an error in surface pressure, spectra with ghosts, spectra with a poor instrument optical alignment, or an error in the time assigned to the spectrum.

The time series of X_{air} is presented in Figure V.3. For a stable instrument X_{air} should be consistent between different days of measurements and should not change during the course of a day. It is one of the first parameters to be checked in order to reveal problematic data. By checking this parameter we have identified few problematic days in August 2017, which were excluded from the data set.

According to TCCON specifications, X_{air} values are ranging from 0.96 to 1.04. This range covers 99.95% of our spectra and does not filter out points lying out of the main distribution, for example, points below 0.97 and above 1.005 are lying beyond of the main distribution (see histogram). The range of X_{air} could be more strict, for example, the range from 0.978 to 0.997 covers 95.7% of the spectra and filters out all the tails. The median value of X_{air} in Paris is 0.986.

V.2.4 Fractional variation of solar intensity (FVSI)

The recorded interferograms could suffer from variability of the DC level caused by the passage of clouds or aerosols while recording the interferogram. The I2S subroutine, which converts interferograms to spectra, performs an automatic correction of DC variability and records the variability of the uncorrected interferogram (see section IV.3.1). The standard range of allowed FVSI values is between 0 and 5%. The time series and histogram of FVSI for the Paris dataset is shown in Fig.V.4. 97.5% of measured spectra pass the FVSI filter and 74.8% of measured spectra have their FVSI in the range between 0 and 0.5%.

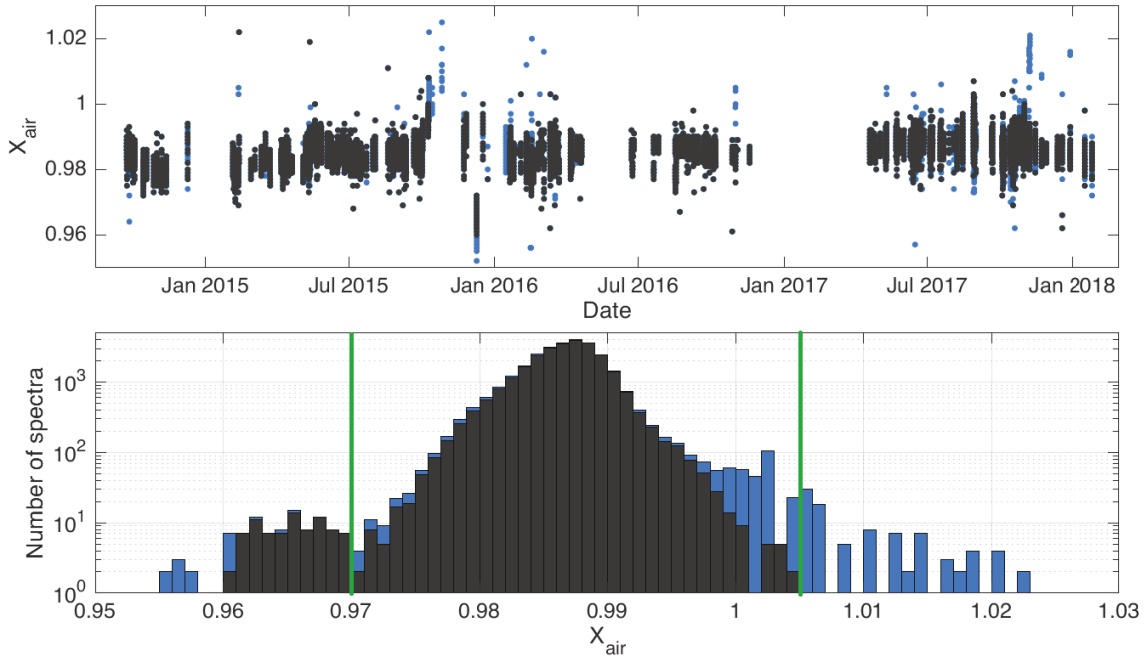

Figure V.3 – The top panel is a time series of X_{air}. The bottom panel gives the histogram of X_{air} with bin width of 0.001. Dark grey colour represents the data with flag=0; data with flag $\neq$ 0, i.e. 8, 9, 15 etc., is shown in blue colour as an additional to the dark grey columns.

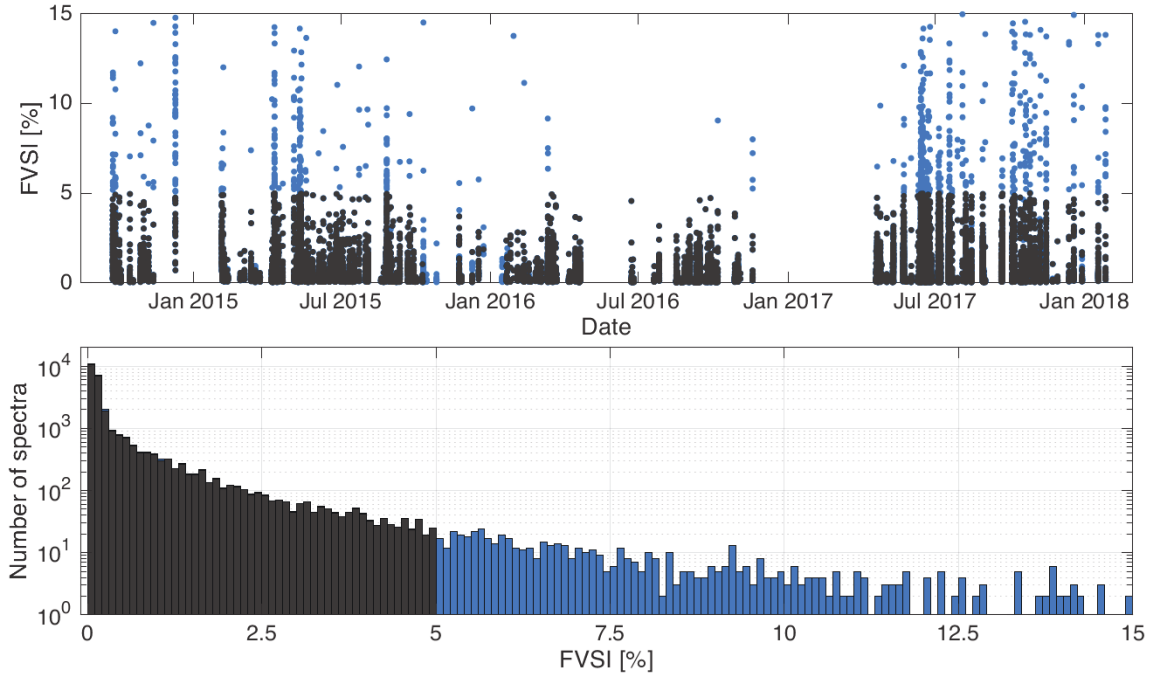

Figure V.4 – The top panel is a time series of FVSI. Bottom panel is a histogram of FVSI, bin width is 0.1%. Dark grey colour for data with flag=0, blue for flag $\neq$ 0.

V.2.5 Solar Zenith Angle

The solar zenith angle is calculated by the GGG subroutine RUNLOG. RUNLOG calculates ZPD time for each spectrum and computes the astronomical solar zenith angle (SZA) by using the latitude and longitude of the site. The time series of SZA is shown in Fig.V.5. The allowed range of SZA is between 0 and 82°. The limit of 82° is used because above this value the total TCCON error budget increases dramatically [30]. For the Paris site only 219 (0.76%) spectra have a SZA exceeding 82°. The minimum SZA during winter is 72° and 25.4° during summer.

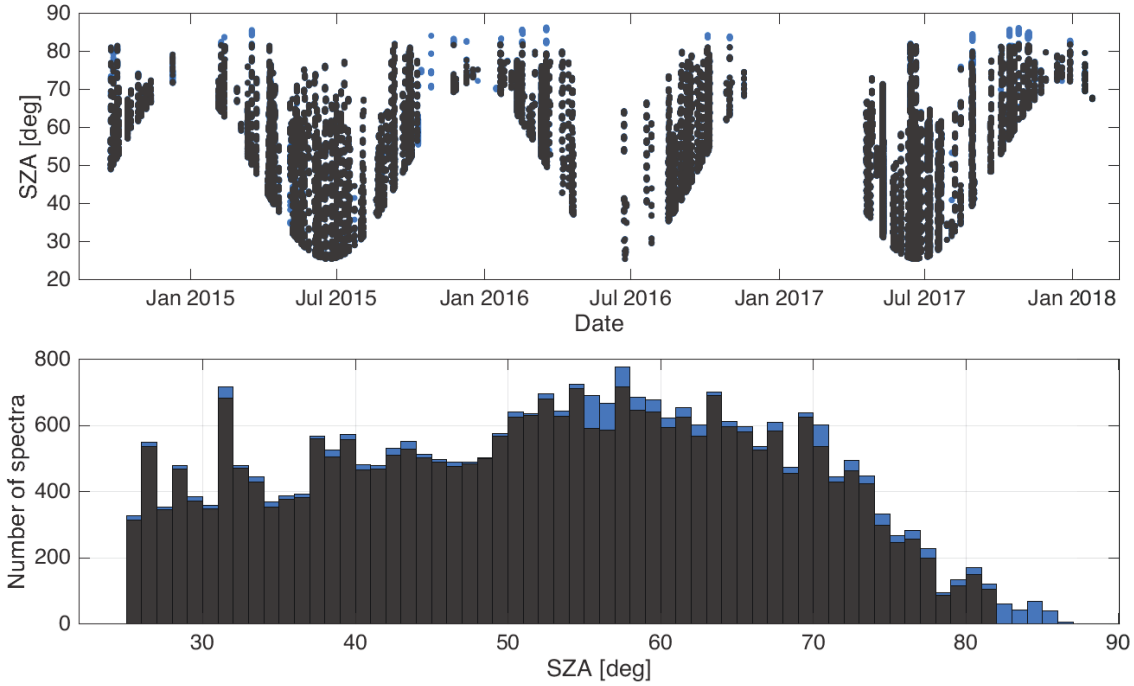

Figure V.5 – Top panel is a time series of SZA. Bottom panel is a histogram of SZA, bin width is 1°. Dark grey colour for data with flag=0; blue colour represents the data with flag≠ 0 as an addition to the dark grey columns.

V.2.6 Pressure derived altitude

The surface pressure measurements are used to calculate a pressure derived altitude for each spectrum. In general, this altitude value differs from the true altitude by up to 0.1 km mainly due to errors in the pressure/temperature model provided by NCEP/NCAR. Thus there are two possibilities: 1) to have the altitude correct, but the surface pressure wrong, or 2) to have the surface pressure correct, but the altitude wrong. It was empirically found that the latter option produces better results for gases whose volume mixing ratio profile is fairly constant in the troposphere (e.g. CO_2, CH_4, O_2, N_2O, HF). The pressure derived altitude time series is presented in Fig. V.6. All values below zero are filtered out. For the Paris site, the median value of the pressure derived altitude is 60 m above sea level, which is equal to the true geometric altitude of the site.

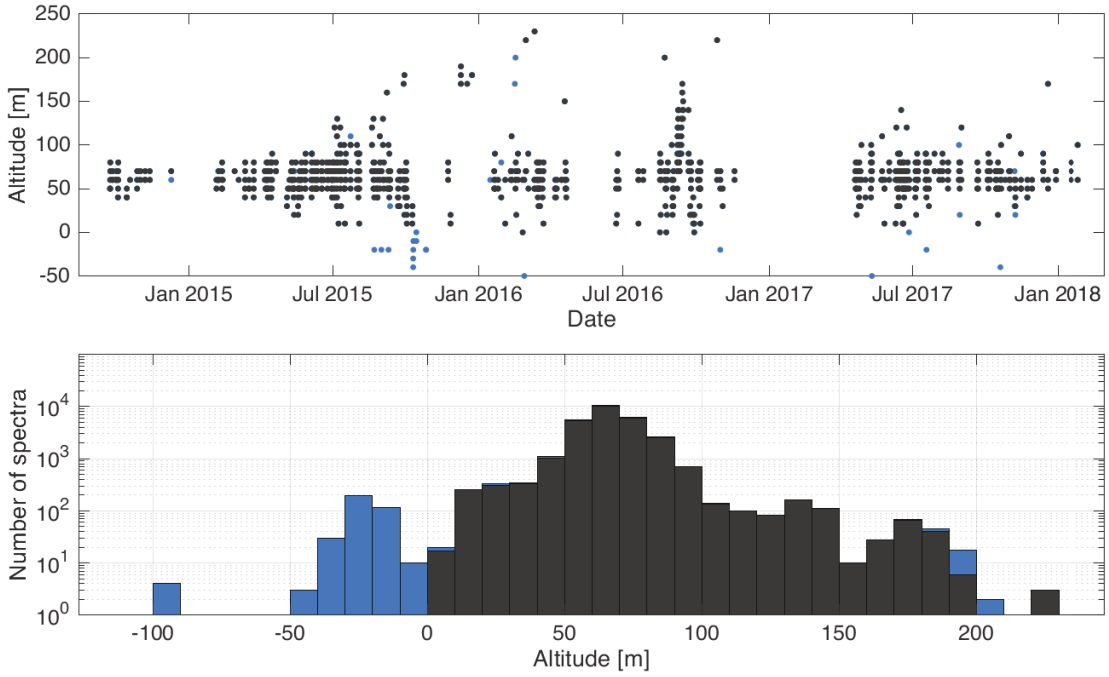

Figure V.6 – The top panel is a time series of pressure derived altitude. The bottom panel is a histogram of pressure derived altitude, and bin width is 10 m. Dark grey colour for data with flag=0, blue for flag $\neq 0$.

V.2.7 Internal Temperature and X_{HF}

Internal temperature is a temperature measured inside of the spectrometer. The spectrometer is installed inside a room equipped with air condition, which was broken during summer 2017. This failure resulted in the temperatures above the limit of 35°C.

X_{HF} and $X_{HF\ error}$ have exceeded the allowed values between 0 and 500 ppt. This is primarily caused by the low signal to noise ratio near the absorption line of HF, GFIT fits only one line of HF centred at 4039 cm^{-1}.

V.3 The precision of X_{CO_2} measurements

In 2011, TCCON claimed the precision of X_{CO_2} measurements to be better than 0.25% (∼1 ppm) [6] and the current goal is to achieve a precision of better than 0.1% (∼0.4 ppm).

The precision of X_{CO_2} calculated by GGG is called $X^{error}_{CO_2}$ and included in the NCDF files. $X^{error}_{CO_2}$ gives a measure of the measurement to measurement variability of the dataset, i.e., the precision. To compute $X^{error}_{CO_2}$, GGG calculates the difference in the column amounts that are close in time (∼5 minutes), and divides that by the quadrature sum of their GFIT-calculated error bars. The average value of this ratio is then multiplied by the $VSF^{error}_{CO_2}$ to determine the $X^{error}_{CO_2}$.

V.3.1 Comparison of $X^{error}_{CO_2}$ at Paris with $X^{error}_{CO_2}$ at other sites

Each site is supposed to use the same type of instrumentation, data acquisition and setting, data processing and analysis software, and calibration traceable to the World Meteorological Organization's gas scale. However, there are still minor differences between sites. All sites use the IFS Bruker 125HR or upgraded 120M instruments, but solar trackers may vary: some sites use a custom instrument and some a commercial solar tracker. The solar tracker mirror coatings can degrade, leading to a degradation of the signal. If the FTS is not kept well aligned, the instrumental line shape could depart from ideal, leading to errors in the retrievals. The acquisition time of one spectrum (75 s is prescribed at OPD of 45 cm) could also differ between sites, depending on the site features (weather conditions, technical problems and so on).

A comparison of the annual median values of $X^{error}_{CO_2}$ for sites being operational between 2015 and 2017 is presented in Fig.V.7. Table V.2 provides the information about the sites used in Fig.V.7.

For sites #11, 14, 15, 18 and 23 $X^{error}_{CO_2}$ value is lower than the 0.4 ppm. Site #27 (Zugspitze, Germany) has the biggest $X^{error}_{CO_2}$ above 1.3 ppm. For the TCCON-Paris site (#20) $X^{error}_{CO_2}$ is between 0.53 and 0.69 ppm, which is similar to the rest of the sites. In the next section we will focus on the improvement of TCCON-Paris $X^{error}_{CO_2}$ value.

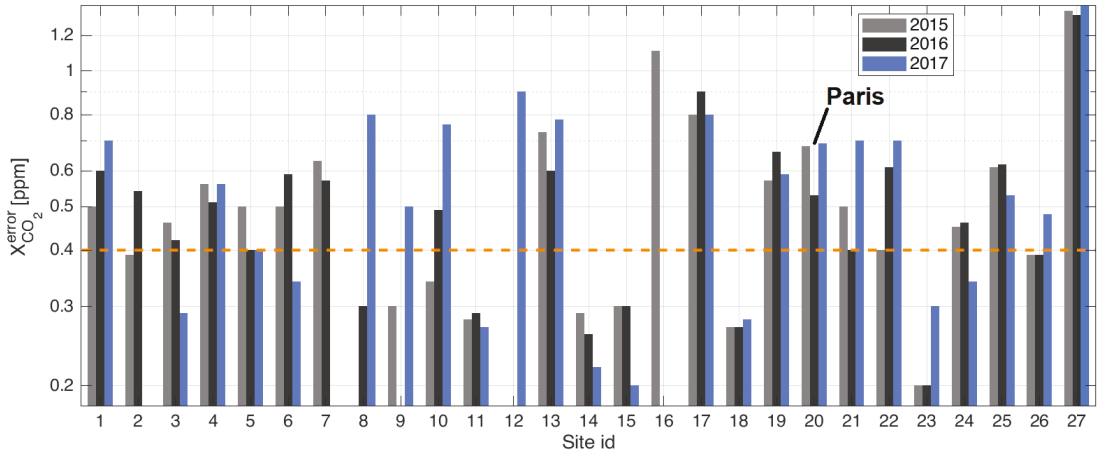

Figure V.7 – The comparison of $X^{error}_{CO_2}$ for all TCCON sites. The different colours indicate years. The horizontal dashed line marks the 0.4 ppm target.

Table V.2 – Overview of $X^{error}_{CO_2}$ for different sites and years.

Site index	$X^{error}_{CO_2}$, ppm (number of spectra) 2015	2016	2017	Site name
1	0.50 (14854)	0.60 (4484)	0.70 (10656)	Ascension Island
2	0.39 (9520)	0.54 (3081)	-	Anmyeondo, South Korea
3	0.46 (21218)	0.42 (21714)	0.29 (3527)	Bialystok, Poland
4	0.56 (1442)	0.51 (3139)	0.56 (1150)	Bremen, Germany
5	0.50 (33374)	0.40 (76111)	0.40 (62556)	CalTech, Pasadena, California, USA
6	0.50 (33033)	0.59 (22479)	0.34 (3819)	Darwin, Australia
7	0.63 (77255)	0.57 (45831)	-	Edwards, CA, USA
8	-	0.30 (4626)	0.80 (48760)	East Trout Lake, Canada
9	0.30 (3680)	-	0.50 (3461)	Eureka, Canada
10	0.34 (11983)	0.49 (9010)	0.76 (9447)	Garmisch, Germany
11	0.28 (148)	0.29 (3130)	0.27 (6966)	Izana, Tenerife, Spain
12	-	-	0.90 (43544)	JPL, Pasadena, California, USA
13	0.73 (10096)	0.60 (7136)	0.78 (18447)	Saga, Japan
14	0.29 (7302)	0.26 (7871)	0.22 (7404)	Karlsruhe, Germany
15	0.30 (65648)	0.30 (41945)	0.20 (46681)	Lauder, New Zealand
16	1.11 (7238)	-	-	Manaus, Brazil
17	0.80 (58677)	0.90 (51970)	0.80 (39080)	Lamont, Oklahoma, USA
18	0.27 (15571)	0.27 (20893)	0.28 (9645)	Orleans, France
19	0.57 (32826)	0.66 (25343)	0.59 (27755)	Park Falls, Wisconsin, USA
20	0.68 (8481)	0.53 (6464)	0.69 (6176)	Paris, France
21	0.50 (34526)	0.40 (29949)	0.70 (32906)	Reunion Island
22	0.40 (5163)	0.61 (6127)	0.70 (3464)	Rikubetsu, Hokkaido, Japan
23	0.20 (13200)	0.20 (16133)	0.30 (11948)	Sodankyla, Finland
24	0.45 (7503)	0.46 (4904)	0.34 (11981)	Ny Alesund, Spitzbergen, Norway
25	0.61 (19367)	0.62 (16499)	0.53 (13059)	Tsukuba, Ibaraki, Japan
26	0.39 (21697)	0.39 (25852)	0.48 (9447)	Wollongong, Australia
27	1.36 (4294)	1.33 (6868)	1.46 (5161)	Zugspitze, Germany

V.3.2 Optimal number of scans for the Paris instrument

The acquisition time per interferogram recommended by TCCON is about 75 seconds at a spectral resolution of 0.02 cm^{-1}, however, for most of the sites, this time is much smaller due to the site's features. For the Paris instrument, the scanner motor operates at the scanning velocity of 40 kHz with the corresponding acquisition time of one interferogram (one scan) of ∼20 seconds. In April 2017, in order to increase the number of scans, we have modified our acquisition setup by adding a backward scan, when the scanner goes from MPD to ZPD. This setup is denoted by F1B1. The forward and backward scans are not averaged. Instead, they are converted into individual spectra (one made in the forward scan and one made in the backward scan) by the I2S program (see section IV.3.1). The F1B1 setup doubles the number of acquired spectra without losing time (required for the scanner to return to ZPD), but the acquisition time for one spectrum still is ∼20 seconds.

In order to increase the acquisition time and to gain in signal to noise ratio, we have

made a few tests with an increased number of scans. We have tested three setups: F1B1 (1 forward and 1 backward scans, 20 seconds per spectrum), F2B2 (2 forward and 2 backward scans, 40 seconds per spectrum) and F4B4 (4 forward and 4 backward scans, 80 seconds per spectrum). The results are presented in Fig.V.8. As expected, increasing the number

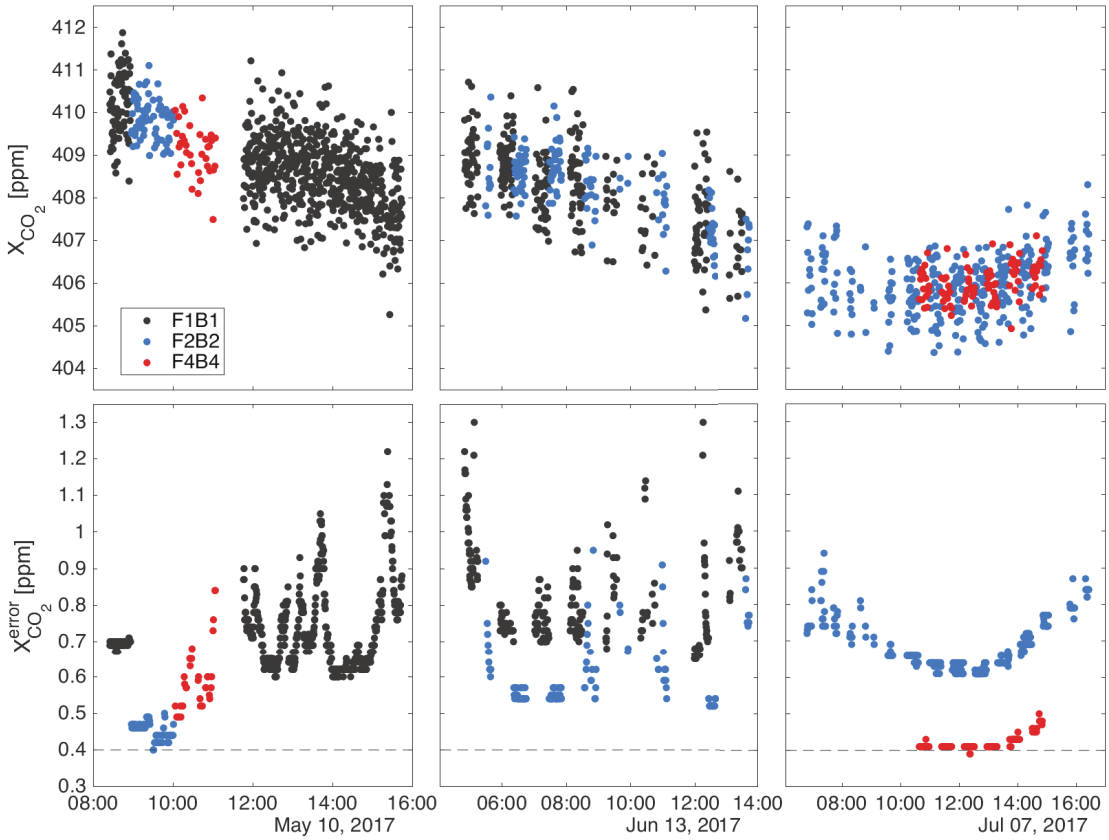

Figure V.8 – Comparison of three different acquisition setups: F1B1, F2B2 and F4B4. Top panels are X_{CO_2}, bottom panels are $X^{error}_{CO_2}$ for three test days.

of scans improves the precision of measurements. The new setups F2B2 and F4B4 show better precision and data consistency then F1B1 setup. However, on May 10 F4B4 does not have better precision than F2B2. This is caused by the specificity of averaging forward and backward scans. Let's consider F4B4 as an example. Four forward scans are acquired with a delay between each scan taken by backward scans, see Fig. V.9. If during the last two forward (80 to 100 and 120 to 140 seconds) and two backward scans (100 to 120 and 140 to 160 seconds) we have a significant variation of the source intensity (for example cloud passage), then the result of averaging forward and backward scans would be corrupted. F4B4 has the same acquisition time as F1B1 at the scanner velocity of 10 kHz, but it is more sensitive to cloudy sky conditions. On June 13 we have compared only the F1B1 and F2B2 setups because this was a cloudy day. The lowest value of $X^{error}_{CO_2}$ for F1B1 setup is 0.64 ppm and 0.51 ppm for F2B2. Then it was decided to switch routine setup to F2B2. On July 7 we have made an additional comparison of F2B2 and F4B4, because the day was very clear, which is quite rare for cloudy Paris prone to aerosols pollution. Under this conditions the

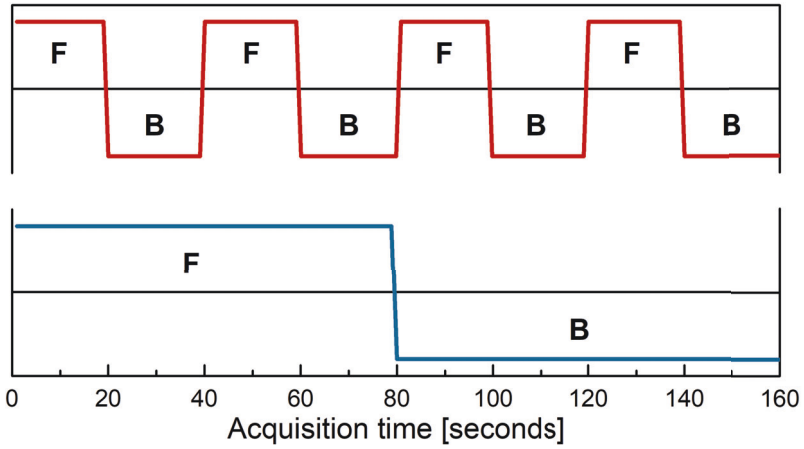

Figure V.9 – Schematic illustration of the difference between F4B4 at 40 kHz (red curve) and F1B1 at 10 kHz (blue curve).

$X^{error}_{CO_2}$ for F4B4 has reached the desired 0.4 ppm while F2B2 reached only 0.6 ppm. Despite these results on 7 July, the decision was to stay with F2B2 which is better suited to the Paris conditions.

Another way to increase the precision of the measurements is to increase the signal that reaches the detector. This is discussed in section V.4.2.

V.4 Updated solar tracker

In January 2018 the solar tracker was sent to Bruker for an update. The updated solar tracker has returned to our site in May 2018. The update includes a new electronics, a camera based optical feedback control (see section II.2.2) and new solar tracker mirrors. In this section we discuss the improvements caused by this update: pointing errors and X_{CO_2} precision, and the appearance of a new phase correction problem.

V.4.1 Solar gas stretch as an indicator of pointing errors

GGG accounts for Doppler shift caused by the motion of the observer relative to the Sun due to the ellipticity of the Earth's orbit around the Sun and the Earth's rotation. But there is an additional source of Doppler shift caused by the pointing error introducing an additional velocity component due to the sun's rotation.

The solar tracker reflects the solar light into the spectrometer, where only a part of the solar image passes through the aperture hole to the interferometer (see Fig.II.9(a,b)). In the case of an ideal solar tracker, only the central part of the solar image would be used. If the solar tracker does not work properly, then the lateral parts of the solar image are measured. The lateral parts of the solar image are affected by the Doppler shift due to the spinning of the Sun. The solar rotation speed (v) is 1900 m/s which is 6.3×10^{-6} of the speed of light (c) and the maximum Doppler shift (Δf) is equal to $\frac{v}{c} f_0$, where f_0 is the emitted frequency. GFIT calculates the solar-gas (S-G) stretch from the spectral fit, representing the difference between the shifts of the atmospheric lines and the solar lines estimated from the spectral

fits. It is reported in dimensionless units (ppm): the wavenumber shift is divided by the local wavenumber. The S-G shift of 1 ppm corresponds to 300 m/s (i.e. one-millionth of the speed of light). Since the Sun rotates with an equatorial velocity of 1900 m/s, it is possible to get S-G shifts of up to 6 ppm in extreme cases, when the edge of the solar disk is used.

The top panel of the Fig.V.10 shows the time series of S-G shifts calculated for the O_2 microwindow since September 2014. The bottom panel shows the statistics (number of spectra against O_2 S-G values). The black colour is the data obtained with the old solar tracker system which uses a four quadrant photodiode, the red colour is the updated solar tracker with the Camtracker system (see section II.2.2). The updated system has a more condensed distribution of O_2 S-G varying between -0.25 and 0.5 ppm, while the old system has more dispersed values of O_2 S-G between -0.8 and 1.5 ppm, except the year 2016 where O_2 S-G values are not inferior to the new system. This demonstrates the better performance of the Camtracker system as compared to the old four quadrant photodiode system.

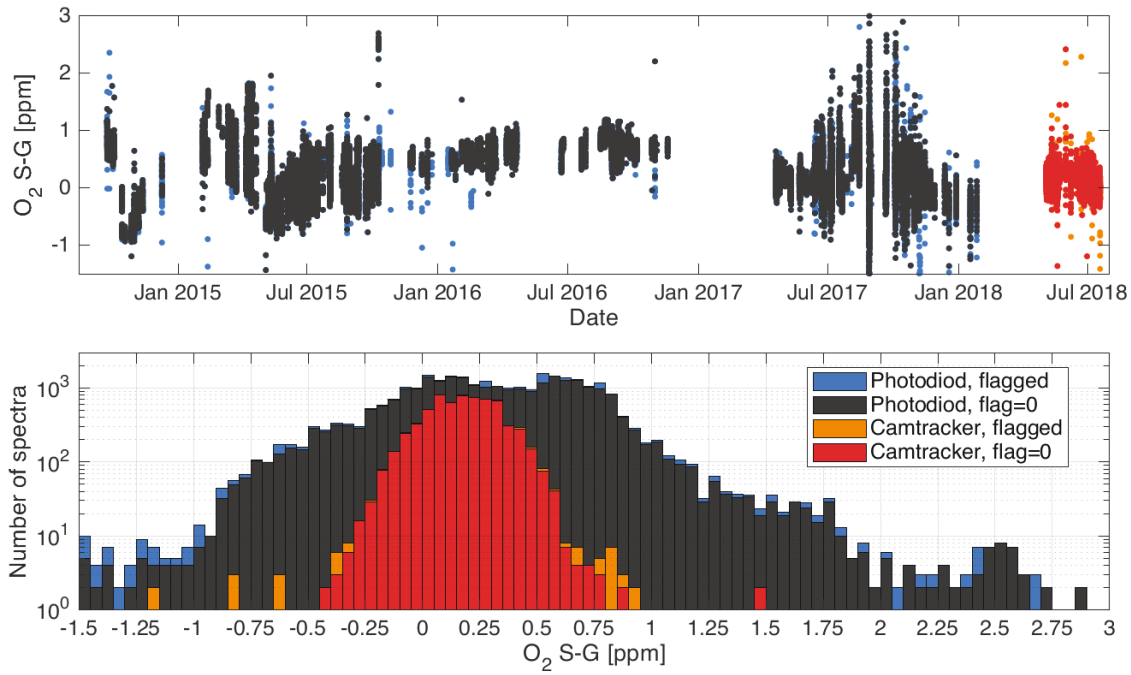

Figure V.10 – The comparison of O_2 S-G as the indicator of pointing errors for two solar tracker systems.

V.4.2 Improvements in $X_{CO_2}^{error}$ with an updated solar tracker

While the FTS is protected from the environmental conditions, the solar tracker is mounted on the roof terrace and is only protected from direct precipitation and dust by a dome. The solar tracker optical mirrors are made from a glass substrate that provides the optically flat surface, and on top of the substrate, a protected aluminium coating is applied that provides the required high reflectance. The reflectivity of the Solar Tracker mirrors decreases with time, especially in the visible range. This is caused by the deposition of dust and dirt, corrosion (deposition of reactive substances like salt or reactive gases in polluted air), and

scratches (mechanical abrasion from blowing sand or dust) [51].

The main effect of the new mirrors is a higher signal, i.e. signal to noise ratio, which leads to better precision measurements. The time series of $X^{error}_{CO_2}$ is presented in Fig.V.11 (top panel). It is important to note that the FTS-Paris uses a metallic mesh filter in order to

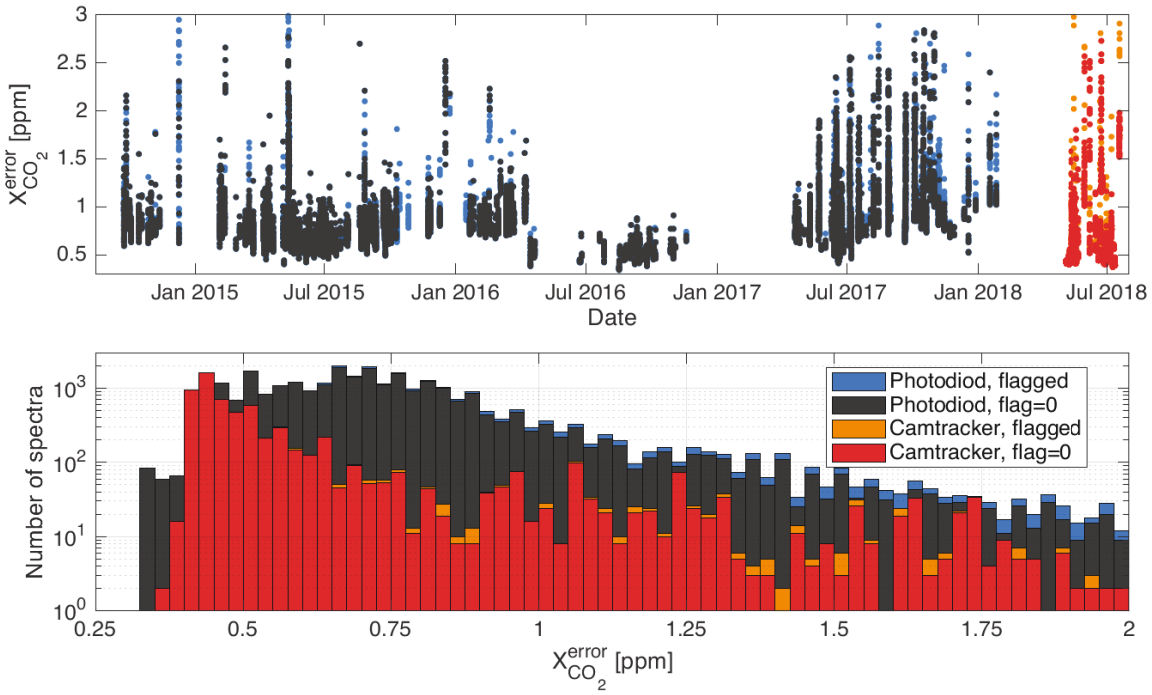

Figure V.11 – The top panel shows the time series of $X^{error}_{CO_2}$ calculated with an updated solar tracker (red colour) and the old system (black colour). The bottom panels shows the distribution of $X^{error}_{CO_2}$ for the two cases.

attenuate the signal and to avoid not only the saturation of the InGaAs detector but also its non-linearity when the signal is too high. We notice that $X^{error}_{CO_2}$ has the seasonal cycle, which increases during winter and has its minimums during summer. By January 2018, $X^{error}_{CO_2}$ has reached the value of 1 ppm, which is an unacceptably high value. After the update, the signal to noise ratio has increased by a factor of two and the $X^{error}_{CO_2}$ has achieved a good level: a median value of $X^{error}_{CO_2}$ is 0.48 ppm in 2018, and 0.69 ppm for the same time period in 2017. Fig.V.11 shows the histogram of $X^{error}_{CO_2}$ calculated with the updated solar tracker (from May 4, 2018 to July 18, 2018) and with the old solar tracker system (from September 23, 2014 to January 18, 2018). In order to be sure that the number of scans (F2B2) is still optimal , we have repeated a test of acquisition setup.

V.4.3 Comparison of acquisition setups with the updated solar tracker

The test of acquisition setups with the updated solar tracker was performed on two days: July 23 and July 24, 2018. We have tested three setups using a scanner velocity of 40 kHz: F1B1, F2B2 and F4B4, and one setup with the scanner velocity set to 20 kHz: F1B1. The aim of this test is to check if the scanner velocity of 20 kHz could be used and to compare F1B1, F2B2 and F4B4 setups. X_{CO_2} and $X^{error}_{CO_2}$ for each of acquisition setups is presented in Fig.V.12.

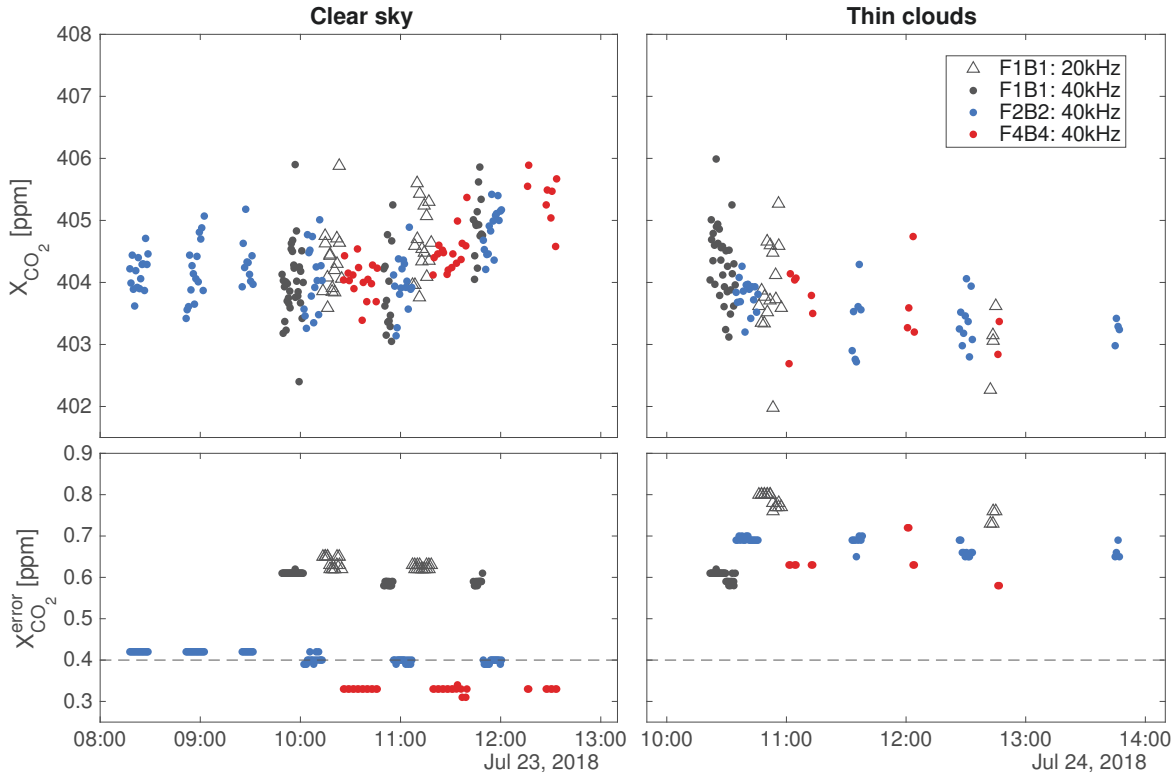

Figure V.12 – Number of scans test with the new solar tracker system.

July 23 was a day with clear sky and July 24 was a day with very thin clouds, typical for Paris. The comparison of $X^{error}_{CO_2}$ for each setup on both days is presented in table V.3. On both days F4B4 has better $X^{error}_{CO_2}$ than F2B2, but the number of spectra on June 24 that have passed through the quality control filter is significantly lower with F4B4 than with F2B2 (12 spectra for F4B4 and 37 spectra for F2B2). F1B1 at 20 kHz leads to the worst results, even F1B1 at 40 kHz has better $X^{error}_{CO_2}$.

Thus, the optimal acquisition setup depends on the sky conditions. If the sky is clear then F4B4 would be the best option providing a sufficient number of spectra and the best $X^{error}_{CO_2}$. Nevertheless, we have kept the F2B2 setup which is the best compromise.

V.5 The phase correction problem

The recorded interferograms are converted into the spectra by applying a Fourier transformation. The recorded interferograms are sampled by a limited number of points. If the

Table V.3 – $X^{error}_{CO_2}$ for different acquisition setups obtained on two test days in July 2018.

Setup	$X^{error}_{CO_2}$, ppm July 23	July 24
F1B1: 20 kHz	0.62	0.80
F1B1: 40 kHz	0.61	0.61
F2B2: 40 kHz	0.42	0.69
F4B4: 40 kHz	0.33	0.63

interferogram is not symmetrically sampled near ZPD (number of points on both sides of ZPD is not equal), a phase correction procedure should be applied (described in section II.1.5). A phase angle is a slowly varying function with wavenumber, which is calculated from a short part of the recorded interferogram. The phase curve is derived by I2S using a fractional intensity threshold parameter (denoted PC) for use of a spectral point in deriving the phase curve. For example, a value of PC=0.02 means that only the low-resolution points exceeding 2% of the peak spectral magnitude are used to define the phase curve. The other weaker points (below threshold) are ignored and the phase at these frequencies is

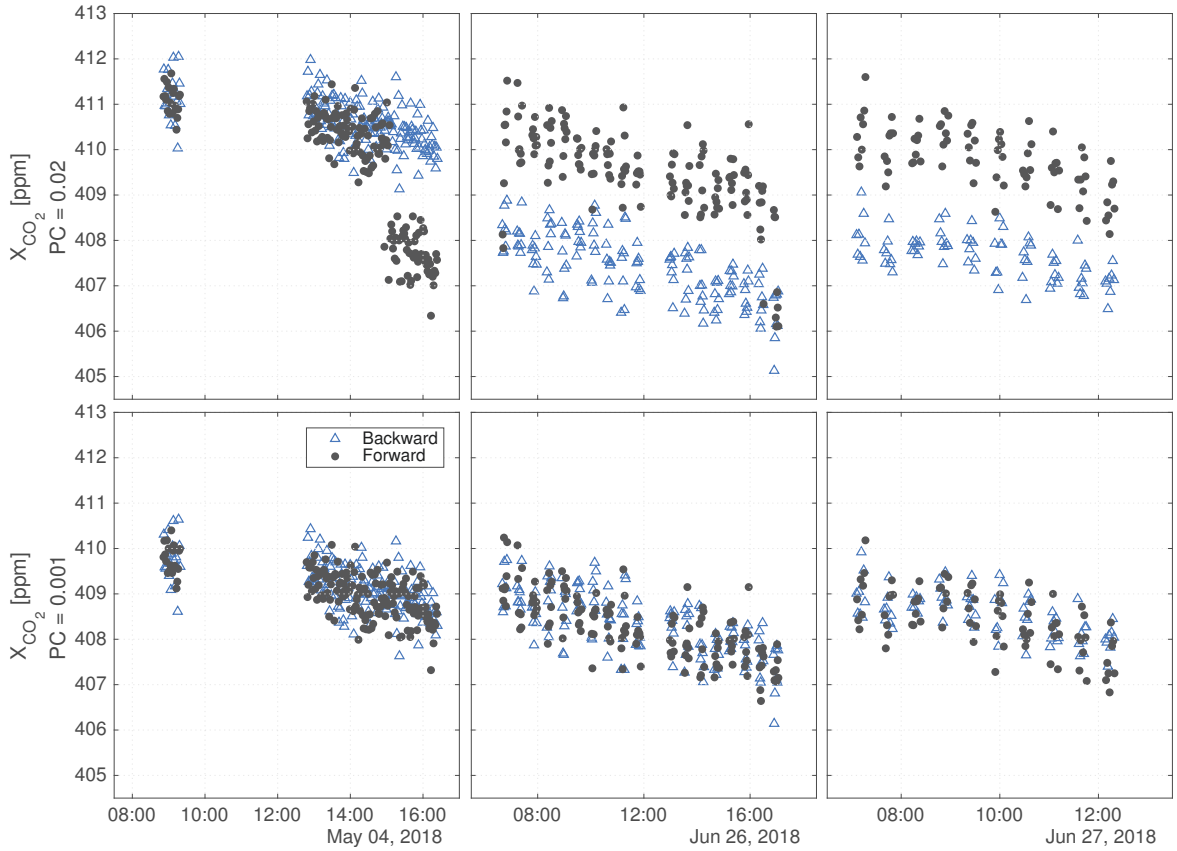

Figure V.13 – An example of phase correction problem obtained for X_{CO_2}. Forward and backward values are not consistent for PC=0.02. Top panels are values with PC=0.02; bottom panels are values with PC=0.001.

interpolated.

The PC value recommended by TCCON is 0.02. Since May 2018, we observe an artefact in retrieved gas columns for forward and backward spectra when the PC=0.02 is used (see Fig.V.13, top panels). X_{CO_2} retrieved for forward and backward spectra is not consistent and biased by ∼2.2 ppm. This problem disappears when we use PC=0.001 (see Fig.V.13, bottom panels). $X_{CO_2}^{PC=0.001}$ is consistent between forward and backward scans but it is biased when compared to $X_{CO_2}^{PC=0.02}$. It is clearly seen on May 4, $X_{CO_2}^{PC=0.02}$ between 08:00 and 14:30 is consistent, $X_{CO_2}^{PC=0.001}$ over the same time interval is biased by -1.25 ppm. On June 26 and 27, $X_{CO_2}^{PC=0.001}$ is located between forward and backward $X_{CO_2}^{PC=0.02}$.

In order to understand the cause of this artefact, we plotted phase curves for each of the cases, Fig.V.14. A complex low resolution spectrum calculated from the interferogram is denoted S_{LR}. Amplitudes (black curves on top panels) are the same for both PC, because they are calculated as $\sqrt{\mathrm{Re}(S_{LR})^2 + \mathrm{Im}(S_{LR})^2}$, but the phase curves differ since the threshold is applied. The difference in phase curves is observed for the regions where S_{LR} contains only noise: below 4000 cm^{-1}; 5150-5500 cm^{-1}; 7000-7400 cm^{-1} and above 11500 cm^{-1}. In the forward high resolution spectrum (left bottom panel), this leads to the small difference in noise regions and there is a difference in continuum levels which could lead to the differences

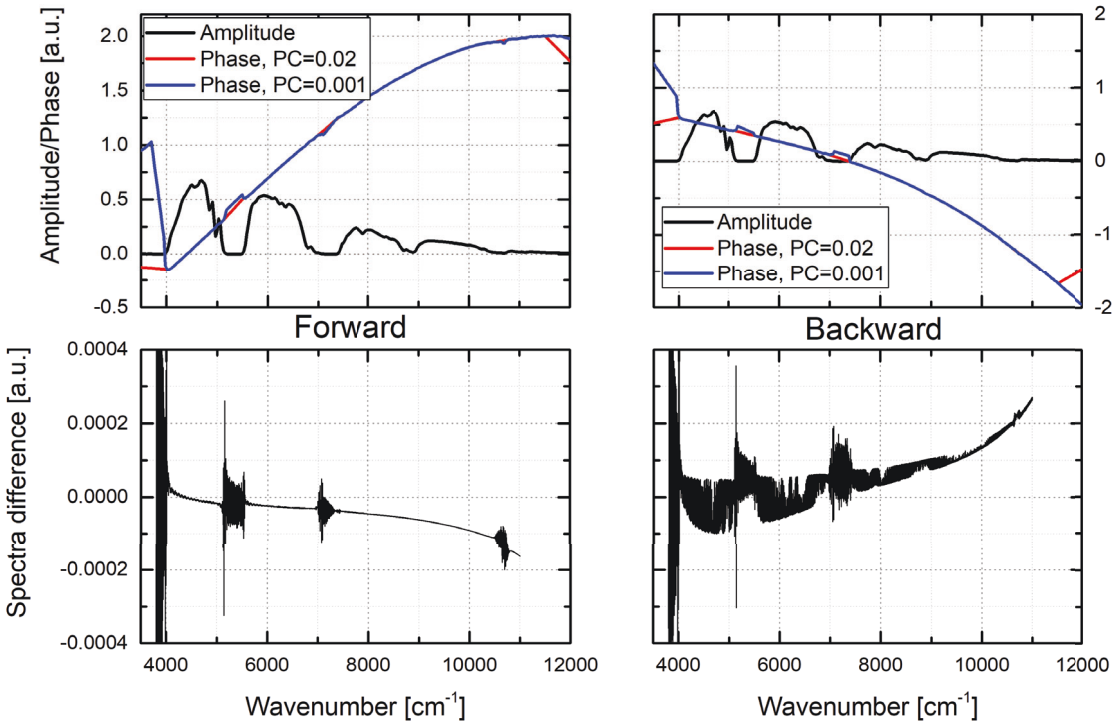

Figure V.14 – Example of phase curves and spectra residuals for forward (left panels) and backward (right panels) spectra. Two top panels: low resolution amplitudes (black curves), red curves are phase curves calculated with PC=0.02 and blue curves with PC=0.001. The bottom panels show the residual between the real high resolution spectra calculated with PC=0.02 and PC=0.001.

in retrieved gas columns. For the backward high resolution spectrum (bottom right panel) the situation is more complex, in addition to the continuum level, absorption lines are present. These absorption lines have an amplitude of 0.1-0.2% of the spectrum which is few times lower than the noise level (0.4%). Continuum level (mainly) and the difference in absorption lines lead to the difference in gas columns. The difference in continuum levels increases with the wavenumber, which would have bigger impact on high wavelength molecules (O_2 at 7885 cm^{-1}).

The comparison of CO_2 and O_2 columns on May 4 is presented in Fig.V.15. Discrepancies between problematic forward and backward spectra for CO_2 columns is +0.2% and +0.85% for O_2. For spectra calculated with PC=0.001 we do not observe these discrepancies, but columns are biased by +0.17% for CO_2 and +0.48% for O_2 in compare to PC=0.02 spectra, that are not affected by forward-backward problem.

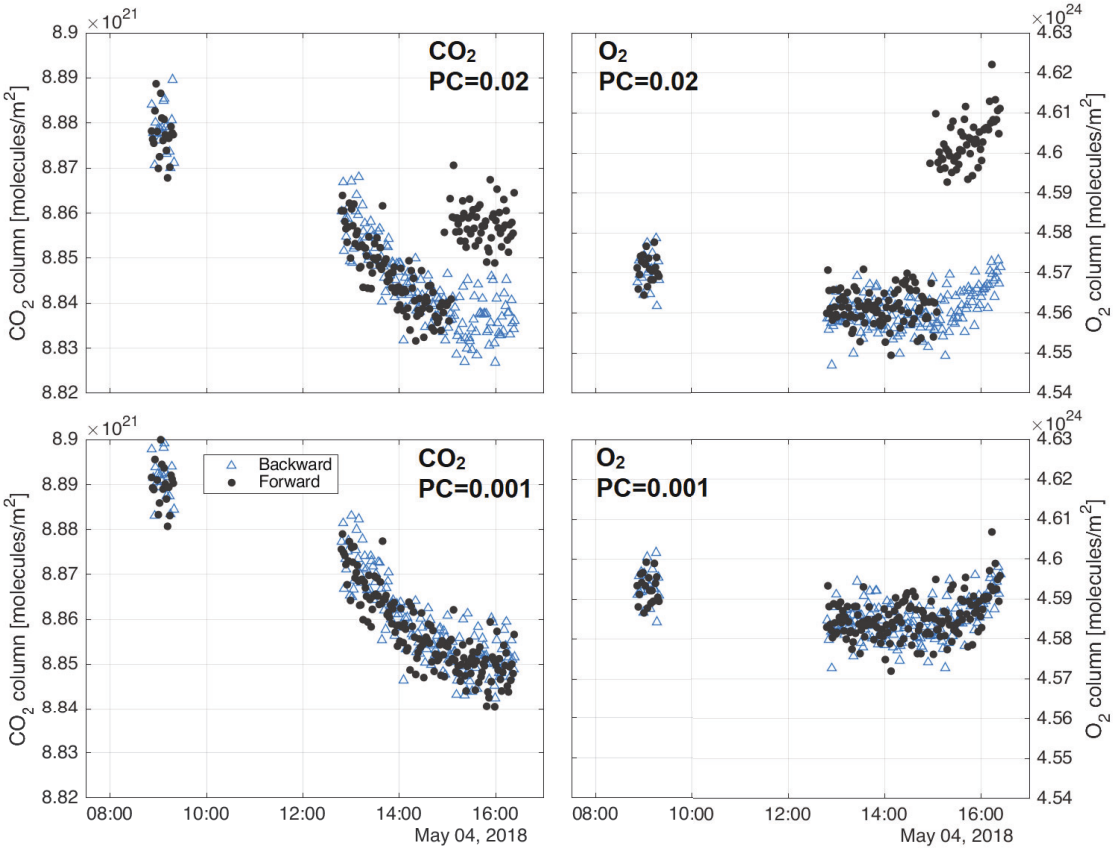

Figure V.15 – The comparison of CO_2 and O_2 columns on May 4 for two phase correction parameters.

Despite on the phase correction problem, $X_{CO_2}^{PC=0.001}$ could not be used as an official TCCON product, because it is biased as compared to $X_{CO_2}^{PC=0.02}$. We have recalculated one year of X_{CO_2} with PC=0.001 and compared it with PC=0.02 (Fig.V.16). The bias between

the two datasets is not constant and can vary during one day of measurements from 1.5 ppm to 3.25 ppm. The correlation between the two datasets is shown in Fig.V.17. The fitted line (the red curve) that passes through the origin, has a slope of 0.996. Thus the average bias between the two datasets is 0.4% (∼1.6 ppm). If we assume that $X_{CO_2}^{PC=0.02}$ is calibrated onto the WMO scale, then to get $X_{CO_2}^{PC=0.001}$ also calibrated it should be corrected for this bias, i.e. +0.4% which equivalent to the multiplication by a factor of 1.04. Anyway, the phase correction problem will be solved with the next update of GGG, since the problem has been also identified by other TCCON sites and a new reanalysis will be conducted for all TCCON data.

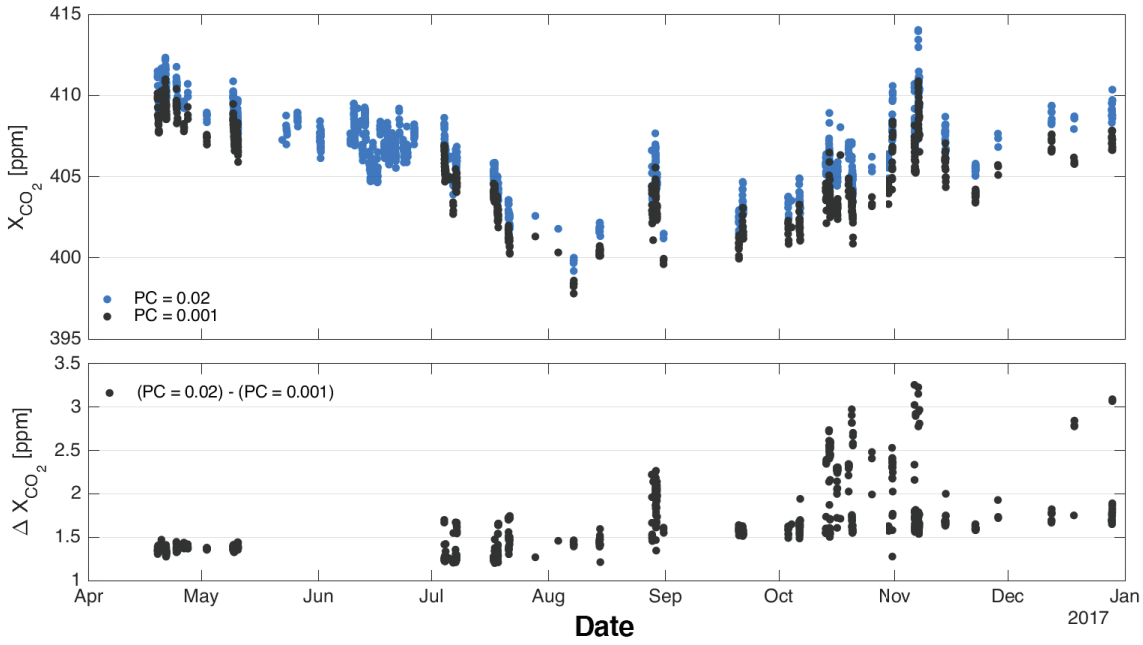

Figure V.16 – The top panel shows time series of $X_{CO_2}^{PC=0.02}$ and $X_{CO_2}^{PC=0.001}$ calculated for 2017. The bottom panel shows the difference between two datasets, i.e. $X_{CO_2}^{PC=0.02} - X_{CO_2}^{PC=0.001}$.

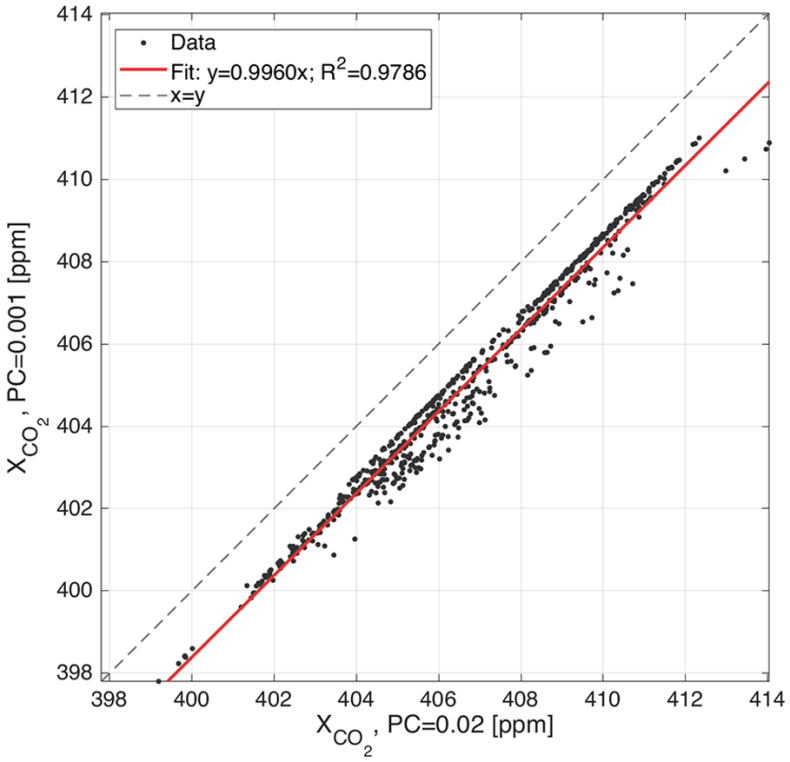

Figure V.17 – The correlation plot of $X_{CO_2}^{PC=0.02}$ and $X_{CO_2}^{PC=0.001}$. The linear fit (the red curve) is made through the origin.

VI – X_{CO_2} retrieved with modified CO_2 a priori profiles

In this chapter we investigate the accuracy of the TCCON-Paris measurements in the condition of the polluted boundary layer in Paris. The key idea of this study is to use in situ CO_2 and planetary boundary height measurements to modify CO_2 a priori volume mixing ratio profiles in the retrievals of X_{CO_2}.

Section VI.1 discusses in situ CO_2 and planetary boundary layer height measurements in Paris at the QualAir platform. Section VI.2 explains the problem of the standard set of CO_2 a priori profiles for the Paris case and proposes a method to solve this problem. In Section VI.3 we show the performance of the proposed method by studying two cases: one day when the boundary layer is highly polluted and another day with the typical conditional of the boundary layer in Paris. In Section VI.4 we apply our method to the three years of measurements by using one modified CO_2 a priori profile per day. In Section VI.5 we use four modified CO_2 a priori profiles per day for the study of summer 2017. In Section VI.6 we discuss how this could affect validation of satellite missions, using the example of OCO-2.

In the following, the term dry air mole fraction is simplified by concentration and is expressed in the part per million (ppm) unit.

VI.1 Paris conditions

Megacities are agglomerations with a population exceeding 10 million. Consequently, large quantities of CO_2 due to the human activities are released in these places. Based on the 2010 population census, the Paris metropolitan area has 10.5 million inhabitants and is ranked as the 21st largest megacity in the world and second in Europe after Moscow.

Paris is centered in the Île-de-France (IdF) region that contains 18% of the French population [52] while covering only 2% of the territory. The emission inventory reported by Association de surveillance de la qualité de l'air en IDF (AIRPARIF) estimates that IdF emitted a total of 41.9 Mt of CO_2 in 2010, i.e., 12% of French anthropogenic CO_2 emissions (CITEPA, 2017, URL: https://www.citepa.org/fr/air-et-climat/polluants/effet-de-serre/dioxyde-de-carbone). Advection and vertical mixing strongly influence the urban CO_2 signal. At low wind speeds, urban CO_2 emissions accumulate over the city and generate an urban dome of CO_2 which adds several tens of ppm at night and several ppm in the afternoon to the background level of surrounding rural areas [53]. At higher wind speeds, the CO_2 urban dome decreases through ventilation processes. The TCCON-Paris station is installed on the QualAir platform at the Jussieu campus of Sorbonne Université. The

QualAir platform is operated by two laboratories: Laboratoire d'Etudes du Rayonnement et de la Matière en Astrophysique et Atmosphères (LERMA), Laboratoire Atmosphères, Milieux, Observations Spatiales (LATMOS) and Laboratoire des Sciences du Climat et de l'Environnement (LSCE). The results of Planetary Boundary Layer height measurements by LATMOS and CO_2 in situ measurements by LSCE are presented in the next two sections.

VI.1.1 Planetary Boundary Layer height measurements

The Paris Planetary Boundary Layer height (PBLh) is determined by LIDAR measurements (LIDAR is the acronym for LIght Detection And Ranging). LIDAR is an active remote sensing technique. It relies on the scattering of laser light pulses by atmospheric aerosols. The optical power of the backscattered light is detected as a function of time, which yields the altitude information, and it is proportional to the aerosol content of the atmosphere. Because the mixed boundary layer is typically moister and has a greater aerosol content than the free troposphere, LIDAR can detect the boundary between the two layers and its altitude. The PBLh over Paris was measured by the Qualair 532 nm elastic aerosol LIDAR which uses gradient detection method [Menut et al. [1999]]. The PBLh data used in this thesis has been provided by Prof. François Ravetta (LATMOS/IPSL, Sorbonne Université, UVSQ, CNRS, Paris, France). Due to the lack of LIDAR data in coincidence with TCCON

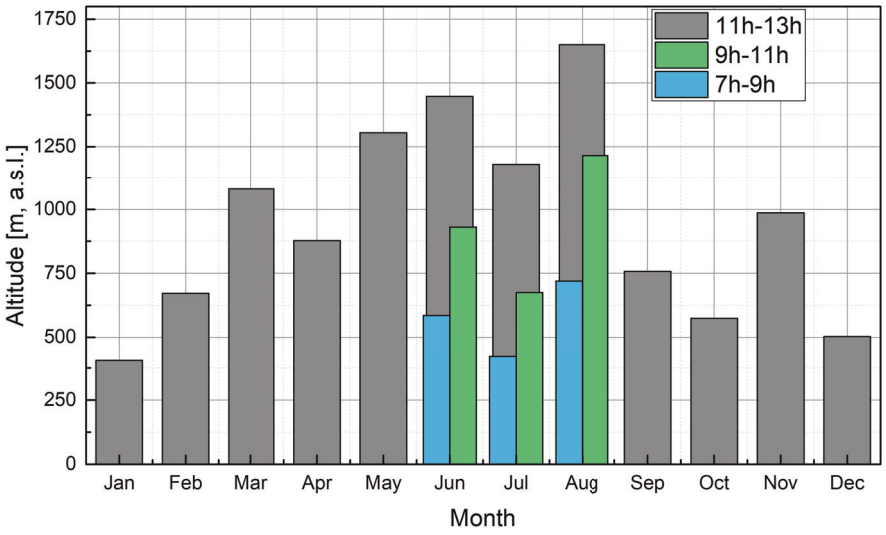

Figure VI.1 – The statistical model of the PBLh based on four years of measurements. Grey columns are noon values (average between 11:00 and 13:00 UTC) representing a developed PBL; blue and green are morning values (average between 7:00 and 9:00 and between 9:00 and 11:00 respectively) representing the PBL development in summer.

measurements and an instrumental failure during the Summer 2017, we will mainly use a statistical model based on four years (2011-2014) of PBLh measurements over Paris [54]. In Fig.VI.1 the statistical model of the PBLh is presented as a function of month. Grey columns represent the statistical data collected around noon between 11:00 and 13:00 representing an already developed PBL. Blue and green columns are the statistical data collected between 7:00 and 9:00 and between 9:00 and 11:00 respectively, representing the development of the

PBL during summer.

VI.1.2 CO_2 in situ dataset measured at Jussieu

The CO_2 in situ dataset was obtained using the cavity ring-down spectroscopy (CRDS) technique. In CRDS, the beam from a single-frequency laser diode enters into a cavity defined by two or more high reflectivity mirrors. When the laser is on, the cavity quickly fills with the laser light. A photodetector measures the amount of light leaking through one of the mirrors. The signal from photodetector is directly proportional to the intensity in the cavity [55]. When the signal reaches a threshold level, the laser is turned off and the light residing within the cavity bounces between the mirrors and leaks out steadily, leading to an exponential decay. For an empty cavity, the decay time is determined by the distance between mirrors and their reflectivity. If the cavity is filled with a target gas that absorbs the laser light, then the decay time is shortened due to molecular absorption. By measuring the decay time at different wavelengths, an absorption spectrum of the trace gas is obtained. This allow to determine the target gas concentrations.

The CRDS measurements are made with the use of a Picarro instrument, model G1302. The atmospheric air is collected at the roof terrace at few meters distance from TCCON-Paris solar tracker and is pumped through an inlet line into the analyzer. The analyzer performs measurements at a rate of 0.5Hz, a temperature of 45°C and a pressure of 140 Torr. The CRDS CO_2 measurements are calibrated by using reference gas tanks.

Fig.VI.2 shows the CO_2 in situ dataset collected from November 7, 2014 to March 5, 2018. Grey points represent one hour averages which can reach up to 600 ppm at particular days (figure scale is fixed to 500 ppm in order to clearly see the seasonal variation). Black points are the means between 11:00 and 13:00 UTC (noon data, there are 9 days out of 831

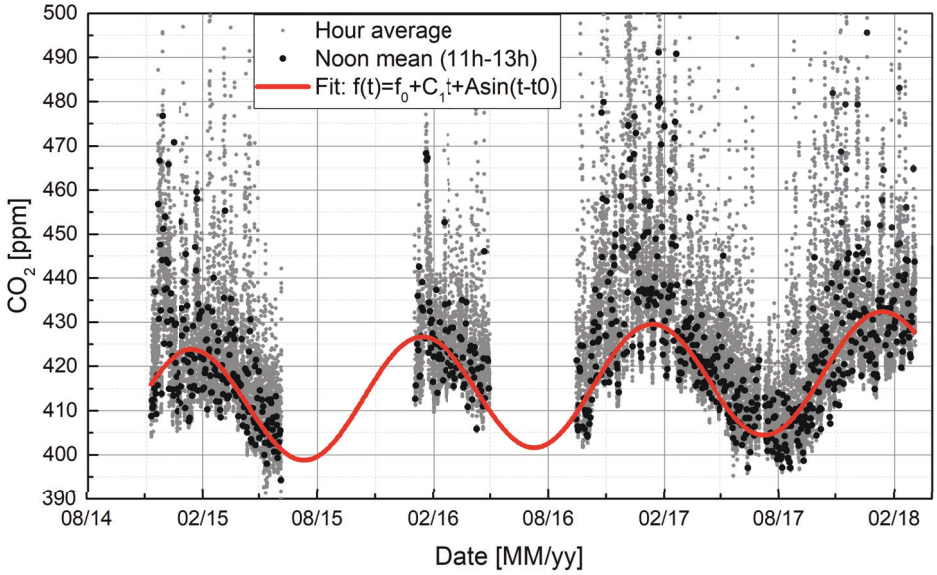

Figure VI.2 – In situ CO_2 VMRs measured at Jussieu. Grey points represent one hour averages and black points are means around noon (from 11h00 to 13h00 UTC). The red line is a sine-shape fit to the black points.

with noon average above 500 ppm). The data record shows two large gaps from June 6, 2015 to January 1, 2016 and from April 30, 2016 to September 14, 2016, caused by an instrumental problem. The red line in Fig.VI.2 is a sinusoidal fit to the black points in order to fill the data gaps. The fitted line has an amplitude of 13 ppm and shows an annual increase of 3.5 ppm. The CO_2 in situ data has been provided by Dr. Irène Remy-Xueref (OSU Pytheas, Station Maritime d'Endoume, 13007 Marseille, France).

VI.2 The problem of TCCON retrievals at Paris

The TCCON spectral fitting program GFIT (previously described in section IV.3.2) applies a vertical scaling factor (VSF) to the a priori volume mixing ratio (VMR) gas profiles (priors for short). The underlying assumption is that the shape of the vertical gas profiles is known. This reduces the calculation time as compared to full vertical profile retrievals. VSFs are calculated and multiplied by the a priori vertical column abundances to yield retrieved column values (Section IV.3.4, Eq.(IV.4)). As explained previously in section IV.3.3, CO_2 priors used by GFIT are based on an empirical model. Fig.VI.3 shows an example of different CO_2 priors for the TCCON-Paris site, generated by GGG. The CO_2 priors have a minimum VMR at the ground of 374 ppm during summer 2017, whereas the CO_2 in situ measurements (noon average) have a minimum value of 396 ppm and a summer mean value of 409 ppm.

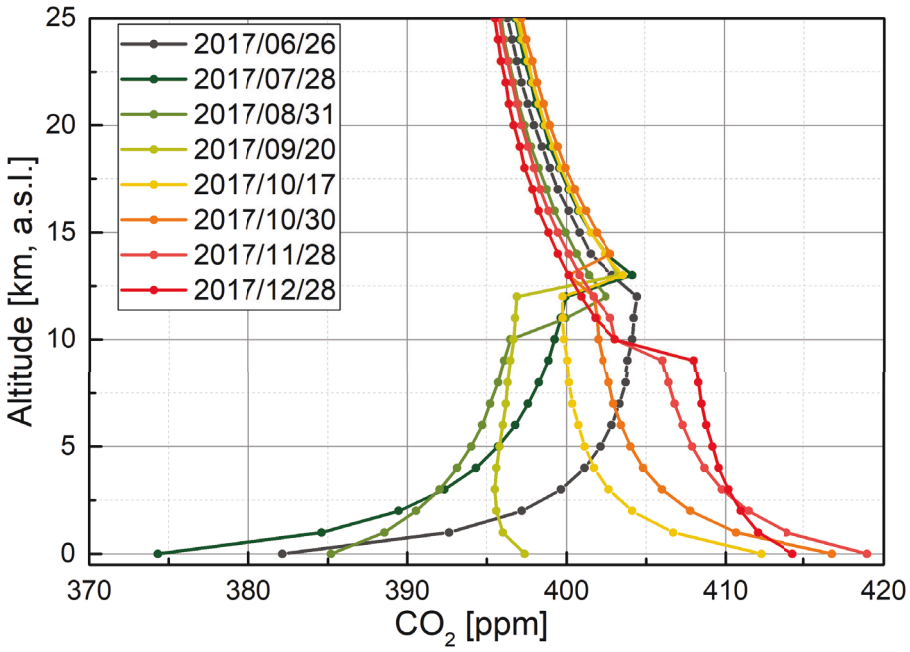

Figure VI.3 – CO_2 priors at the TCCON-Paris site for some selected days in 2017.

If the CO_2 prior is close to the real atmospheric CO_2 VMR profile, the calculated VSF_{CO_2} is expected to be close to unity. The lack of CO_2 molecules at the bottom part of CO_2 priors leads to increased VSF_{CO_2} values during summer 2015, 2016 and 2017 (Fig.VI.4). GFIT compensates the lack of CO_2 in the lower troposphere (inside the PBL) by overscaling priors with VSF_{CO_2} values up to 1.02, which corresponds to the shift of priors by 8 ppm. The

VSF_{CO_2} during winter has values less than unity, despite the polluted PBL in Paris. It is probably caused by an overestimation of CO_2 VMRs in the free troposphere of a priori profiles.

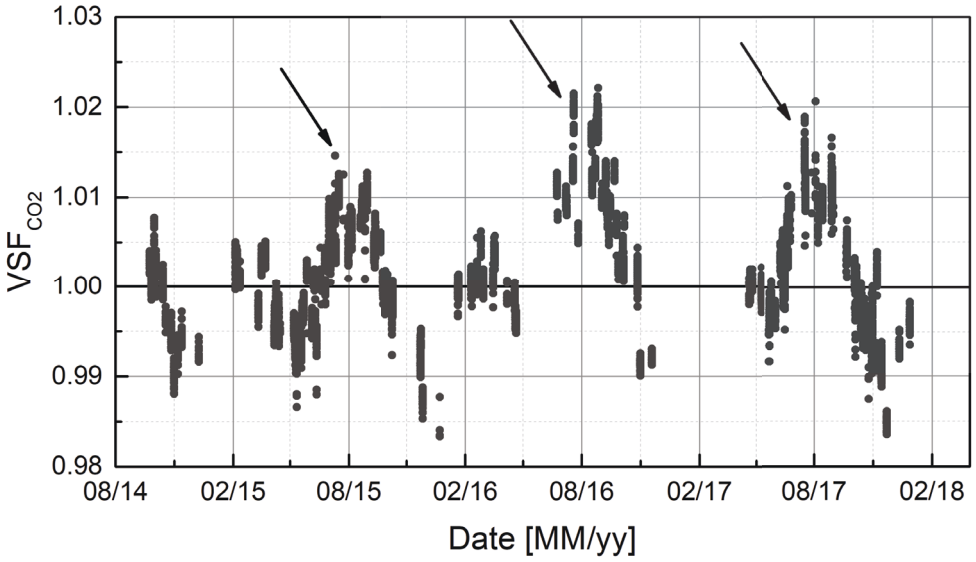

Figure VI.4 – Time series of CO_2 vertical scale factors calculated by GFIT for TCCON-Paris. Black arrows indicate the systematic increase of VSFs during summer periods.

The difference between the CO_2 a priori profiles generated by GGG and the real CO_2 profiles affected by Paris conditions could lead to biases in the retrieved column averaged DMFs of CO_2 (X_{CO_2}).

In the following sections, we estimate the bias by using different sets of modified CO_2 priors. The idea is to take the standard CO_2 a priori profile generated by GGG and to modify its bottom part, see Fig.VI.5, and feed the modified profile into GFIT. The bottom part of the modified priors represents a polluted boundary layer. We consider a simplified case, assuming that the PBL is well mixed and that the CO_2 mixing ratio does not change with altitude inside of the PBL. The in situ data is used to fix the CO_2 VMR inside the PBL. Above the PBL, the prior remains unaltered as compare to the standard prior.

Altitude grid

The standard CO_2 priors created by GGG2014 are given on an altitude grid from 0 to 70 km with a step size of 1 km. For the purpose of this work (modification of CO_2 priors at the altitude of PBLh) we have redefined the altitude grid by using an altitude step of 500 m at altitudes below 3 km. The new altitude grid therefore is 0, 0.5, 1, 1.5, 2, 2.5, 3, 4, 5,...70 km. The usage of an even smaller altitude step is impractical, because the vertical resolution of the FTIR is not sufficient. The step size of 500 m was defined empirically after comparing different altitude steps (50 m, 100 m and 250 m). It has been found that the step size of 500 m produces the best fit results.

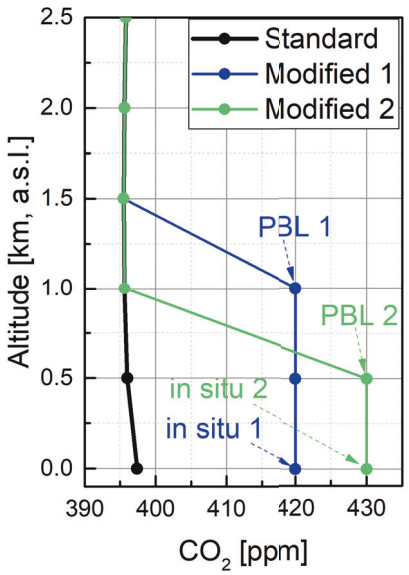

Figure VI.5 – Three examples of CO_2 a priori profiles: Standard profile generated by GGG (black line) and two modified profiles (blue and green curves).

Residual comparison

In order to judge whether the modified CO_2 priors are better suited than the standard priors for describing Paris conditions, we compare the residuals of the fit for the two CO_2 microwindows used by GFIT. We compare the RMS (root mean square) of the fit residuals (measured minus calculated spectra) calculated with the use of standard and modified CO_2 a priori profiles (next for simplification the "RMS of the residual" is denoted "RMS"). The RMS calculated with the use of the standard a priori profiles are denoted $RMS^{6220}_{\text{standard}}$ and $RMS^{6339}_{\text{standard}}$ for each CO_2 microwindows correspondingly and $RMS^{6220}_{\text{modified}}$ and $RMS^{6339}_{\text{modified}}$ with the use of the modified a priori profiles. We are interested in the value ΔRMS defined by:

$$\Delta RMS = \frac{1}{2}\left(\frac{RMS^{6220}_{\text{modified}} - RMS^{6220}_{\text{standard}}}{RMS^{6220}_{\text{standard}}} + \frac{RMS^{6339}_{\text{modified}} - RMS^{6339}_{\text{standard}}}{RMS^{6339}_{\text{standard}}}\right) \cdot 100\% \quad \text{(VI.1)}$$

A negative value of ΔRMS means that a better fit is obtained when the modified prior is used and a positive value means that the fit is better when it is performed with the standard prior.

VI.3 X_{CO_2} sensitivity study

In this section we investigate how the modified CO_2 priors influence X_{CO_2}. This is done for two case studies: one for a highly polluted PBL (January 20, 2016) and one for unpolluted PBL (April 18, 2016).

VI.3.1 Case study of a highly polluted day - January 20, 2016

Air mass conditions

According to AirParif (http://www.airparif.asso.fr/), January 20, 2016 was a polluted day in Paris. The CO_2 in situ VMR remained close to 460 ppm during all day (Fig.VI.6). The wind blows from the East (90-110°) with speeds between 3-7 km/h. Thus, it is too weak to blow off the city plume.

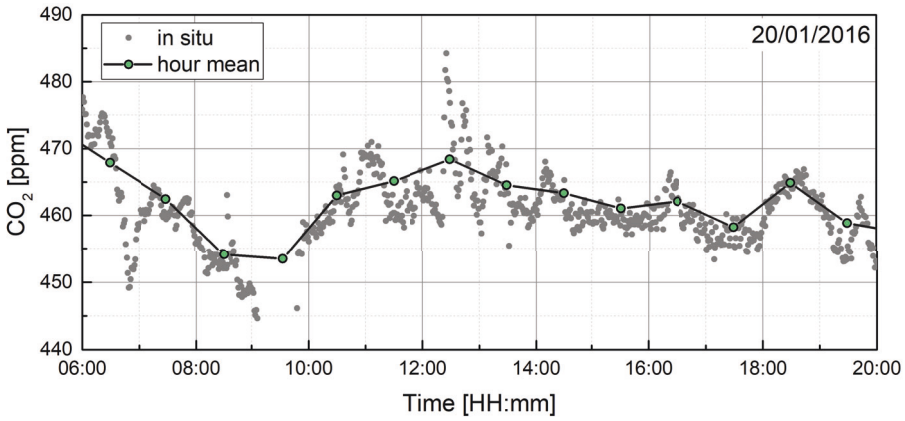

Figure VI.6 – Time series of CO_2 in situ measurements on January 20, 2016. The measurements are performed at the QualAir platform at Jussieu.

The PBLh measured by LIDAR at that day shows unusually low values. It is around 200 m between 11:00 and 15:00 UTC, while the average value for January is 400 m (see Fig. VI.1).

Set of modified CO_2 priors

The standard CO_2 prior for January 20, 2016 is shown in Fig.VI.7 (the top panel, black curve). The value of the CO_2 prior at the ground is 407 ppm, while the in situ CO_2 measurements are 50 ppm higher. We are looking for the modified prior that provides the best fit for all spectra on that day. To find it, we use a set of modified priors with 500 m altitude and different CO_2 VMRs inside the PBL from 400 to 500 ppm with a step of 10 ppm (green curves in top panel of Fig.VI.7). By the use of these modified priors we have calculated ΔRMS for each measured spectrum. The bottom panel of Fig.VI.7 shows the mean values of ΔRMS calculated by the use of modified CO_2 priors. A minimum of mean ΔRMS is about 460-470 ppm, GFIT is insensitive to CO_2 variatiosn less than 10 ppm for a given PBL height. For convenience, we assume that 460 ppm is the minimum (highlighted by red color in Figures).

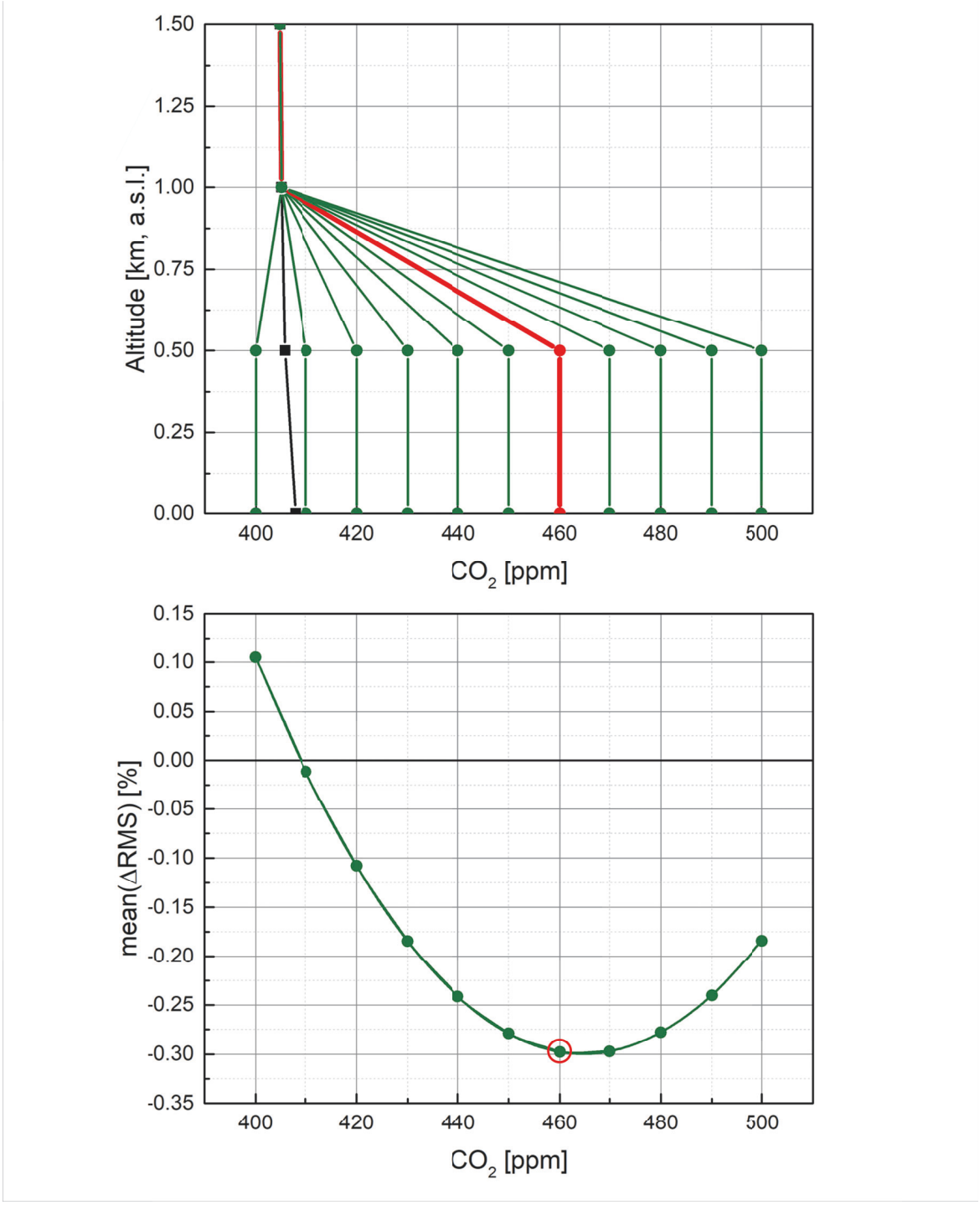

Figure VI.7 – The top panel is the set of modified CO_2 priors modified at the altitude of 500 m and the CO_2 concentration between 400 and 500 ppm. The bottom panel shows the mean values of ΔRMS calculated for each spectrum by using modified CO_2 priors from the plot above. The red color indicates the optimal modified formula prior.

We have repeated the same exercise for two other sets of modified a priori profiles: one with an altitude of 0 m (only the ground concentration is modified) and one with an altitude of 1000 m. The resulting curves of mean ΔRMS are presented in Fig.VI.8. The set with 0 m altitude has its minimum at 600 ppm (the corresponding modified a priori profile is denoted 0000_600, where the first number is the altitude of modification and the second is concentration), The value is far from the in situ CO_2 VMR, which is 140 ppm lower. For 1000 m altitude set the minimum is found at 440 ppm (denoted 1000_440). This value is lower than the measured CO_2. The 500 m altitude set has minimum of 460 ppm (denoted 0500_460) closest to the measured CO_2.

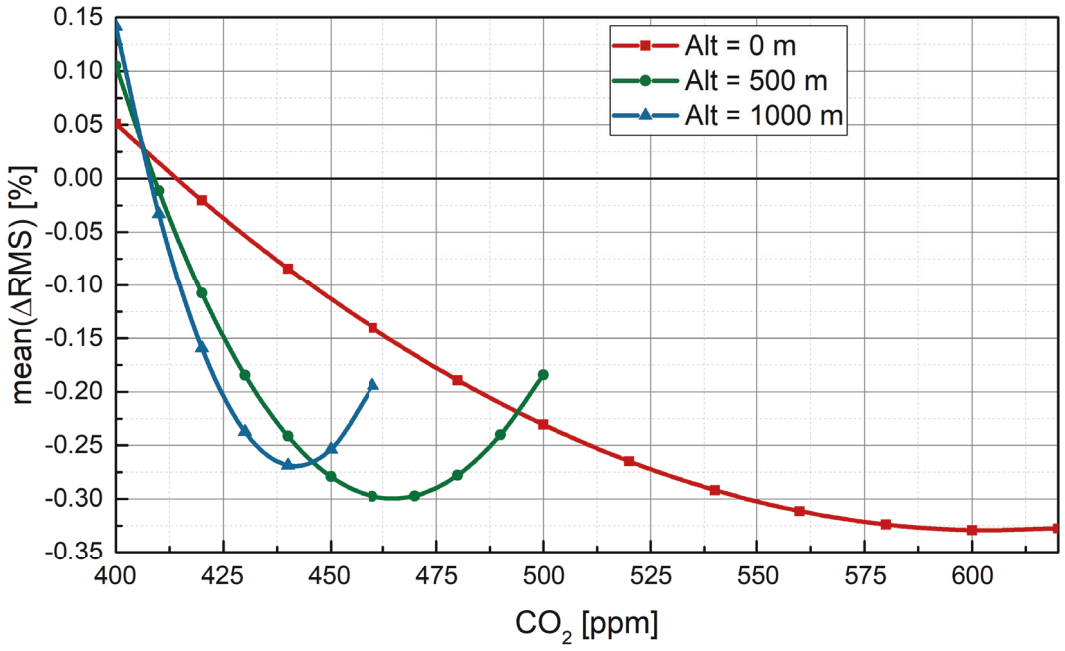

Figure VI.8 – Daily mean values of ΔRMSs obtained with three sets of modified CO_2 priors: 0, 500 and 1000 m.

For each of the best fitted modified CO_2 priors (0000_600, 0500_460 and 1000_440) X_{CO_2} has been calculated and shown in Fig.VI.9. The bias between standard and modified X_{CO_2} is shown in the bottom panel ($\Delta X_{CO_2} = X_{CO_2}^{\text{modified}} - X_{CO_2}^{\text{standard}}$). ΔX_{CO_2} does not differ much between three modified CO_2 priors, because FTIR measurements have not sufficient vertical resolution. This also explains the choice of the 500 m step as the altitude grid. It is therefore difficult to distinguish between two molecules that are at close altitudes, but FTIR measurements are sensitive to the number of molecules added to the layer. Let's estimate the number of molecules added by modifying CO_2 priors, relative to the standard CO_2 prior. As a rough estimate we compare the integrated surfaces under each CO_2 profile ($f(z)$):

$$\Delta\text{Surf} = \int_0^{z_{max}} f_{modified}(z)dz - \int_0^{z_{max}} f_{standard}(z)dz$$

where ΔSurf has the dimension of ppm×km and is called additional surface. For 0000_600 the additional surface is 45 ppm×km, for 0500_460 is 41 and for 0000_440 is 42. All three values are very close to each other, which confirms our hypothesis about the sensitivity to

the number of added molecules. For the noon time interval between 11:00 and 13:00 ΔX_{CO_2} stays close to -0.5 ppm. After 13:00 ΔX_{CO_2} decreases with the increase of solar zenith angle (SZA) and reaches -1.75 ppm. The anticorrelation of SZA and ΔX_{CO_2} can immediately be observed in Fig.VI.9. As we will see in a moment, the behaviour of ΔX_{CO_2} is caused by the difference in averaging kernels (AK) which strongly depend on SZA.

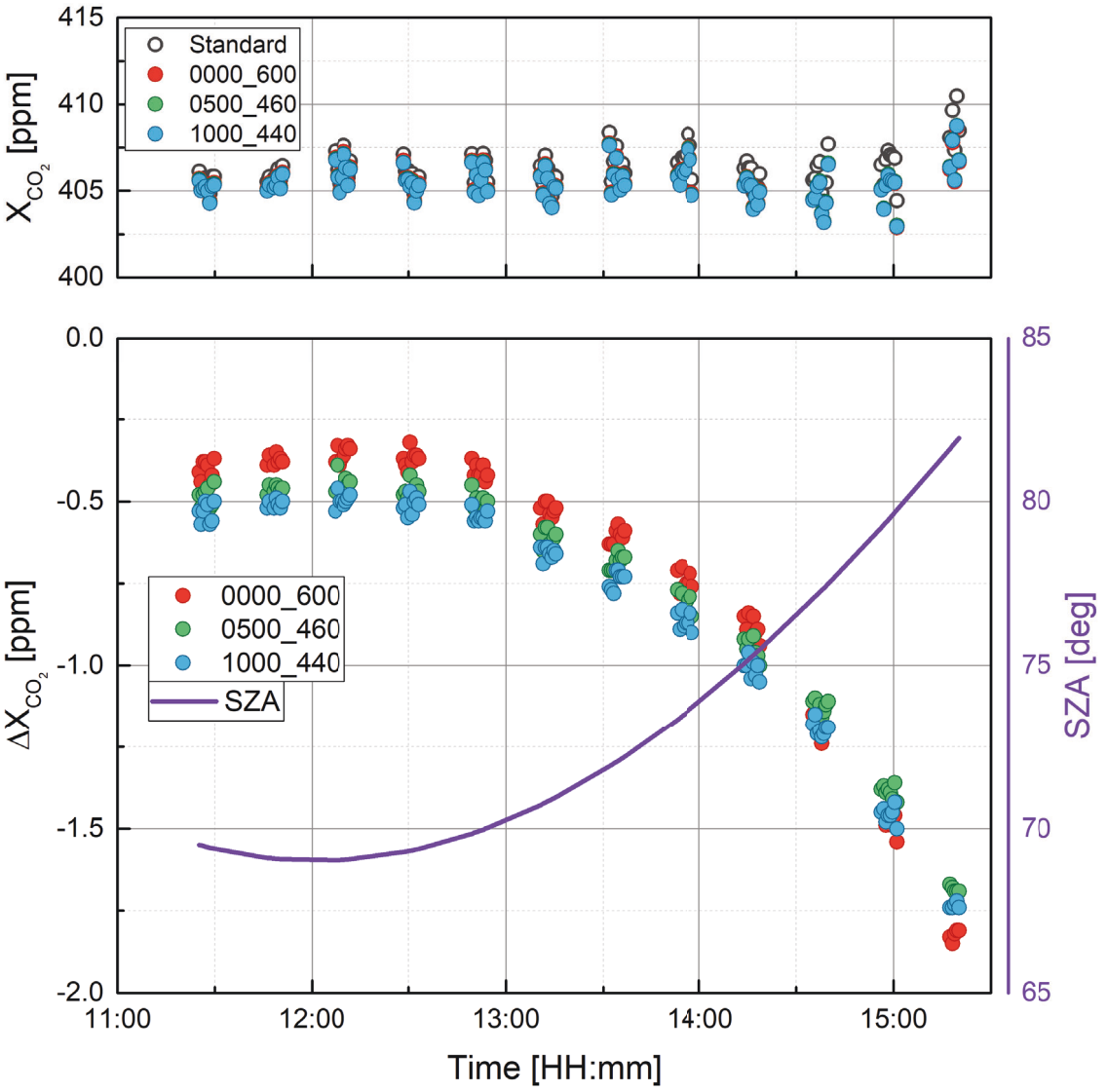

Figure VI.9 – The comparison of X_{CO_2} calculated with standard and modified CO_2 priors. The bottom panel shows ΔX_{CO_2} calculated by the use of three modified CO_2 priors (0000_600, 0500_460 and 1000_440), and SZA dependence (violet color).

In order to investigate the SZA dependence of ΔX_{CO_2} we have calculated the AKs for the standard and modified (0000_460) CO_2 a priori profiles (Fig.VI.10). The difference between two sets of AK (ΔAK) increases as a function of SZA. For small SZA (69-71°) ΔAK does not change much, but with the increase of SZA ΔAK increases progressively. This change in AK explains the shape of ΔX_{CO_2}.

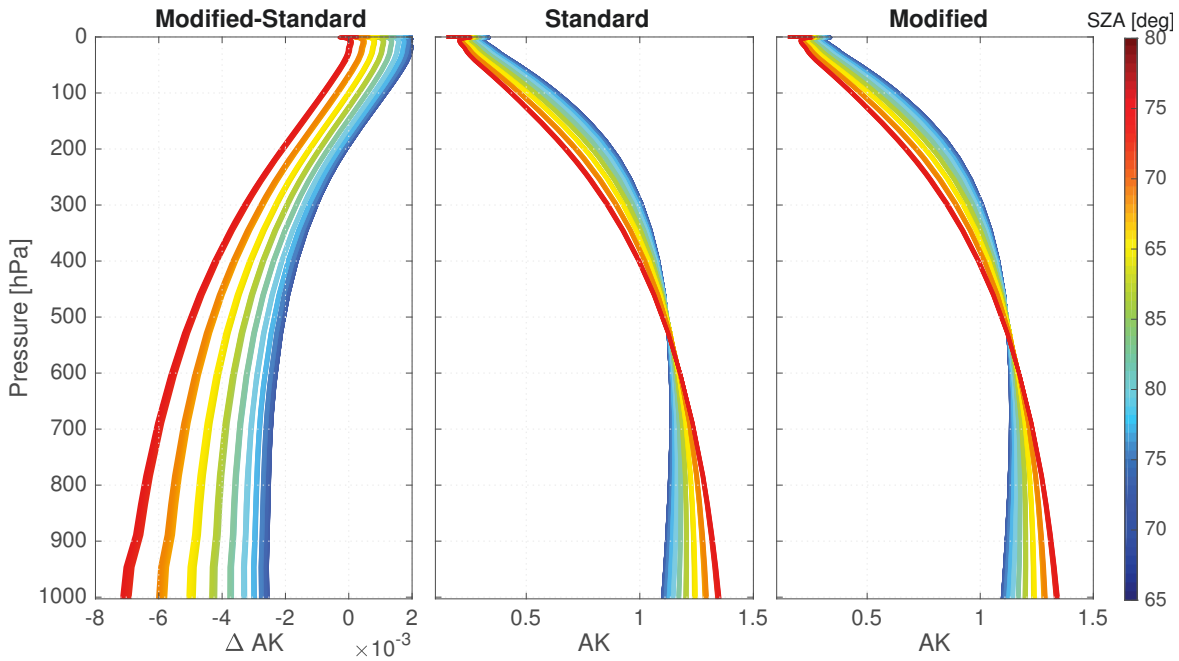

Figure VI.10 – Column averaging kernels calculated for CO_2 by the use of modified (right panel) and standard (middle panel) priors. The left panel shows the difference (modified - standard). The color represents different values of SZAs.

VI.3.2 April 18, 2016 - unpolluted day

Air conditions and set of modified a priori profiles

April 18, 2016 is a day with relatively low concentrations of CO_2 ranging between 410 and 430 ppm (Fig.VI.11). The standard CO_2 prior to that day has a CO_2 concentration at the ground of 414 ppm, which is close to the measured concentrations. The PBL height increases from 600 m to 1800 m during the day and remains constant after 13:00 (the PBL is developed). In order to follow the development of the PBL height during the day, TCCON spectra were divided into five groups. Each group is defined by the corresponding time interval. Table VI.1 contains time intervals for each group, corresponding PBL height and average in situ CO_2 VMR. For each group we have determined the optimal modified priors, as it was done in the case of January 20.

Table VI.1 – Description of each groups of modified CO_2 priors used on April 18, 2016.

Time interval	CO_2 in situ, ppm	PBL height, m	Optimal modified a priori profile	Color
08:00 - 09:00	429±7	710	0500_440	Red
09:00 - 10:00	425±4	1070	1000_430	Green
10:00 - 11:00	420±5	1400	1500_420	Yellow
11:00 - 13:00	418±5	1690	1500_410	Blue
13:00 - 15:00	417±6	1800	1500_410	Pink

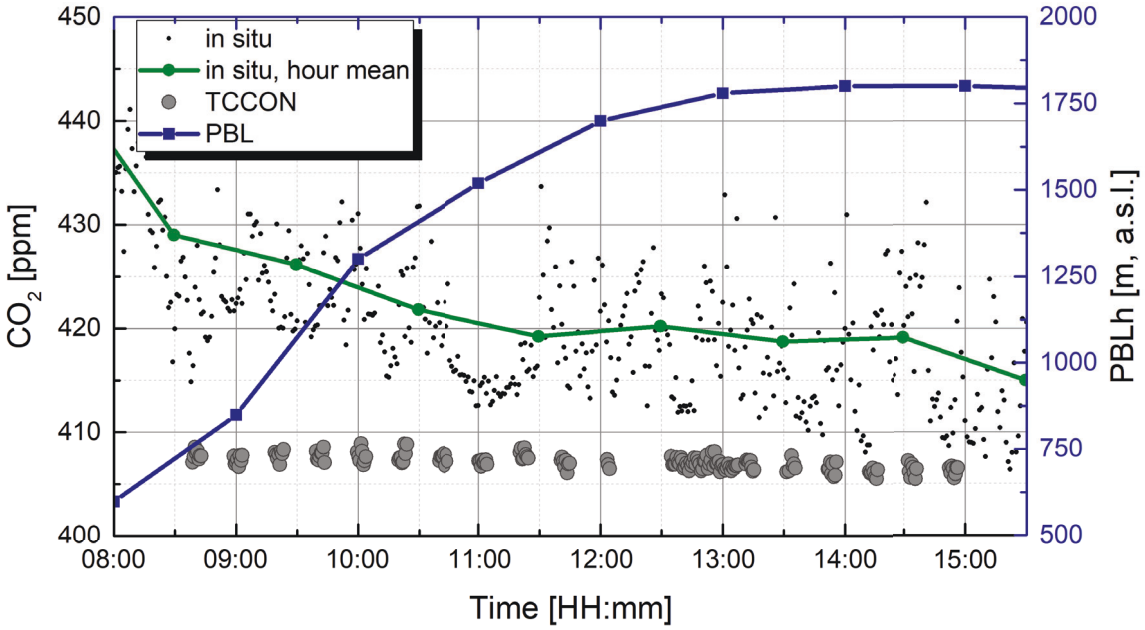

Figure VI.11 – Air mass conditions on April 18, 2016. The black dots are CO_2 in situ measurements and the green curve is the corresponding one hour average. The blue curve shows the LIDAR measurements of the PBL height. Grey circles are TCCON measurement of X_{CO_2}.

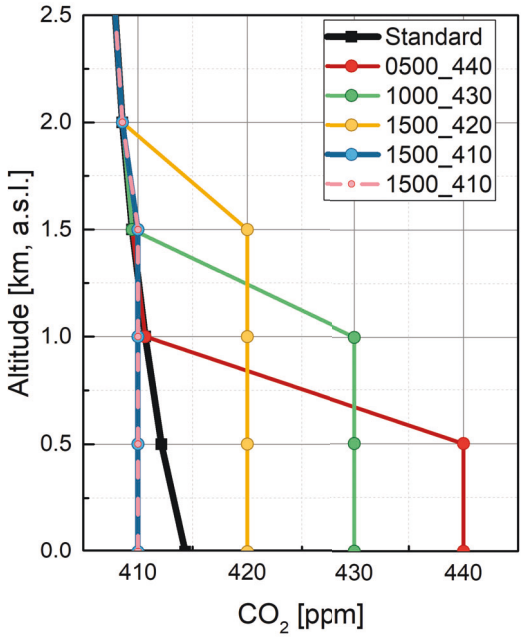

Figure VI.12 – CO_2 a priori profiles used in the April 18 case study.

Among the best fitted modified priors we chose the ones that are closest to the PBL height and in situ CO_2 (fourth column of Table VI.1). For example, for the second group

(09:00 - 10:00), the best fitted a priori profiles are 0500_450, 1000_430 and 1500_420. Since the difference in X_{CO_2} for different best fitted a priori profiles is small, we choose 1000_430 (call it optimal) because it has closest parameters to the PBL height (1070 m) and in situ CO_2 (425). Standard CO_2 and optimal a priori profiles are presented in Fig.VI.12.

Comparison of X_{CO_2}

For each group of spectra we have calculated $X_{CO_2}^{modified}$ with the use of the corresponding optimal CO_2 a priori profiles. The comparison of $X_{CO_2}^{modified}$ with $X_{CO_2}^{standard}$ is shown in Fig.VI.13. For the first three groups, ΔX_{CO_2} stays close to 0.2 ppm and significant improvements of the spectral fit have been obtained (see bottom panel). For the time interval between 11:00 and 15:00 we do not observe significant improvements in the spectral fit, because optimal priors are very close to the standard one (Fig.VI.12), and therefore ΔX_{CO_2} stays around 0 ppm.

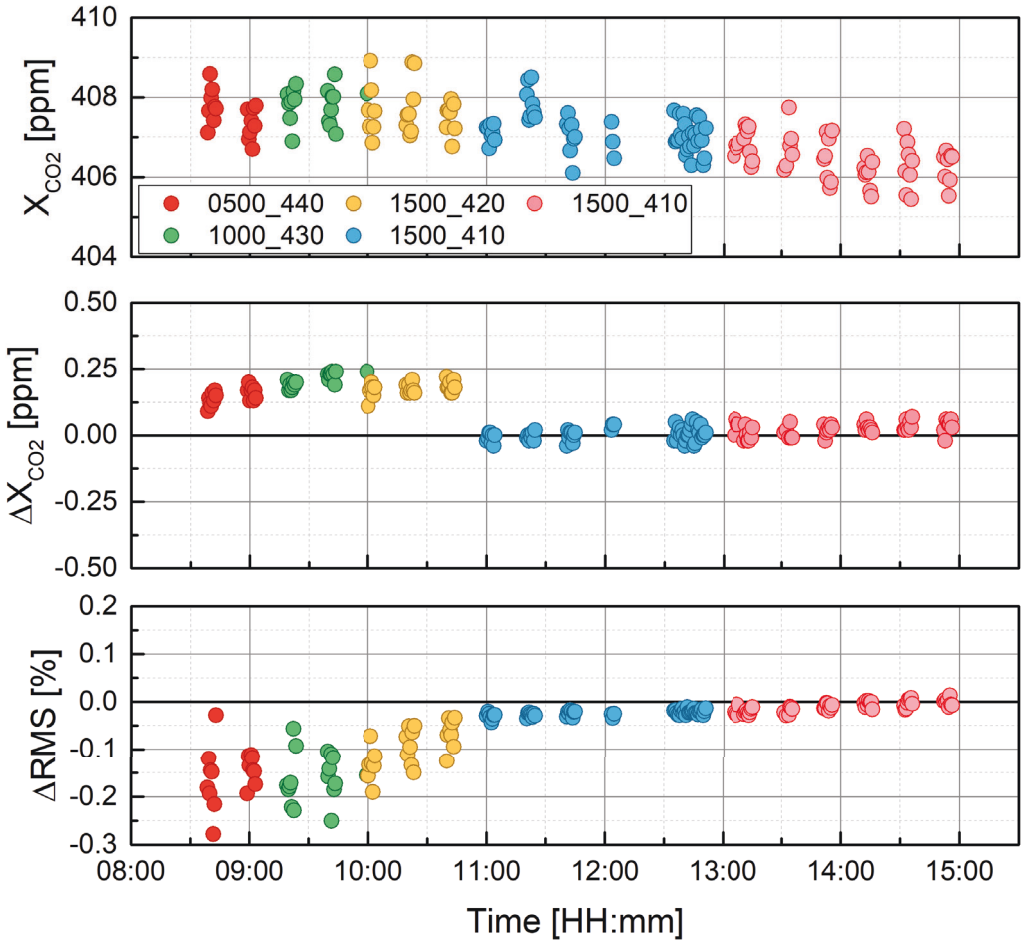

Figure VI.13 – Comparison of X_{CO_2} calculated with standard and modified a priori profiles. Top panel: X_{CO_2} calculated with optimal modified a priori profiles, $X_{CO_2}^{standard}$ is not seen because it is overlapped by $X_{CO_2}^{modified}$; Middle panel: ΔX_{CO_2}; Bottom panel: ΔRMS calculated for each spectrum.

To conclude: On April 18, 2016 the standard CO_2 prior is well suited to evaluate TCCON spectra under unpolluted air conditions in Paris. The modified CO_2 priors does not show significant improvements, since they are close to the standard one.

VI.4 X_{CO_2} calculated with modified CO_2 priors for three years of measurements

In this section we study the influence of a modified CO_2 prior on the retrieved X_{CO_2} over a long time period. This study is concentrated on spectra measured around noon (11:00 - 13:00, UTC), in order to avoid the solar zenith angle dependence of ΔX_{CO_2}, as it was observed for the case of January 20, 2016.

VI.4.1 The set of modified CO_2 priors

For each day of measurements we have prepared one modified CO_2 prior based on the statistical model of the PBL height (Section VI.1.1) and on in situ CO_2 measurements. For the in situ data gaps, we use an interpolation (sine shape fit, Fig.VI.2). Fig.VI.14 shows the comparison of standard priors CO_2 at the ground (black points) with in situ CO_2 measurements (green points are measured and red points are interpolation). The difference

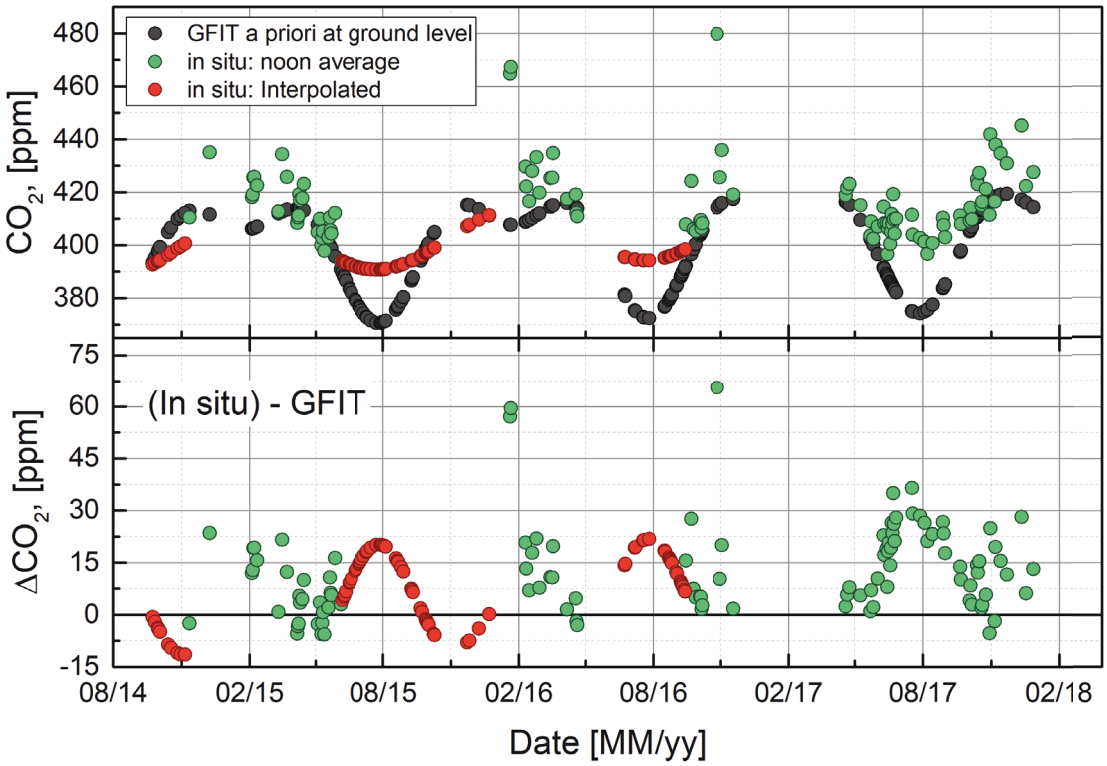

Figure VI.14 – Comparison of CO_2 in situ data with the CO_2 at the ground level of standard a priori profiles. The top panel shows absolute values; bottom panel shows the difference between the two data.

between in situ and GFIT (ΔCO_2, bottom panel) has a clear increase of up to 30 ppm during the summer 2017, and reaches 22 ppm for the interpolated in situ ΔCO_2 data in Summer 2015 and 2016. There are few pollution episodes on January 20 and 21, 2016 (ΔCO_2 = 60 ppm), and November 27, 2016 (ΔCO_2 = 65 ppm).

VI.4.2 X_{CO_2} comparison over the three years period

The comparison of $X_{CO_2}^{standard}$ and $X_{CO_2}^{modified}$ over the three years is presented in Fig.VI.15. On the top panel $X_{CO_2}^{standard}$ (grey points) are mostly covered by other values because they are overlapped by the red and green $X_{CO_2}^{modified}$ points. The difference between $X_{CO_2}^{modified}$ and $X_{CO_2}^{standard}$ (ΔX_{CO_2}) is presented on the middle panel and ΔRMS on the bottom panel.

For summer 2015 and 2016, $X_{CO_2}^{modified}$ is calculated using modified priors based on the interpolation of in situ CO_2 data. ΔX_{CO_2} has a structure of camelbacks and reaches +0.71 ppm and 0.69 ppm for 2015 and 2016 correspondingly. ΔRMS in summer 2015 is mainly negative (negative values mean better fit with modified a priori, see Eq.(VI.1)) and in summer 2016 all of the spectra (except one) are fitted better with modified priors. For summer 2017, $X_{CO_2}^{modified}$ is calculated using modified priors based on the in situ CO_2 measurements. ΔX_{CO_2} has a maximum value of +0.86 ppm and ΔRMS is mainly negative. These high values of ΔX_{CO_2} are caused by the shape of standard CO_2 priors during summer, that underestimate the number of CO_2 molecules in the lower troposphere (Fig.VI.3). GFIT is not able to scale these profiles properly. For other seasons (spring, fall and winter) ΔX_{CO_2} stays within 0.25 ppm, i.e. within the X_{CO_2} precision.

The use of modified CO_2 priors does not always lead to a better spectral fit (Fig.VI.16). For modified priors based on measured CO_2 in situ there are 822 spectra with positive and 2475 spectra with negative ΔRMS. For modified a priori profiles based on the interpolation of in situ CO_2 there are 315 spectra with positive and 1954 spectra with negative ΔRMS. In total 79.6% of spectra are better fitted with modified a priori profiles than with the standard one. Despite on the fit improvements, VSF_{CO_2} calculated with modified CO_2 priors does not differ much from the standard one (see Fig.VI.17). The small improvement ($\sim$0.005) is obtained with modified priors based on the interpolation of the in situ data (red points), but the measured in situ data does not show any significant improvements.

The summer maxima of ΔX_{CO_2} corresponds to the minima of the X_{CO_2} seasonal cycle. Modifying priors leads to a decrease of seasonal amplitude variation of X_{CO_2} but does not effect the annual trend. The bias of 0.5-0.85 ppm is large and clearly exceeds TCCON specifications. The similar effect could probably be observed for other TCCON sites located close to emission sources.

The results of this study have been presented at the IRWG-TCCON 2018 meeting in Cocoyoc, Mexico. As a result of the discussion with other TCCON members, the next version of GGG will have two sets of CO_2 priors: one adopted for unpolluted sites and one adopted for polluted sites, as well as an ability to easily modify a priori profiles of every gas (for this work I made a program that performs modification of CO_2 priors only). From the presentation ("GGG Updates" on June 12, 2018) of G. Toon (responsible for the GGG development): observations of the TCCON VSF_{CO_2} show positive anomalies (VSF_{CO_2} above unity) in the northern hemisphere in July and August (this is what we observe for TCCON-Paris, Fig.VI.4), and negative anomalies throughout the southern hemisphere. This would be corrected in the next version of GGG by adding a latitude dependent gradient and by

reducing the amplitude of the CO_2 seasonal cycle. Then CO_2 priors will probably better fit to the Paris conditions as well.

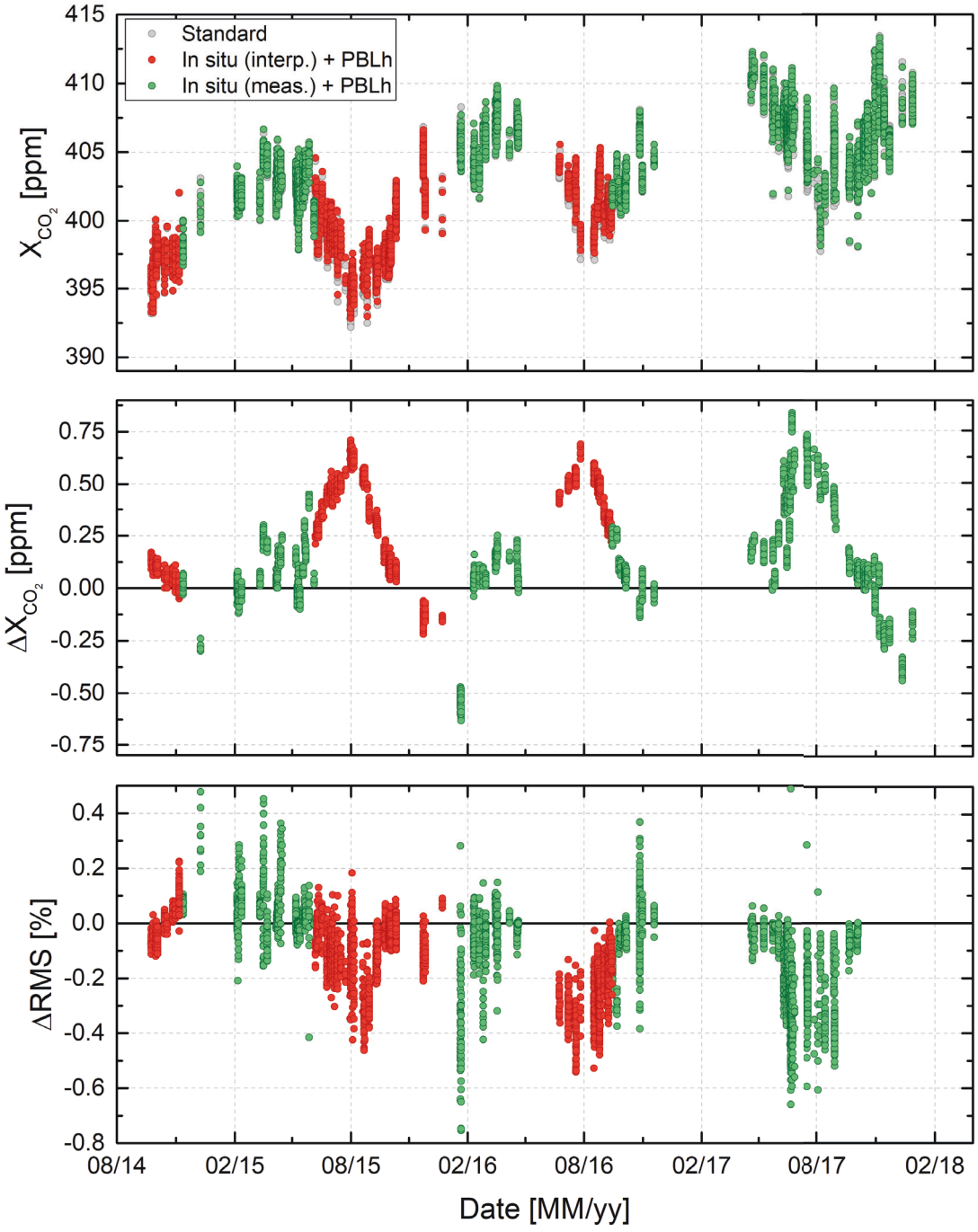

Figure VI.15 – Comparison of $X_{CO_2}^{modified}$ and $X_{CO_2}^{standard}$ over three years of measurements. Top panel shows absolute values; middle panel shows $\Delta X_{CO_2} = X_{CO_2}^{modified} - X_{CO_2}^{standard}$; bottom panel shows ΔX_{CO_2} for each spectrum.

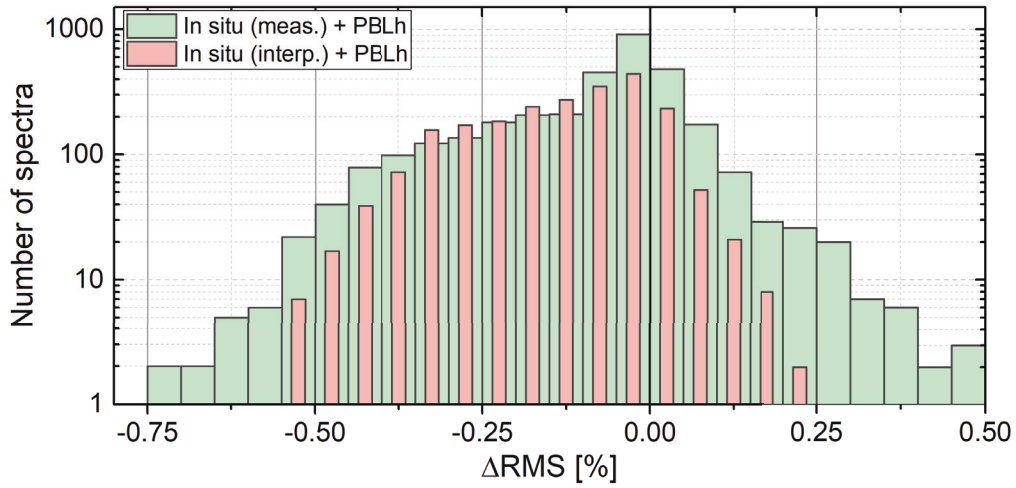

Figure VI.16 – Histogram of ΔRMS.

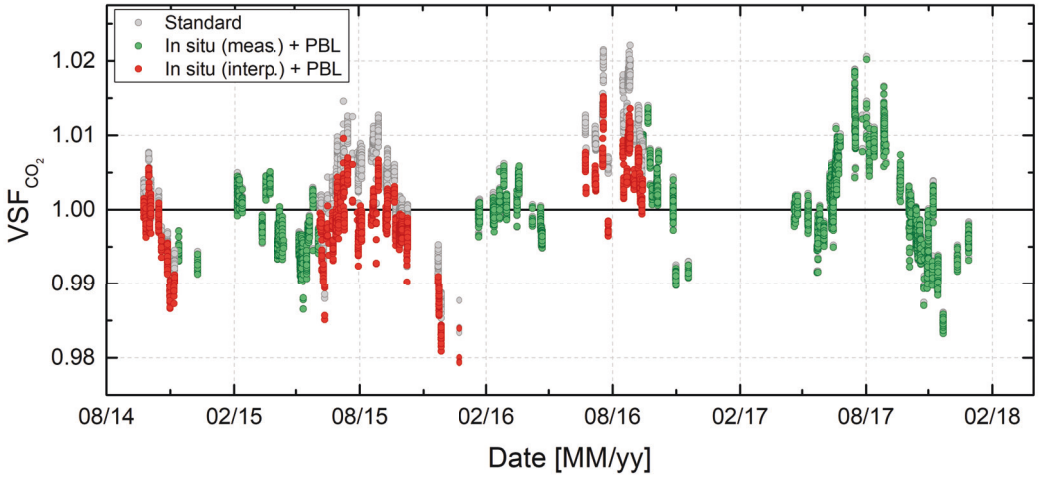

Figure VI.17 – Comparison of VSF_{CO_2} calculated with standard and modified CO_2 priors.

VI.5 X_{CO_2} calculated with modified CO_2 priors during summer 2017

In the previous section we have compared X_{CO_2} calculated with the standard and modified CO_2 priors by using only one CO_2 prior per day and spectra measured between 11:00 and 13:00. In this section we study the intraday changes of ΔX_{CO_2} calculated with the use of four modified CO_2 priors per day, covering various time intervals during the summer 2017.

VI.5.1 Setup: four CO_2 priors per day

This study covers only summer 2017, because of two reasons: 1) the statistical model of the PBL development has been calculated only for the summer period, because then the PBL reaches its annual maximum and it has maximum dynamics caused by strong heat fluxes and warm surface temperatures [54]; 2) in summers 2015 and 2016, there were no CO_2 in situ measurements due to instrumental problems.

We have prepared four sets of modified CO_2 priors based on the CO_2 in situ measurements and the statistical model of the PBL development (see Section VI.1.1). Each set covers different time intervals and PBL conditions (table VI.2).

Table VI.2 – Time intervals and PBL conditions used for four modified CO_2 priors.

	Time interval	PBL conditions	Number of spectra	Color on figures
Set 1	07h - 09h	PBL develops	1013	Red
Set 2	09h - 11h	PBL develops	1289	Green
Set 3	11h - 13h	PBL is developed	1244	Yellow
Set 4	13h - 15h	PBL is developed	1192	Blue

The comparison of CO_2 in situ VMRs with ground VMRs of standard CO_2 priors is presented in Fig.VI.18. The top panel shows absolute values and the bottom panel shows the difference between GFIT priors and in situ ($\Delta CO_2 = CO_2^{\text{in situ}} - CO_2^{\text{GFIT}}$). ΔCO_2 is positive during whole summer of 2017. Morning values of CO_2 VMRs (07h-09h, red points) are always higher than the rest of the day due to the PBL development. The maximum of ΔCO_2 is 75 ppm reached on August 28 and 29.

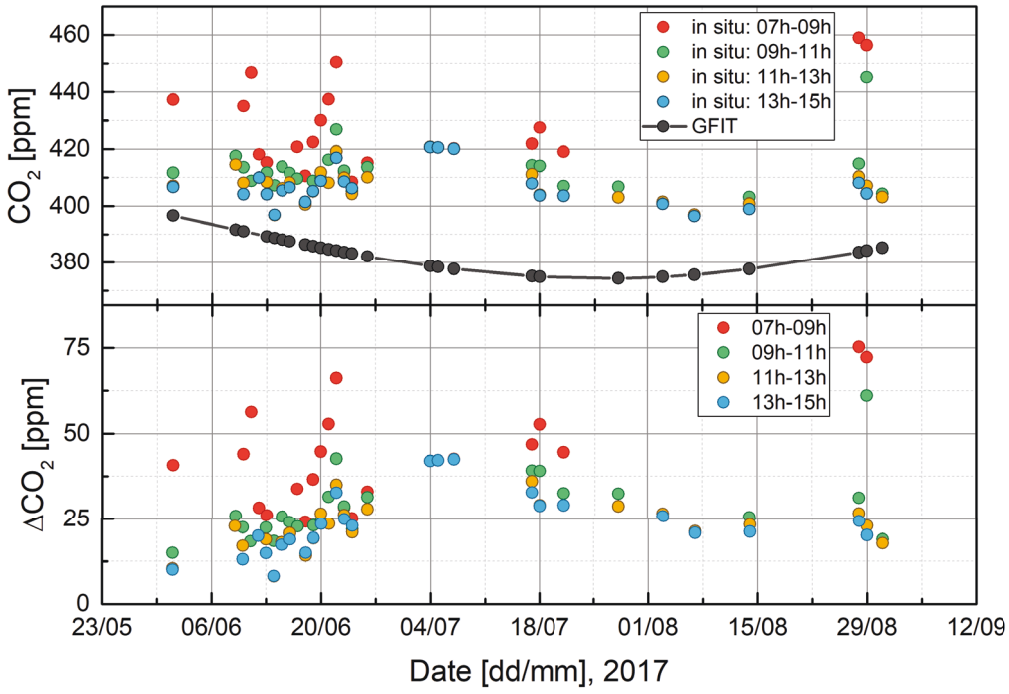

Figure VI.18 – Comparison of CO_2 in situ data with CO_2 at the ground level of CO_2 priors. The top panel shows absolute values; the bottom panel shows the difference between in situ and GFIT data.

VI.5.2 X_{CO_2} comparison

The comparison of $X_{CO_2}^{modified}$ calculated by the use of four modified CO_2 priors per day and for $X_{CO_2}^{standard}$ is presented in Fig.VI.19. ΔX_{CO_2} stays positive during the summer 2017 except two days in August (28 and 29), which will be discussed later in this section. The red points (spectra between 07:00 and 09:00) mostly provide the lowest values of ΔX_{CO_2} and have the maximum of 0.64 ppm on June 22 (ΔCO_2 is 66 ppm). The yellow points (spectra between 11:00 and 13:00) are with the highest values of ΔX_{CO_2}. The yellow points are exactly the same case that was studied in the previous section with the ΔX_{CO_2} maximum of +0.86 ppm. Green and blue points basically take the place between red and yellow points. Concerning the spectral fit improvements, almost all of the spectra (99.7%) are better fitted with modified CO_2 priors, especially noticeable for the red points.

In order to have a better representation of how each of the CO_2 priors influence on ΔX_{CO_2} we have selected four representative days (Fig.VI.20). The setup for each CO_2 prior is summarized in Table VI.3. On June 13, the transitions of ΔX_{CO_2} between two neighbor priors have no gaps, that can be observed on July 7 and August 29 between green and yellow points. On July 7 the ΔX_{CO_2} gap of 0.21 ppm is explained by the change in priors where the BPL height is changed from 500 m to 1000 m and CO_2 VMR is changed only by 10 ppm, i.e. yellow prior have much more molecules added than the green one. On August 29, we observe the opposite case: ΔX_{CO_2} gap is -0.45 ppm caused by a significant change in CO_2 VMR by 38.1 ppm and a change in PBL height from 1000 m to 1500 m, i.e the green prior have more added molecules than the yellow one. On August 28, this gap is observed between the red and green priors but is insignificant (0.05 ppm). These gaps would probably

Table VI.3 – Setup of each modified CO_2 priors on four selected days.

Date	Time	in situ CO_2, ppm	GFIT CO_2, ppm	$CO_2^{\text{in situ}} - CO_2^{\text{GFIT}}$, ppm	PBLh [m]
13/06/2017	07h-09h	415.3±1.1	389.3	26.0	500
	09h-11h	411.7±1.0		22.4	1000
	11h-13h	408.3±1.1		19.0	1500
	13h-15h	404.1±1.2		14.8	1500
18/07/2017	07h-09h	427.6±1.8	377.6	50.0	500
	09h-11h	414.0±2.3		36.4	500
	11h-13h	403.9±0.9		26.3	1000
	13h-15h	403.8±0.6		26.2	1000
28/08/2017	07h-09h	459.0±2.2	383.7	75.3	500
	09h-11h	414.9±6.9		41.2	1000
	11h-13h	410.4±1.2		26.7	1500
	13h-15h	408.1±1.1		24.4	1500
29/08/2017	07h-09h	456.4±9.5	384.2	72.2	500
	09h-11h	445.2±8.5		61.0	1000
	11h-13h	407.1±1.7		22.9	1500
	13h-15h	404.4±0.9		20.2	1500

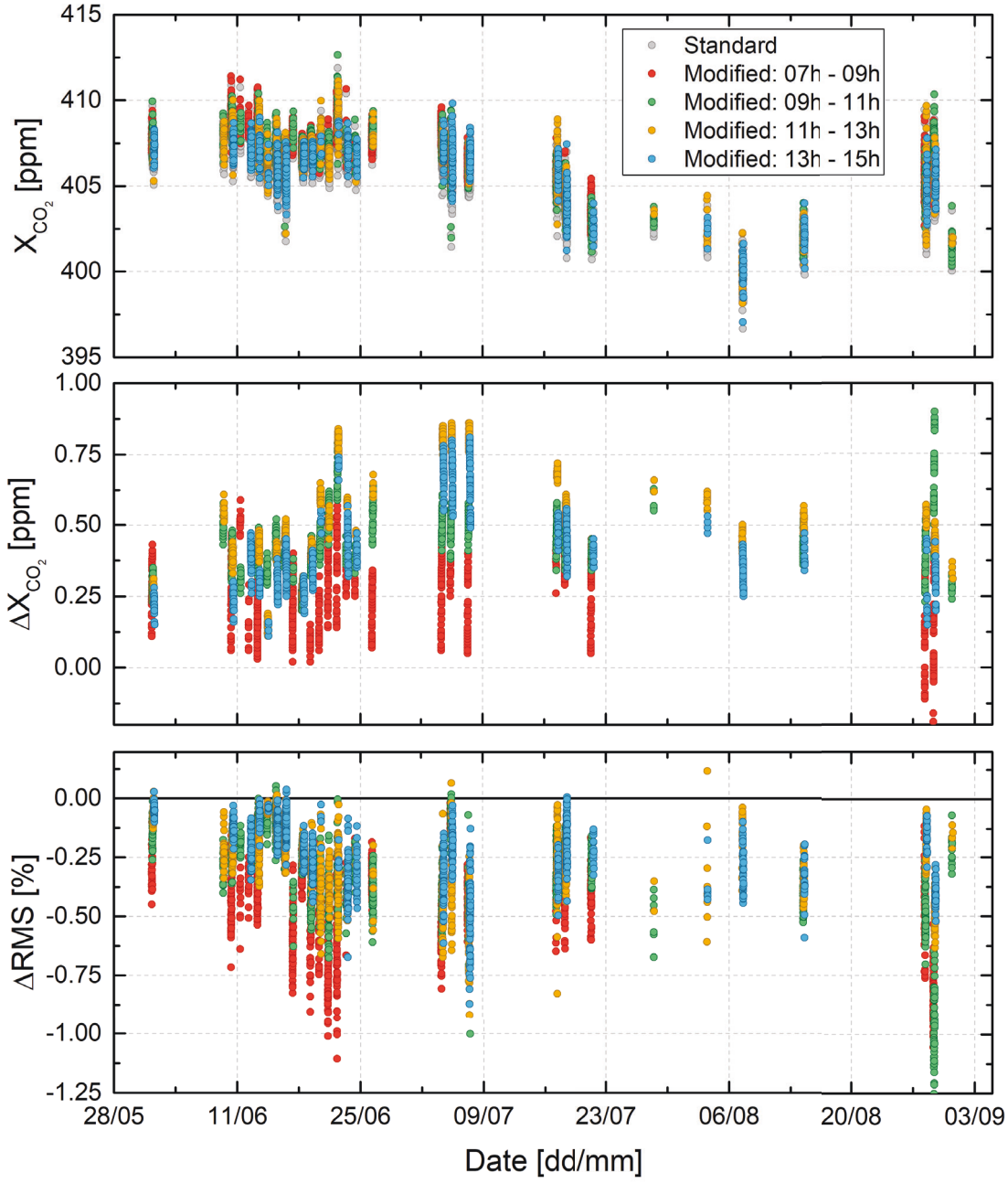

Figure VI.19 – Top panel shows X_{CO_2} calculated with the use of standard CO_2 a priori profiles. Bottom panel shows the ΔX_{CO_2} calculated for four sets of CO_2 a priori profiles.

disappear if we use more CO_2 priors per day and a thinner altitude grid, but there are many unknown parameters such as the CO_2 VMR profiles inside of the PBL: we assume that it is well mixed and we correspondingly use a constant CO_2 VMR inside of the PBL, but in the reality it is not always well mixed [53]. As well we have no information about the transition between PBL and the free troposphere, we simply stick the modified priors to the standard priors at the level above the PBL.

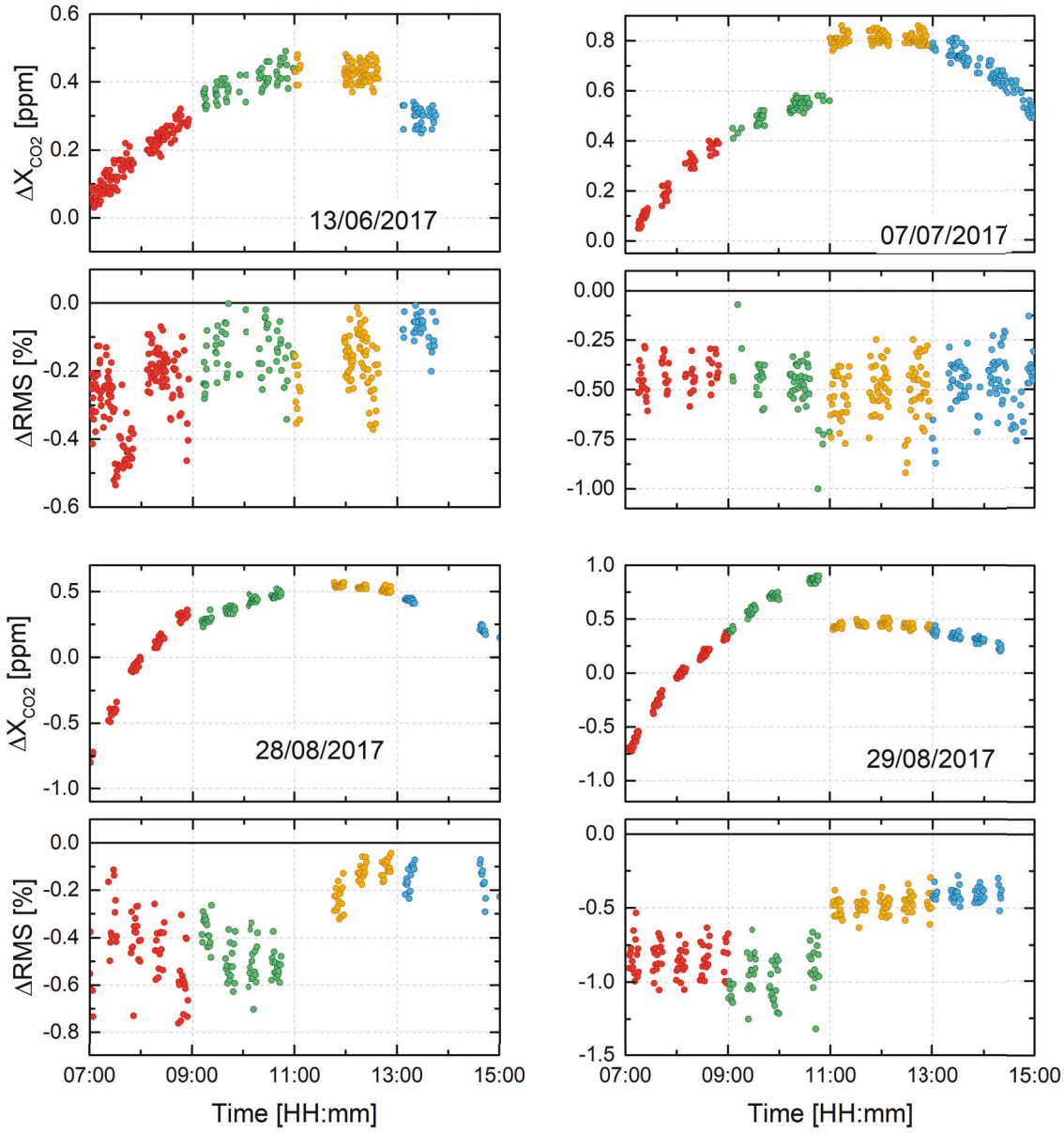

Figure VI.20 – Four selected days in summer 2017. ΔX_{CO_2} calculated with four modified CO_2 priors per day are separated by colour, the same colours as in Fig.VI.19.

VI.6 Comparison of OCO-2 and TCCON-Paris X_{CO_2} measurements using standard and modified CO_2 priors

The Orbiting Carbon Observatory-2 (OCO-2) is NASA's first Earth-orbiting satellite dedicated to measuring carbon dioxide column-averaged dry air mole fraction of CO_2 to better understand the carbon cycle. OCO-2 was launched on July 2, 2014 into low-Earth orbit and joined the A-train satellite constellation (https://atrain.nasa.gov/intro.php). It measures near-infrared spectra of sunlight reflected off the Earth's surface, which are analyzed

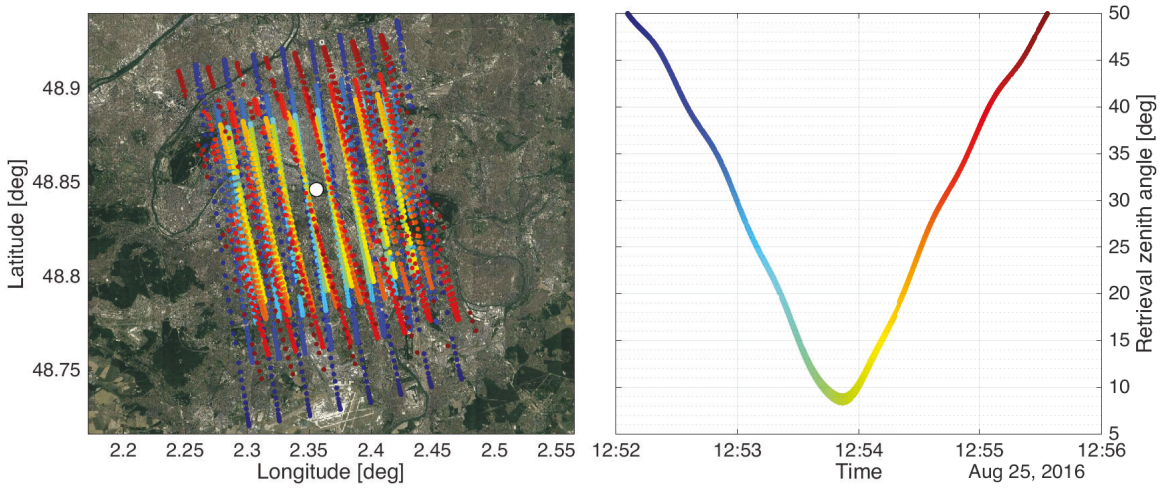

Figure VI.21 – OCO-2 target mode over TCCON-Paris on August 25, 2016. Left figure: the location of the measurements in latitude and longitude. Left panel: the zenith angles viewed by OCO-2.

to calculate X_{CO_2}. TCCON is the primary ground-based validation network for OCO-2 [14].

OCO-2 has three viewing modes: nadir mode, in which the instrument points straight down at the surface of the Earth; glint mode, in which the instrument points just off the glint spot on the surface; and target mode, in which the observatory is commanded to scan about a particular point on the ground as it passes overhead. The three modes serve different purposes: the nadir and glint-mode measurements are normally used for scientific analyses, and the target mode is used primarily as part of the OCO-2 bias correction procedure.

TCCON-Paris is one of the TCCON sites used for OCO-2 target validation mode (Fig.VI.21). The spacecraft scans across the site as it passes overhead to sweep across the ground several times over a period of about 4.5 min. During the target maneuver the spacecraft records few thousand spectra that are analyzed to retrieve X_{CO_2} (see Fig.VI.22). The target maneuver presented on August 25, 2016 has 4395 soundings.

The TCCON data are then used for the $X_{CO_2}^{OCO-2}$ bias characterization and correction. In Table VI.4 the comparison of $X_{CO_2}^{OCO-2}$ and $X_{CO_2}^{TCCON}$ calculated by the use of standard and modified CO_2 priori is presented. For the presented days the effect of modified CO_2 priors is increasing $X_{CO_2}^{TCCON}$ value, which increases the bias between TCCON and OCO-2, except July 18, 2017 where the bias is decreased form -0.6 to -0.1 ppm. If we assume that $X_{CO_2}^{TCCON}$ calculated by the use of modified CO_2 priors has better accuracy then using standard priors, then the bias correction of OCO-2 data should be also performed using $X_{CO_2}^{TCCON}$ calculated using modified priors for every TCCON site that suffers from local pollution sources.

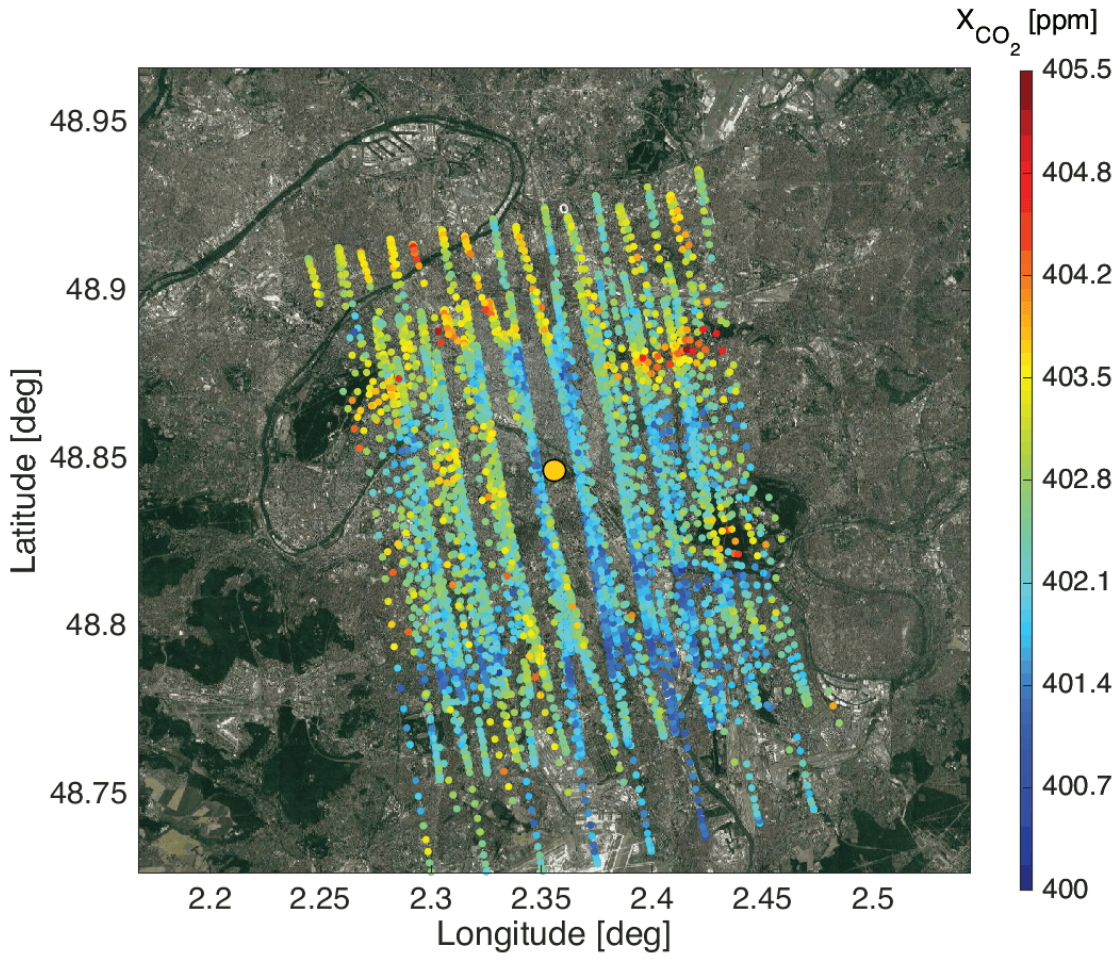

Figure VI.22 – OCO-2 target mode over TCCON-Paris on August 25, 2016. Colored points are X_{CO_2} measured by OCO-2 during the target maneuver; yellow circle is X_{CO_2} measured by TCCON-Paris.

Table VI.4 – The comparison of X_{CO_2} measured by OCO-2 and TCCON. TCCON data is calculated by the use of standard ($X_{CO_2}^{standard}$) and modified ($X_{CO_2}^{modified}$) CO_2 priors. The last two columns in the table are: $\Delta X_{CO_2}^{standard} = X_{CO_2}^{standard} - X_{CO_2}^{OCO-2}$ and $\Delta X_{CO_2}^{modified} = X_{CO_2}^{modified} - X_{CO_2}^{OCO-2}$. All of the values are in ppm.

Date (mode)	OCO-2	$X_{CO_2}^{standard}$	$X_{CO_2}^{modified}$	$\Delta X_{CO_2}^{standard}$	$\Delta X_{CO_2}^{modified}$
11/03/2016 (target)	407.2	408.0	408.1	+0.8	+0.9
25/08/2016 (target)	402.3	403.7	404.3	+1.4	+2.0
05/10/2016 (nadir)	401.5	402.0	402.0	+0.5	+0.5
18/06/2017 (nadir)	405.4	406.6	406.9	+1.2	+1.5
18/07/2017 (target)	404.6	404.0	404.5	-0.6	-0.1

VII – Comparison of EM27/SUN measurements with TCCON

This chapter describes two short campaigns of collocated EM27/SUN and TCCON measurements. The Total Carbon Column Observing Network (TCCON) has already been described in previous chapters. The EM27/SUN is a commercial low resolution spectrometer, used for the measurements of solar absorption spectra, described in Section VII.1.2. The network of EM27/SUN spectrometers is called **CO**llaborative **C**arbon **C**olumn **O**bserving **N**etwork (COCCON), see Section VII.1.1.

The first campaign was made during spring 2017. EM27/SUN measurements were used to characterize the X_{CO_2} bias between two TCCON sites located in France: TCCON-Orleans and TCCON-Paris. The campaign included six days of collocated measurements of EM27/SUN with two TCCON sites: four days in Paris and two days in Orleans, see Section VII.2. The second campaign of collocated measurements was made during spring 2018 at the TCCON-Paris. The campaign includes the comparison of EM27/SUN data with TCCON high and low resolution measurements, and the biases between three types of measurements are described, Section VII.3.

VII.1 EM27/SUN network

VII.1.1 COCCON

Ground based networks of atmospheric trace gas measurements using FTIR spectrometers such as TCCON [6] and IRWG-NDACC [26] provide high precision measurements of trace gases on a good temporal scale. TCCON has a good coverage in Europe, North America and Oceania but it has sparse coverage over Asia and no officially operational TCCON station in Africa, South America and North Asia (Russia). To deploy a TCCON station needs a large infrastructure to be set up and maintained, that is difficult in some remote regions. Spaceborn atmospheric measurements, on the other hand include satellite missions such as the Orbiting Carbon Observatory-2 [56], the Greenhouse Gases Observing Satellite (GOSAT [57]) and others. The main advantage of the satellite measurements is their global coverage, but this happens at the cost of actually poor temporal resolution (repeat cycle for OCO-2 is 16 days [58], 3 days for GOSAT and 6 days for GOSAT-2 (http://www.gosat-2.nies.go.jp/about/spacecraft_and_instruments/)).

COCCON is a network of portable low resolution FTS - Bruker EM27/SUN instruments [59]. The main advantage of EM27/SUN instruments is that they are easy to deploy and

operate, because of a light weight (∼25 kg) and compact size (80x43x48 cm^3)) and low cost as compared to TCCON station. The network of EM27/SUN instruments extends the global density of atmospheric column measurements of greenhouse gases [60–62]. EM27/SUN have a good long-term stability and precision of measuring total columns of trace gases [59, 63]. They have been shown to measure the same variations of atmospheric gases within a day as the high-resolution spectrometers of the Total Carbon Column Observing Network [59]. They were used in campaigns for the quantification of local sinks and sources [60, 64].

VII.1.2 EM27/SUN - instrument description

EM27/SUN is a commercially manufactured spectrometer by Bruker. It is made of low resolution spectrometer Bruker EM27 combined with a camera-based solar tracker (CamTracker) developed by KIT and Bruker [65], see Fig.VII.1.

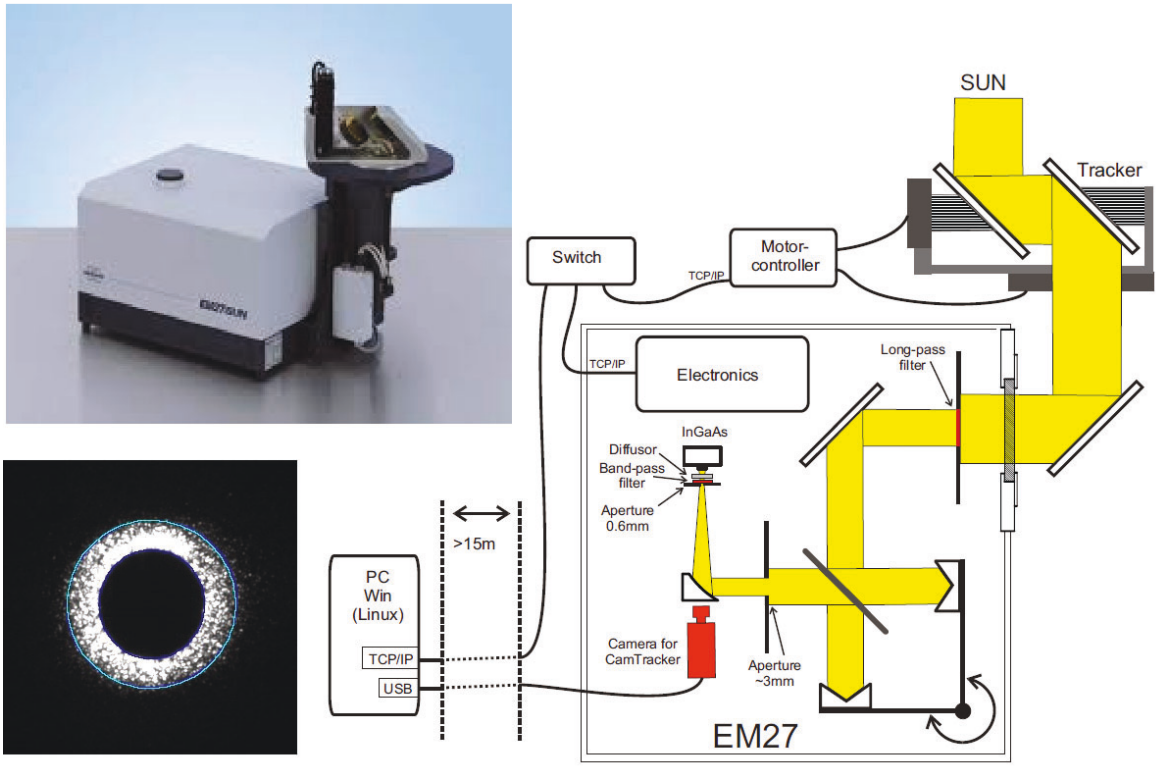

Figure VII.1 – Top left: A photo of EM27/SUN spectrometer. Bottom left: CamTracker image of the solar disk over the detector aperture, blue circle is a fit to solar image. Right: principle scheme of EM27/SUN instrument. - Source :[1]

The solar tracker follows the movement of the sun and reflects the solar radiation into the spectrometer. The solar tracker consists of two plane mirrors that rotate along an azimuth and elevation axis driven by two stepper motors. A camera inside the spectrometer observes solar images centered about the entrance aperture of the detector. The solar images are then

[1]Source : Photo of the EM27/SUN instrument is taken from https://www.bruker.com. CamTracker image and EM27/SUN scheme are taken from [65].

processed to determine and adjust the position of the solar tracker by fitting circles to solar and aperture images, the same principles are used for TCCON described in section II.2.2.

The EM27 Fourier transform spectrometer is a pendulum interferometer with two cube corner mirrors and a CaF_2 beamsplitter. The cube corner mirrors can move up to 0.45 cm, leading to maximum optical path difference of 1.8 cm (4×0.45 cm) which corresponds to a spectral resolution of 0.5 cm^{-1}.

The standard EM27/SUN configuration uses an InGaAs detector sensitive to the spectral range of 5500 – 12000 cm−1, Fig.VII.2 blue spectrum. The standard detector range covers commonly used microwindows for the retrieval of O_2, CO_2, CH_4, and H_2O. The EM27/SUN can also be equipped with a second detector [66] which extends the standard spectral range to 4000 - 5500 cm^{-1}, covering CO and N_2O absorption bands, Fig.VII.2 red spectrum. In this thesis only the spectra measured with the standard InGaAs detector are used for the retrievals of gas columns.

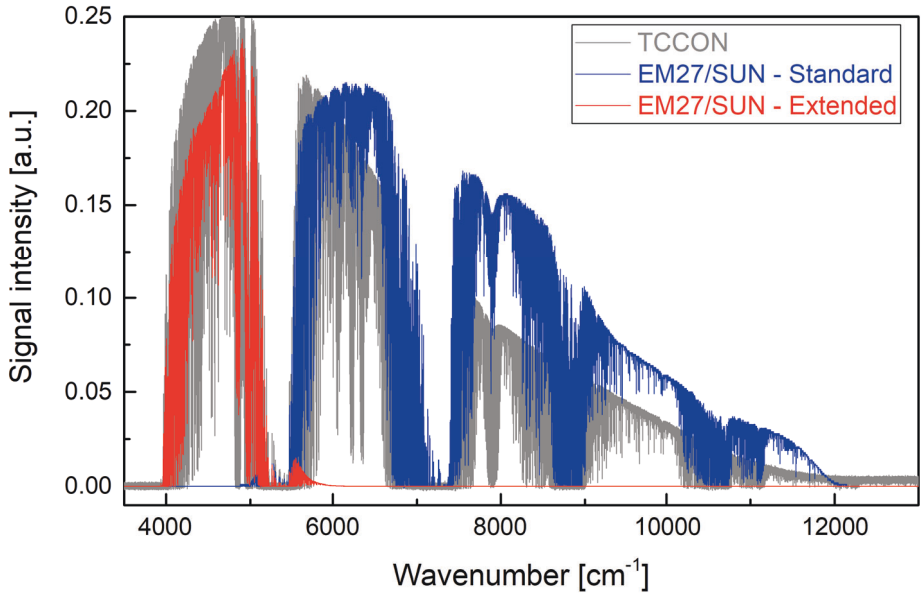

Figure VII.2 – Solar absorption spectra measured by EM27/SUN. The blue curve is obtained by the use of the standard InGaAs detector, the red curve by the use of the second detector. The gray curve is a TCCON spectrum for comparison.

VII.1.3 Data processing

The most commonly used retrieval softwares for the analysis of EM27/SUN spectra are GGG [30] and PROFFIT [67]. GGG is commonly used by the North American community while PROFFIT is commonly used by the European community. For this work I use GGG2014 in order to be consistent with TCCON.

EM27/SUN records double sided interferograms with a maximum path difference of 1.8 cm. The interferogram contains two parts: forward and backward interferograms. GGG separates forward and backward interferograms, corrects source brightness fluctuations and converts each interferogram into one spectrum by applying a Fourier transformation and phase correction, see Section IV.3.1. The resulting spectra are then fitted by GFIT (fitting

program from GGG) to retrieve the gas columns. Table VII.1 presents spectral microwindows used for EM27/SUN spectra analysis by GFIT.

Table VII.1 – Spectral windows used for the analyses of EM27/SUN spectra.

Molecule	Central wavenumber cm^{-1}	Window Width cm^{-1}	Interfering Species
CO_2	6220.00	80.0	H_2O, HDO, CH_4
	6339.00	85.0	H_2O, HDO
CH_4	5938.00	116.00	CO_2, H_2O, N_2O
	6002.00	11.10	CO_2, H_2O, HDO
	6076.00	138.00	CO_2, H_2O, HDO
O_2	7885.00	240.00	H_2O, HF, CO_2
H_2O	6076.90	3.85	CH_4, HDO, CO_2
	6255.95	3.60	CO_2, HDO
	6301.35	7.90	CO_2, HDO
	6392.45	3.10	HDO
	6401.15	1.15	H_2O, HDO
	6469.60	3.50	CO_2, HDO
HDO	6330.05	45.50	H_2O, CO_2
	6377.40	50.20	H_2O, CO_2

Then the gas columns are converted to X_{gas} by dividing the gas column by the oxygen column, as described in section IV.3.4. X_{gas} are then corrected for the airmass dependent artifact by applying an air-mass-dependent correction factor. The airmass correction factors are the same as for TCCON, see Section IV.3.8. Then X_{gas} is calibrated to WMO standard by applying a scaling factor, see Section IV.3.7.

The double-sided interferograms were recorded by averaging 10 scans for forward and backward spectra with the maximum resolution of 0.5 cm^{-1}. The scanner velocity is set to 10 kHz and one measurement takes about 58 s.

VII.2 Collocated TCCON and EM27/SUN measurement in Paris and Orleans in Spring 2017

All TCCON sites are supposed to be calibrated by aircraft in situ profile measurements, but for some of the sites this can not be done. TCCON-Paris is one of these sites, because civil aircraft flights are prohibited over Paris. The closest calibrated site is TCCON-Orleans, located at ∼100 km south of Paris, Fig.VII.3.

Figure VII.3 – Map of the two TCCON sites in France: Paris and Orleans. - Source :[2]

It is almost impossible to move the TCCON-Paris instrument to TCCON-Orleans (or vice versa) for side by side measurements in order to investigate the biases between the two instruments. Nevertheless, the small size and weight of the EM27/SUN makes it ideal as a transfer standard between the two TCCON sites. In the short measurements campaign during spring 2017 we have performed measurements at the TCCON with the goal to compare two TCCON instruments.

VII.2.1 Campaign description and setup

The campaign includes six days of collocated TCCON and EM27/SUN measurements. The schedule of EM27/SUN measurement is presented in Table VII.2. The EM27/SUN instrument was taken on lease from Karlsruhe Institute of Technology. It was shipped to the TCCON-Paris site on April 16, 2017. The EM27/SUN was placed on the roof terrace at Jussieu campus of Sorbonne Université (48.8465°N, 2.356°E, 60 m a.s.l.) at a few meter from the TCCON solar tracker, Fig.VII.4(a). Two days of collocated measurements were performed in Paris and the EM27/SUN was then transferred to the TCCON-Orleans site (47.965N°E, 2.113°E, 130 m a.s.l.).

[2]Source : Picture is made of Google maps: https://maps.google.com/

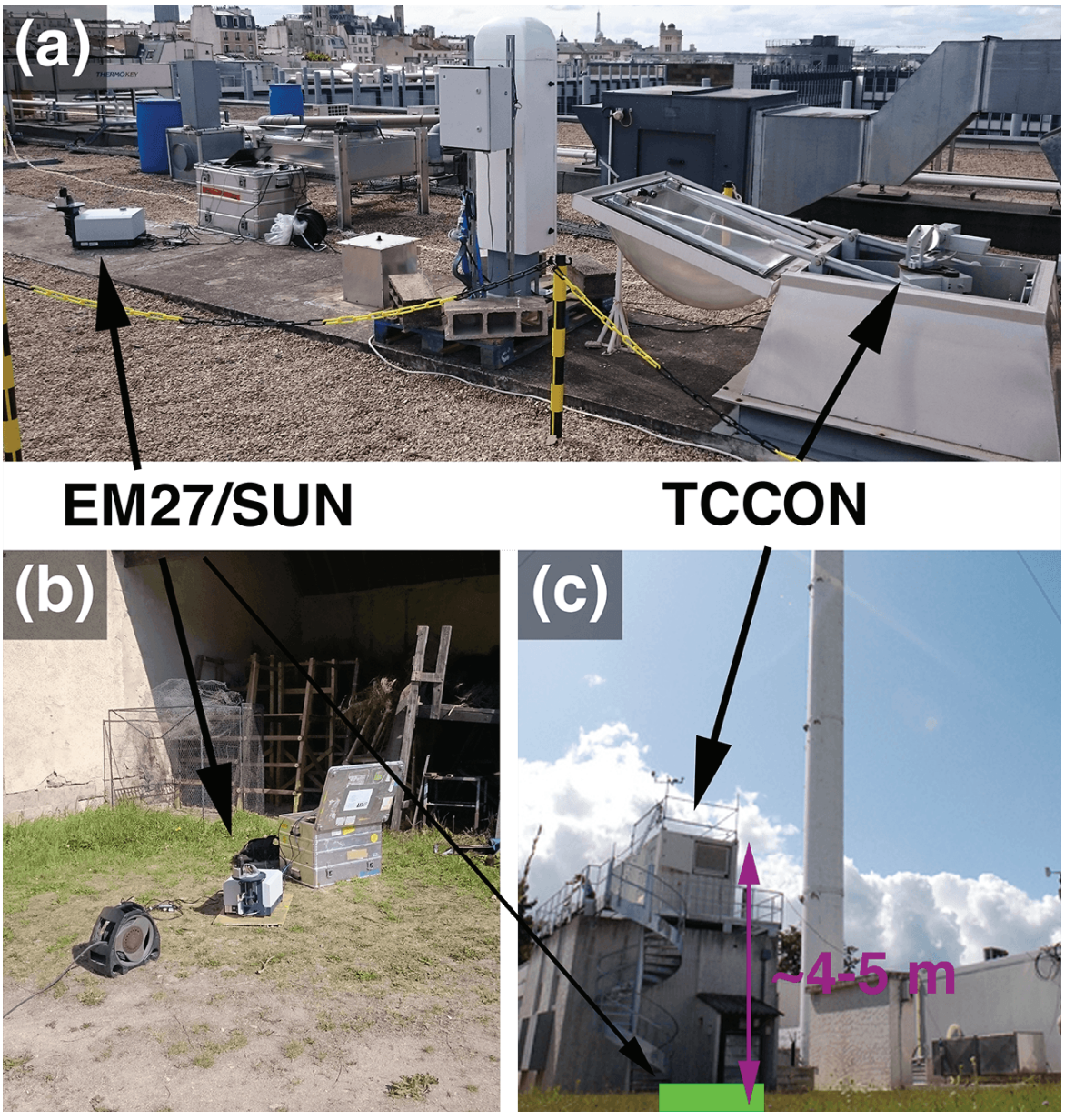

Figure VII.4 – Photo of EM27/SUN placement. (a) - roof terrace at Jussieu campus of Sorbonne Université, (b) - farm, close to TCCON-Orleans, (c) - TCCON-Orleans, green square shows the position where EM27/SUN was placed. - Source :3

The TCCON-Orleans site is located in a forest area, isolated from anthropogenic pollution sources. The TCCON-Orleans instrument is placed inside of a shipping container, with the solar tracker mounted on top of the container's roof, 4-5 m above the ground, Fig.VII.4(c) . On the first day, the EM27/SUN was placed in the farm, 300 m from the TCCON-Orleans, Fig.VII.4(b). On the second day it was placed in close proximity to the TCCON container, Fig.VII.4(c). Then the EM27/SUN was delivered back to Paris for two additional days of measurements.

Table VII.2 – Dates and location of EM27/SUN measurements collocated with TCCON in 2017.

Date	Location
19/04/2017	Paris
20/04/2017	Paris
21/04/2017	Orleans
24/04/2017	Orleans
09/05/2017	Paris
10/05/2017	Paris

a) Pressure note

During the measurements in Orleans the EM27/SUN instrument was never placed at the same altitude as the solar tracker of the TCCON instrument. On April 24, 2017 EM27/SUN was placed on the ground level near the TCCON-Orleans instrument. This makes a difference in altitude of ∼4-5 m which is equivalent to ∼0.5 hPa. On April 21, 2017 EM27/SUN was placed on the farm which is 300 m away and 10 meters below (from GPS data) than the TCCON-Orleans. At the Paris site the EM27/SUN was placed at the same altitude as the TCCON solar tracker. Differences in altitudes could lead to errors in the retrieved columns. Fortunately, the EM27/SUN was supplied with a Thermo Hygrometer Barometer PCE-THB 40 (next THB40). It measures the pressure with a precision of ±1 hPa, while the TCCON's barometers have a precision of ±0.1 hPa.

Comparison of the pressure measured by THB40 and both TCCON barometers (Paris and Orleans) are presented in Fig.VII.5 (top panel). At Paris the difference in pressure (TCCON - THB40) is between 0.5 and 1.25 hPa and at Orleans it is between 0.25 and 0.75 hPa. The difference in pressure is due to poor or degraded calibration of THB40 and is smaller for Orleans because of the difference in altitude between THB40 and TCCON-Orleans pressure sensors. The X_{CO_2} calculated with two pressure sets for both sites is presented in Fig.VII.5 (two bottom panel). The difference (ΔX_{CO_2}) between two datasets is small +0.015% (∼0.06 ppm) but not negligible. For X_{CH_4} the difference is -0.06% (∼ 1 ppb). In the next section, all of the EM27/SUN spectra are treated using the THB40 pressure sensor data in order to have consistent EM27/SUN measurements at two sites.

[3]Source : (a) and (b) are personal photos, (c) is taken from https://tccon-wiki.caltech.edu/Sites/Orleanss.

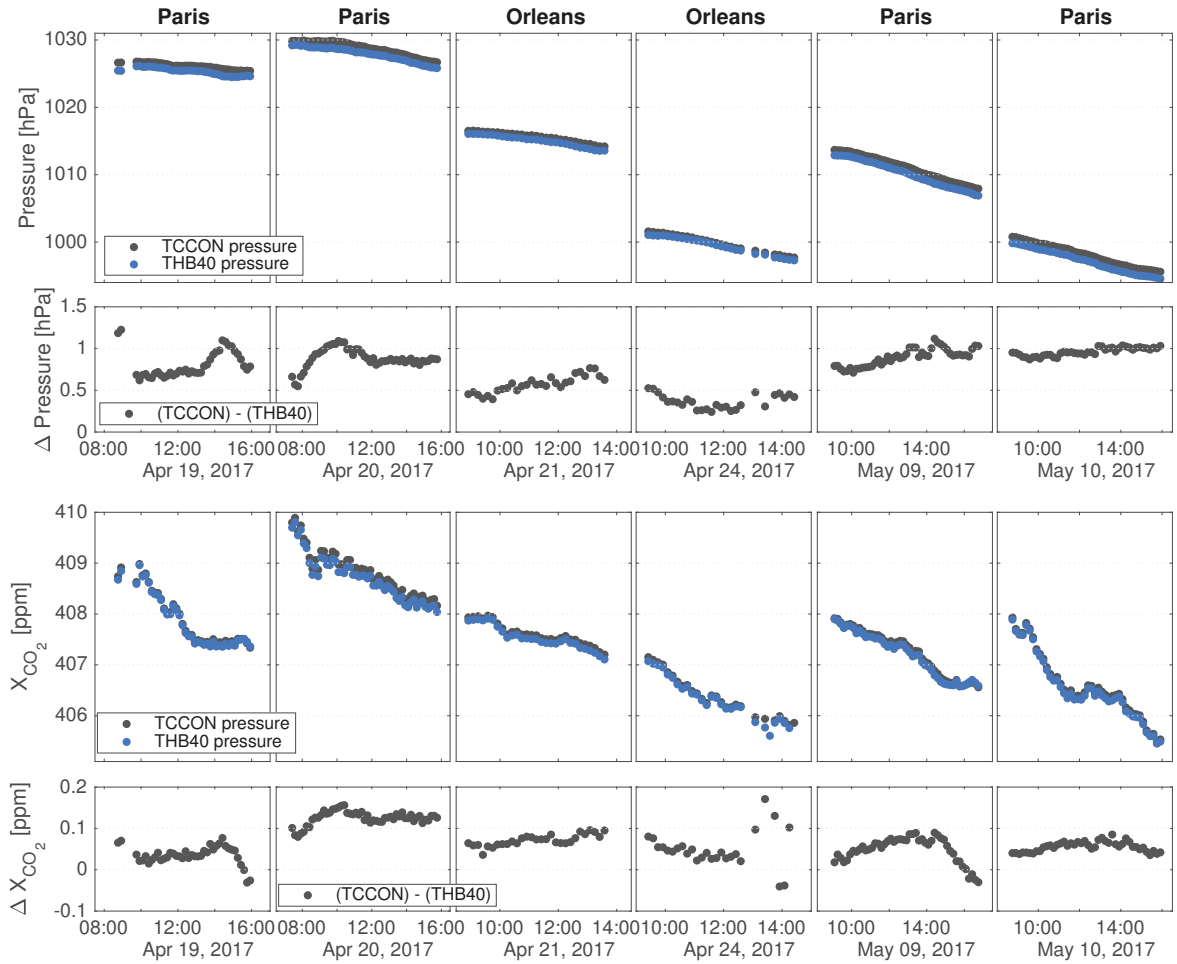

Figure VII.5 – Top panel: Comparison of the pressure measured by THB40 and TCCON's barometers; Bottom panel: comparison of X_{CO_2} calculated with two pressure datasets.

VII.2.2 Data comparison

a) Unscaled data

All of the EM27/SUN spectra are analyzed using the GGG2014 and THB40 pressure sensor dataset. TCCON-Orleans data is downloaded from TCCON data archive: https://tccondata.org/. All of the TCCON products in this section are high resolution (0.02 cm^{-1}) while EM27/SUN is low resolution (0.5 cm^{-1}). The effect of different spectral resolutions is discussed in Section VII.3. To compare measurements between the TCCON and the EM27/SUN instruments, all of the data (X_{gas}) were averaged over 10 minute bins in order to reduce the variance of binned difference [64]. Averages are weighted by the calculated precision of X_{gas} measurements (X_{gas}^{error}) and calculated by:

$$\overline{X}_{gas} = \frac{\sum_i X_{gas,i} \times (X_{gas,i}^{error})^{-2}}{\sum_i (X_{gas,i}^{error})^{-2}}$$

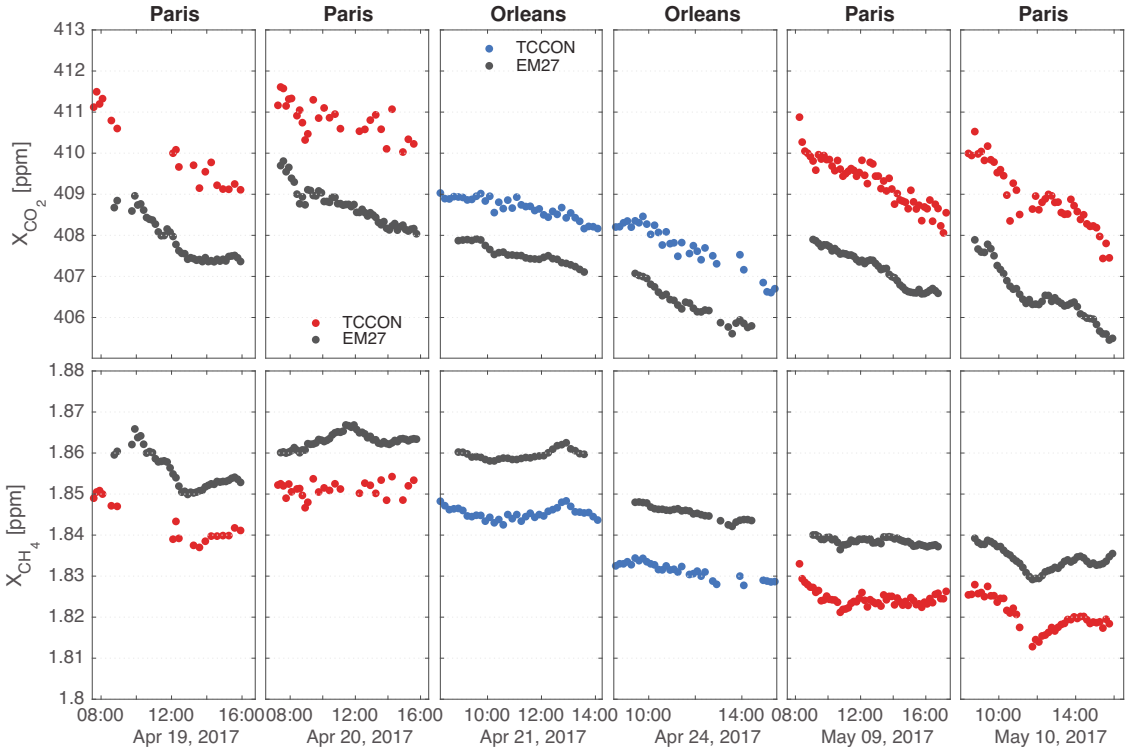

Figure VII.6 – X_{CO_2} (top panel) and X_{CH_4} (bottom panel) measured by EM27/SUN (black points), TCCON-Paris (red points) and TCCON-Orleans (blue points).

where $X_{gas,\,i}$ is ith measurement in a bin, $X^{error}_{gas,\,i}$ is the precision of i^{th} measurement in the bin and $\overline{X}_{gas}$ is the bin average.

The datasets of X_{CO_2} and X_{CH_4} measured by EM27/SUN and both TCCON sites are presented in Fig.VII.6. X_{CO_2} measured by EM27/SUN is significantly smaller than both TCCON sites and significantly bigger for X_{CH_4}. This difference is caused by the difference in spectral resolutions (EM27/SUN and TCCON have different averaging kernels, see Section VII.3.2), and is probably caused by a non ideal optical alignment of EM27/SUN. Non optimal alignments lead to an instrumental line shape (ILS) different from the ideal one (which is a sinc function for boxcar apodization). GFIT assumes the ideal ILS for spectra fitting. If the ILS is far from an ideal, this leads to errors in column retrievals. Unfortunately, we have no information about the ILS of the EM27/SUN instrument and further we assume that the effect of non-ideal ILS is a systematic bias for all six days of measurements.

The correlation between EM27/SUN and TCCON data are presented in Fig.VII.7. The data points are fitted by a line through the origin of the coordinate system (0, 0). By regarding a slope of the fitted line we determine a bias, for example if the slope is 0.99 then the bias is $(0.9969 - 1) \times 100\% = -0.31\%$. The EM27/SUN bias in X_{CO_2} with respect to TCCON-Orleans is -0.31% (∼1.25 ppm) and -0.52% (∼2.1 ppm) with respect to TCCON-Paris. For X_{CH_4} the bias is +0.78% (∼14.4 ppb) for Orleans and +0.74% (∼13.7 ppb) for Paris site.

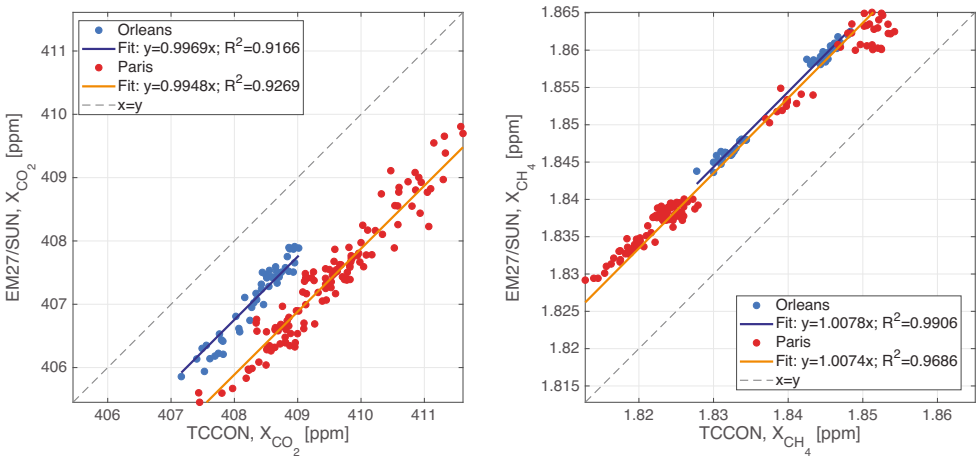

Figure VII.7 – X_{CO_2} (left) and X_{CH_4} (right) correlations plots between EM27/SUN and TCCON-Paris (red) and TCCON-Orleans(blue).

b) Scaled data

The TCCON-Orleans is validated to WMO scale by aircraft in situ measurement campaigns over the site while the TCCON-Paris is not. We can therefore use the TCCON-Orleans data as a reference. In order to calibrate EM27/SUN measurements, X_{gas} should be biased by the coefficients determined above: EM27/SUN X_{CO_2} is biased by +0.31% (scaling by 1.0031) and X_{CH_4} by -0.78% (scaling by 0.9922). This EM27/SUN data is called calibrated.

Comparing the calibrated EM27/SUN data with TCCON-Paris data we found a bias of -0.21% for X_{CO_2} and -0.04 for % X_{CH_4}. Then the Paris data is biased to the calibrated EM27/SUN data: X_{CO_2} is shifted by +0.21% and X_{CH_4} by +0.04%. The calibrated EM27/SUN and biased TCCON-Paris data are presented on Fig.VII.8.

Now, the calibrated EM27/SUN data is in a good agreement with TCCON measurements from both sites. Correlation coefficients for X_{CO_2} are 0.9166 for Orleans and 0.9269 for Paris; for X_{CH_4} they are 0.9906 and 0.9686 for Orleans and Paris respectively.

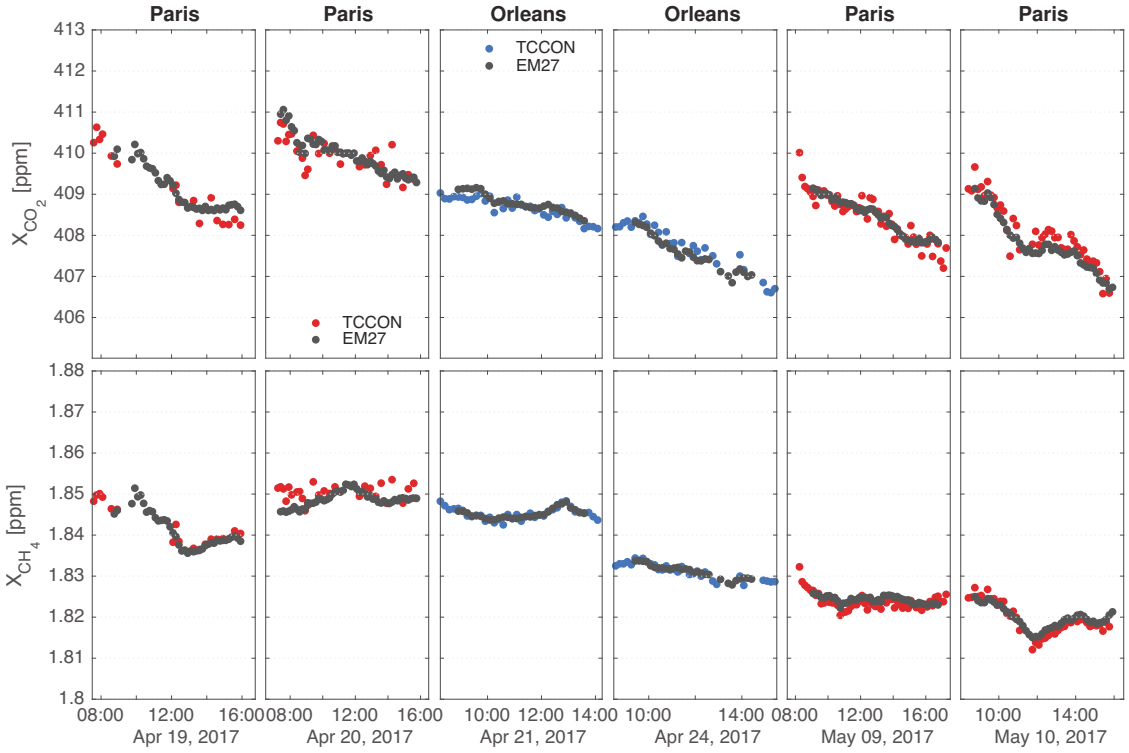

Figure VII.8 – X_{CO_2} (top panel) and X_{CH_4} (bottom panel) measured by calibrated EM27/SUN (black points), biased TCCON-Paris (red points) and standard TCCON-Orleans (blue points).

VII.2.3 Comparison of TCCON-Orleans and TCCON-Paris

The TCCON-Paris instrument is located in the city center of Paris with significant anthropogenic sources of CO_2. The TCCON-Orleans site is located at ∼100 km south of Paris in not polluted forest area. Such proximity of two TCCON sites with different pollution conditions is unique in Europe.

In this section, we compare X_{CO_2} and X_{CH_4} measured at TCCON-Orleans and Paris sites. For the Paris site we use two X_{CO_2} datasets: 1) X_{CO_2} calculated by the use of standard a priori profiles and biased by -0.21% derived from the comparison with EM27/SUN as described above; 2) X_{CO_2} calculated by the use of modified a priori profiles based on the combination of CO_2 in situ measurements and Planetary Boundary Layer height statistical model, see Section VI.4, also biased by -0.21%.

X_{CO_2} standard a priori

The comparison of X_{CO_2} for two TCCON sites is presented on the top panel of Fig.VII.9. The Paris X_{CO_2} has been biased by -0.21%. The X_{CO_2} bias between Paris and Orleans sites is +0.16% (∼0.65 ppm), and the correlation coefficient for the two data sets is 0.9252. The obtained bias is above the TCCON X_{CO_2} precision measurements of ∼0.1%. If the X_{CO_2}

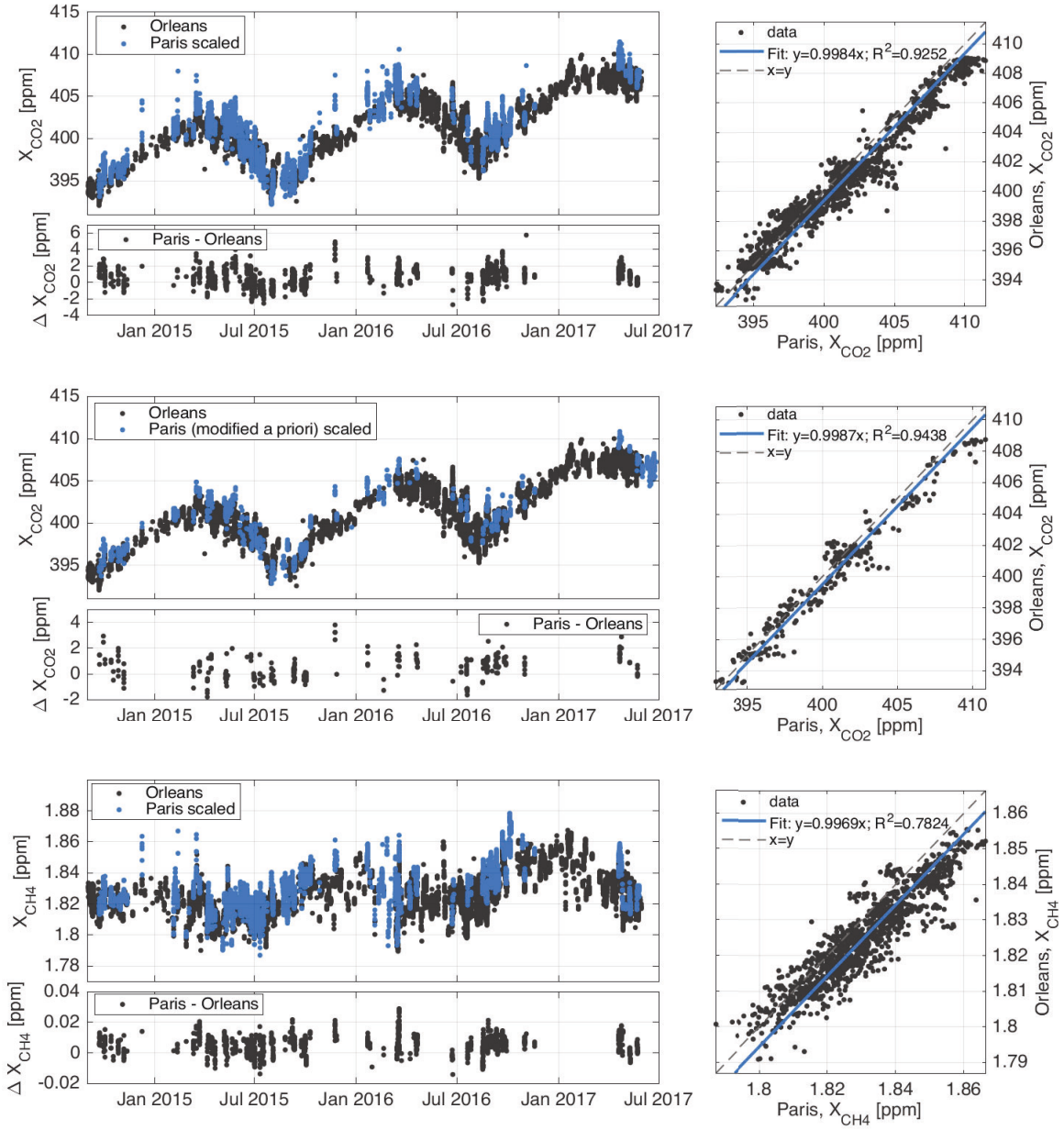

Figure VII.9 – Comparison of two TCCON sites: Orleans and Paris. Top panels: comparison of scaled Paris X_{CO_2} with Orleans. Middle panels: comparison of scaled Paris X_{CO_2} calculated by the use of modified CO_2 a priori profiles with Orleans. Botton panels: comparison of scaled Paris X_{CH_4} with Orleans.

bias of -0.21% determined by EM27/SUN instrument is correct then the origin of the bias between two TCCON sites could be attributed to the local sources of CO_2 in the Paris region.

For not biased X_{CO_2} Paris data this bias would increase to 0.37% (∼1.5 ppm). The X_{CO_2} scale factor for the TCCON-Paris data has been determined during the spring and could differ for other seasons, because GGG CO_2 a priori profiles are not well adopted for the Paris conditions and requires additional comparisons during other seasons.

X_{CO_2} modified a priori

In Chapter VI the improved set of CO_2 a priori profiles has been implemented and a new X_{CO_2} data set has been obtained. The new X_{CO_2} dataset has been calculated using the spectra measured between 11:00 and 13:00 (UTC) (see Section VI.4) resulting in fewer data points. Apart of the pollution episodes, the effect of modified CO_2 a priori profiles is to reduce the annual variation of X_{CO_2} by ∼0.75 ppm.

For the two days of EM27/SUN measurements in Paris: April 19 and May 9, the in situ CO_2 data are available. On April 19 the noon averaged mixing ration of CO_2 is 418 ppm while GGG CO_2 a priori profile provides 416.3 ppm at the ground. On 9 May measured CO_2 is 415 ppm and GGG CO_2 a priori gives 409 ppm. The difference in X_{CO_2} obtained with standard and modified a priori profiles is negligibly small both for TCCON ($\Delta X_{CO_2} = 0.05$ ppm) and for EM27/SUN ($\Delta X_{CO_2} = 0.04$ ppm). Thus, we use the same bias correction for Paris X_{CO_2} calculated using modified CO_2 a priori profiles, which is -0.21%.

The comparison of X_{CO_2} is presented on the middle panel of Fig.VII.9. A bias of +0.13% (∼0.52 ppm) between two TCCON sites has been determined which is smaller then for the case of standard CO_2 a priori profiles. The correlation coefficient between two data sets has also been improved to 0.9438.

Comparison of X_{CH_4}

The comparison of X_{CH_4} for two sites is shown on the bottom panel of Fig.VII.9. The bias of +0.31% (∼6 ppb) has been determined. The correlation coefficient is 0.7824. The bias of 0.31% is close to the precision of X_{CH_4} measurements which is ∼0.5%.

VII.3 Comparison of EM27/SUN with TCCON-Paris in Spring 2018

This short campaign includes only four days of collocated measurements of EM27/SUN and TCCON-Paris: 4, 7, 8 and 11 May, 2018. The EM27/SUN instrument was taken on lease from Le Laboratoire des Sciences du Climat et de l'Environnement (LSCE). The EM27/SUN measurements in Paris are similar to the campaign in 2017, Section VII.2.1. The EM27/SUN spectra are analyzed using the pressure dataset measured by the TCCON pressure sensor. TCCON-Paris was operating in two modes: standard high resolution (0.02 cm^{-1}) measurements (denoted TCCON HR) and "EM27/SUN like" measurements (denoted TCCON LR). TCCON LR records double-sided interferograms with the maximum optical path difference of 1.8 cm, which corresponds to the resolution of 0.5 cm^{-1} which is equal to the resolution of EM27/SUN.

For TCCON HR and LR spectra a standard phase correction threshold 0.02 was applied (see SectionV.5 for the phase correction problem of TCCON-Paris spectra). All of the spectra with identified phase correction problem have been removed.

VII.3.1 Comparison of X_{CO_2} and X_{CH_4}

X_{CO_2} and X_{CH_4} calculated for four days of collocated measurements are presented in Fig.VII.10 and the correlations are presented in Fig.VII.11.

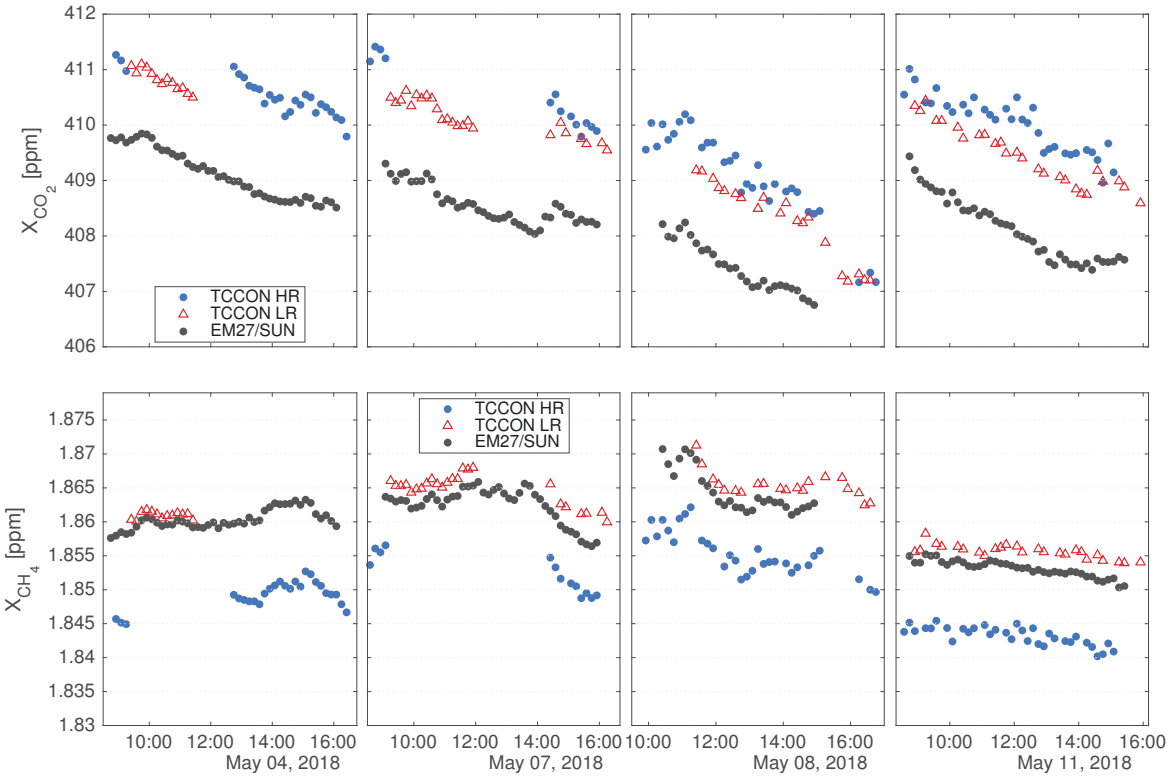

Figure VII.10 – Comparison of X_{CO_2} (top panel) and X_{CH_4} (bottom panel) measured by EM27/SUN (black points), TCCON HR (blue points) and TCCON LR (red triangles) at the Paris site.

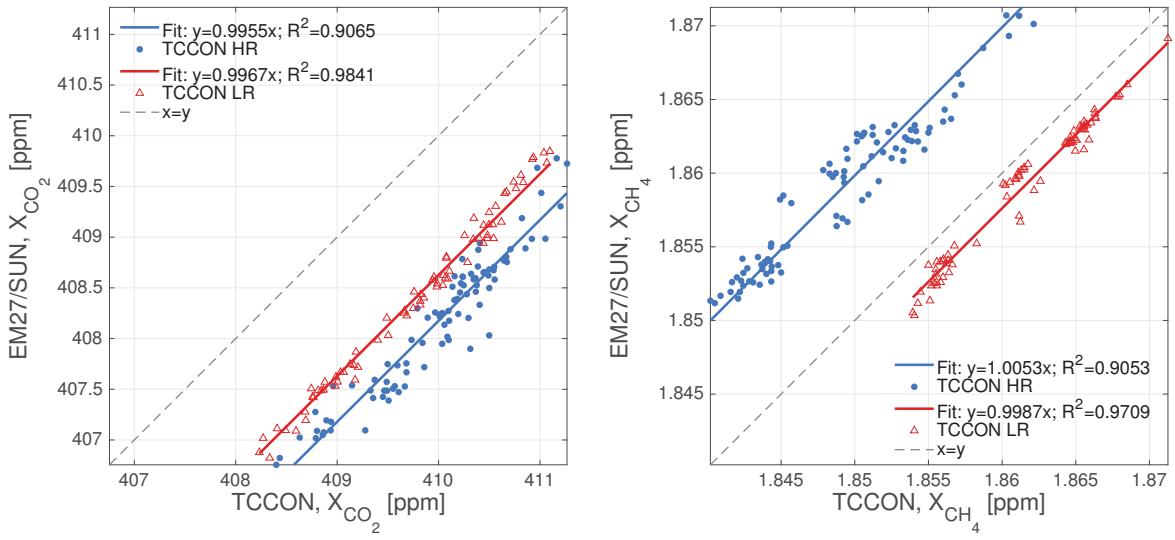

Figure VII.11 – X_{CO_2} (left) and X_{CH_4} (right) correlation plots between EM27/SUN and TCCON LR (red) and TCCON HR (blue).

As in 2017, EM27/SUN has X_{CO_2} lower than the TCCON HR and bigger for X_{CH_4}. In order to compare the biases in 2017 and 2018 between TCCON HR and EM27/SUN, we have reanalysed the EM27/SUN spectra measured in 2017 using the TCCON-Paris pressure sensor data. Biases between EM27/SUN and TCCON HR in 2017 and 2018, and TCCON LR in 2018 are presented in table VII.3. Biases in 2017 are bigger than in 2018, which is probably due to the difference in two EM27/SUN instruments (for example optical alignment). EM27/SUN has smaller but not zero biases to TCCON LR.

Table VII.3 – Biases between EM27/SUN and TCCON-Paris for two molecules CO_2 and CH_4.

	X_{CO_2}	X_{CH_4}
TCCON HR, 2017	-0.50% (∼2.0 ppm)	+0.79% (∼14.6 ppb)
TCCON HR, 2018	-0.45% (∼1.8 ppm)	+0.53% (∼9.8 ppb)
TCCON LR, 2018	-0.33% (∼1.3 ppm)	-0.13% (∼2.4 ppb)

In order to understand the origin of the biases, we compare the averaging kernels and total columns for each type of measurements in the next section.

VII.3.2 Comparison of total columns of CO_2, CH_4 and O_2 and their averaging kernels

To calculate column-averaged dry-air mole fractions, the total column of the gas is divided by the total column of the dry air, which is equal to the total column of gas divided by an assumed dry-air mole fraction of O_2 (0.2095). In this section we investigate which total column contributes the most to the biases and compare column averaging kernels.

Comparison of the total columns for each gas (CO_2, CH_4 and O_2) are presented in Fig.VII.12 and summarised in TableVII.4. Comparison of the column averaging kernels is

presented in Fig.VII.13.

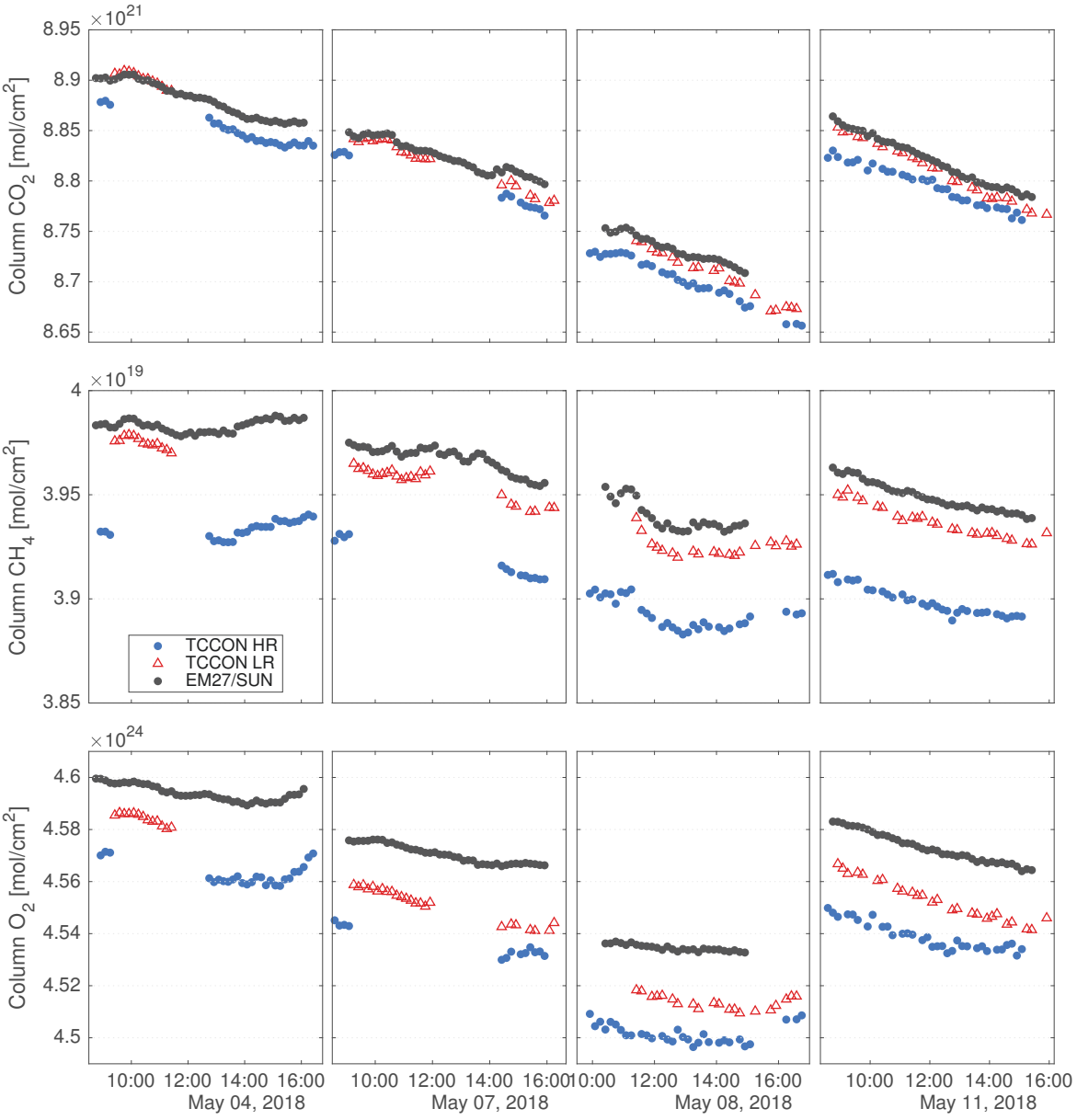

Figure VII.12 – Comparison of total column calculated by EM27/SUN, TCCON HR and TCCON LR.

Table VII.4 – X_{gas} and total column biases between EM27/SUN and TCCON HR and LR.

	X_{CO_2}	X_{CH_4}	col_{CO_2}	col_{CH_4}	col_{O_2}
TCCON HR	-0.45%	+0.53%	+0.28%	+1.76%	+0.71%
TCCON LR	-0.33%	-0.13%	+0.07%	+0.28%	+0.41%

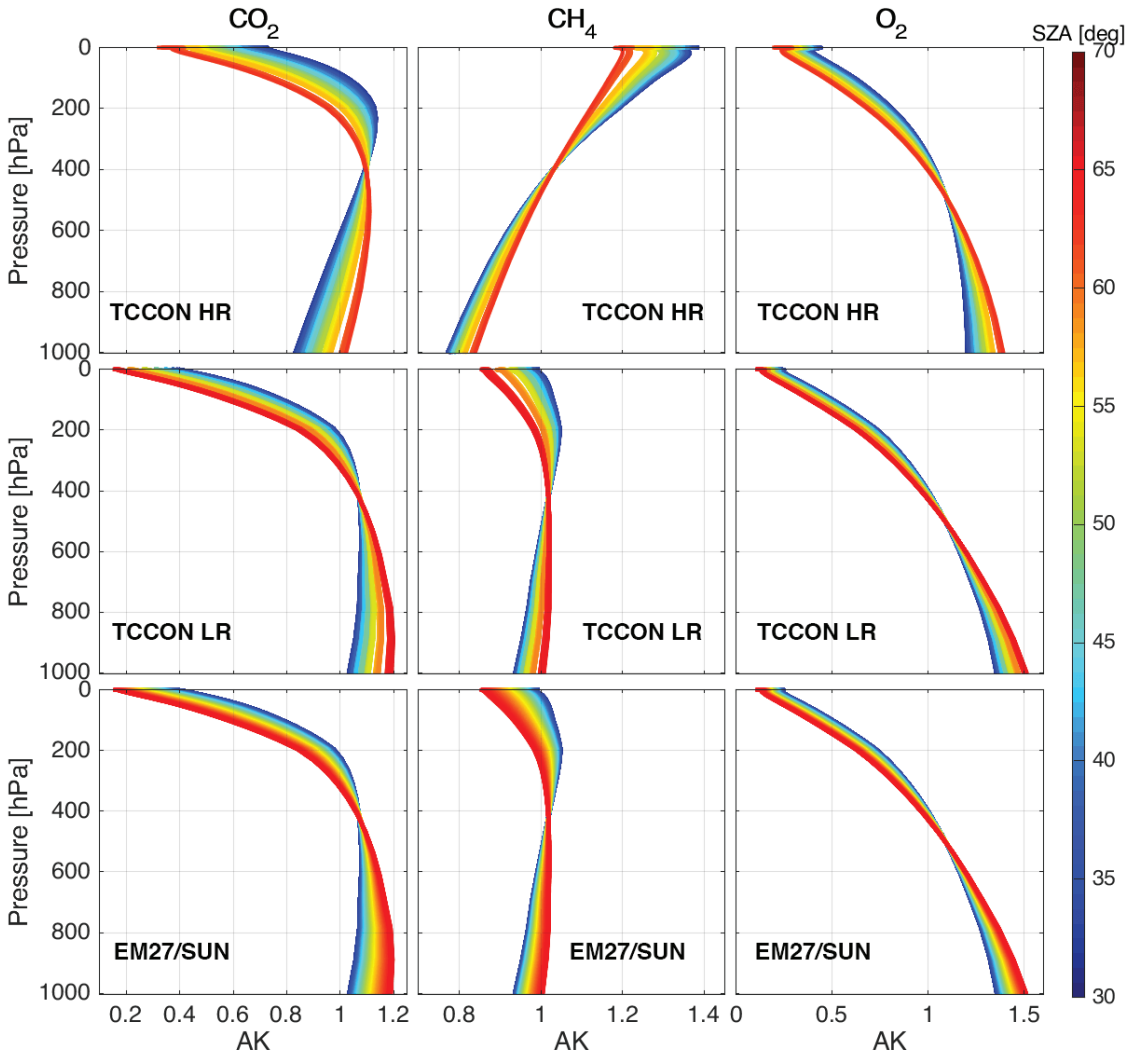

Figure VII.13 – The comparison of averaging kernels calculated for CO_2, CH_4 and O_2, for TCCON HR (three top panels), TCCON LR (three middle panels) and EM27/SUN.

Comparison of total columns measured by EM27/SUN and TCCON LR

The bias in CO_2 total columns between EM27/SUN and TCCON LR is relatively small: +0.07%, but for the total column of O_2 the bias is 0.41% which is the main contributor to the X_{CO_2} bias of -0.33%. The bias in columns of CH_4 is +0.28% and comparable with the bias in O_2 column. As a result of division of gas and O_2 columns the biases are partially compensated which leads to the smaller bias in the resulting X_{gas}. The columns averaging kernels of EM27/SUN are identical to TCCON LR for all three gases, which does not explain the source of the biases between EM27/SUN and TCCON LR. The source of this bias is probably due to the difference in instruments, for example in the ILS.

Comparison of total columns measured by EM27/SUN and TCCON HR

For the case of the TCCON HR measurements, there is significant difference in the column averaging kernels between TCCON HR and EM27/SUN (identical to TCCON LR). The difference in column averaging kernels explains the biases in total columns between TCCON HR and TCCON LR, through the equation given by [68]:

$$\hat{c}_{\mathrm{HR}} - \hat{c}_{\mathrm{LR}} = (\mathbf{a}_{\mathrm{HR}} - \mathbf{a}_{\mathrm{LR}})(\mathbf{x} - \mathbf{x_a})$$

where $\hat{c}_{\mathrm{HR}}$ and $\hat{c}_{\mathrm{LR}}$ are the total columns of the gas measured by TCCON HR and TCCON LR instruments correspondingly, $\mathbf{a}_{\mathrm{HR}}$ and $\mathbf{a}_{\mathrm{LR}}$ are corresponding column averaging kernels, $\mathbf{x_a}$ is the a priori vertical mixing ratio profile of the gas and $\mathbf{x}$ is the true vertical mixing ratio profile of the gas.

The EM27/SUN measurements are therefore not directly comparable to TCCON HR, since there are two origins of biases. The first one is the difference in column averaging kernels due to the difference in spectral resolutions. The second one is the difference in instruments most probably due to the difference in instrumental line shapes, which could be different from one EM27/SUN instrument to another.

Summary and Outlook

The objective of this PhD work was to study and characterise the performance of the TCCON-Paris station as well as to investigate alternative solutions to the standard WMO calibration procedures for this particular site, which is the only European TCCON station located in the centre of a megacity. As such, TCCON-Paris is an interesting target for the validation of current (OCO-2, GOSAT, TROPOMI) and future (GOSAT-2, OCO-3, MicroCarb) satellite missions. This will, in particular, test the satellites ability to detect and measure CO_2 gradients due to strong local anthropogenic emission sources of greenhouse gases and air pollutants associated with a megacity.

The instrument has been maintained and characterised over the whole three years period of the thesis. This included monitoring of its instrumental line shape as an essential indicator of the instrument proper functioning and stability. These tests have been performed on a monthly basis using low-pressure HCl gas cell measurements. Once in the three years period, an optical realignment became necessary. In order to facilitate this relatively complex and potentially error-prone procedure, I have developed a new setup for the observation of Haidinger fringes using a CCD camera. The Haidinger fringes criterium is one of the alignment criteria used in the TCCON network. Contrary to fringe observation using an external telescope, the new method does not modify the standard optical path. Instead of removing a mirror from the existing optics it temporarily inserts an additional mirror, which is a more reliable procedure. Another advantage of the proposed method is that in principle it also works under vacuum conditions if the CCD camera is permanently installed inside the spectrometer. Implementing this solution network-wide could improve on the reliability of the network data by resolving issues that arrive from aligning the optics under conditions that are different from the operational.

The stability of the FTS-Paris instrument has been investigated using the Allan variance approach to determine the optimum operating conditions for gas cell measurements. Using measurements acquired during an international blind intercomparison of N_2O gas columns in low-pressure cells, the optimal averaging time of one spectrum has been determined to be 6 hours. The detailed analysis of measurements at Peterhof (St. Petersburg, Russia), Karlsruhe (Germany) and Paris has revealed that an originally unexplained bias between Paris and Karlsruhe of about 1% was due to an error in the reference data. When properly accounted for, the agreement between Paris and Karlsruhe measurements is within 0.26%, which is close to instrumental limitations. These results which demonstrate the well-functioning of the Paris instrument will be published by the intercomparison organisers (PI F. Hase, Karlsruhe), once the data from the other partner sites have undergone a similar thorough reanalysis.

Besides the hardware, the TCCON analysis software (GGG) has been investigated thoroughly in order to guarantee good quality data. In these investigations, discrepancies between forward and backward spectra were detected after the update of the solar tracker early in 2018. These discrepancies are due to a malfunctioning of the phase correction algorithm which is linked to a threshold parameter. Changing the network default value of 0.02 to 0.001 removes this discrepancy, but introduces a bias of $\sim$0.4% in the resulting CO_2 columns. The erroneous phase correction has been communicated to the developers of GGG (PI G. Toon, JPL) and will be taken into account in the next release of the analysis software.

The most central question of this thesis is how the very variable and relatively high ground concentrations of carbon dioxide due to nearby sources impact on the retrieval results. The ground level volume mixing ratios of CO_2 a priori profiles sometimes differ by more than 50 ppm from the mixing ratios obtained by in situ measurements. Using the onsite in-situ CO_2 measurements (PI I. Xueref-Rémy, Marseille) and LIDAR soundings of the boundary layer height (PI F. Ravetta, Paris), we constructed a set of improved a priori profiles that comply with local ground conditions. These new a priori profiles were incorporated into GGG for studying the impact on the retrieved dry air mole fraction of CO_2 (X_{CO_2}). Analyzing the data of the last three years, a significant bias of up to 0.88 ppm during summer periods has been found. This value is high enough to affect the validation of satellite missions, especially the on-going validation of the OCO-2 satellite. These results have been presented at the annual joint NDACC-IRWG & TCCON 2018 meeting at Cocoyoc (Mexico). It was suggested to take these local particularities into account either by providing more realistic a priori profiles for urban sites or by giving the possibility that GGG a priori profiles can be easily modified. In my opinion, the best solution would be to allow for both possibilities in future releases of GGG.

In the frame of linking TCCON-Paris to the international CO_2 scale provided by WMO, two intercomparison campaigns with mobile low-resolution instruments (EM27/SUN) have been undertaken. In the first campaign, a mobile instrument was used as a transferable reference between the TCCON-Orleans and TCCON-Paris sites. The instrument was calibrated at the TCCON-Orleans site and then used as a reference for the TCCON-Paris measurements, revealing a possible bias of +0.21% in X_{CO_2} between Paris and Orleans. In the second campaign, the difference between EM27/SUN and TCCON-Paris carbon dioxide columns is investigated. A bias of about 0.45% has been found. In principle, two different biases are possible: one caused by the difference in column averaging kernels due to the spectral resolution being different between the stationary and the mobile instruments. This could explain a bias of about 0.12%. Another one due to other instrumental differences, most likely due to the different instrumental line shapes. A better understanding of the differences and similarities between high and low resolution instruments and further investigations will help in making the link to the WMO scale, especially in environments where overflights with calibrated in-situ instruments are forbidden or logistically impossible. Intercomparisons under varying seasonal conditions will be particularly useful in this respect, especially if such studies are done during pollution episodes in Paris. Then, differences in instrumental sensitivities with respect to local pollutions could be determined. Based on an improved understanding of these fine instrumental effects, a calibration of TCCON stations using mobile low resolution instruments seems to be conceivable on a longer-term scale.

Acknowledgement

The present thesis has been written at the Laboratoire d'Etudes du Rayonnement et de la Matière en Astrophysique et Atmosphères (LERMA) at Sorbonne Université. I am grateful to the Région Île-de-France who has provided the funds for my thesis position.

Most importantly, I would like to thank my thesis director Christof Janssen and co-director Yao Té, who welcomed me in their team at LERMA. They were always ready to assist and encourage me, especially during times when I got lost (in my research). As a member of the SMILE research group, I have enjoyed the opportunity to work on exciting projects and participating in conferences throughout the world. In addition to Christof and Yao, I am also grateful to my thesis committee members, Pascale Chelin and Mathieu Bertin for keeping my thesis on track and aimed towards completion.

I am especially thankful to Pascal Jeseck for the enormous amount of time and energy he has invested in teaching me about the FTS Bruker 125HR instrument and the GGG package. He has also been an invaluable help in the battle with the French bureaucracy system.

I further owe thanks to Irène Xueref-Remy and François Ravetta for their open collaboration and contributing to my work by providing and explaining the CO_2 in situ (Irène) and PBL height (François) data and for the discussion of the obtained results in my work. I further want to thank Michel Ramonet and Morgan Lopez for providing an EM27/SUN instrument for the short measurement campaigns and for their assistance in measurements at the TCCON-Orleans site. Special thanks are also due to Frank Hase and Maria Makarova for their collaboration in the N_2O intercomparison blind test. I am also very grateful to Debra Wunch, Geoffrey Toon and Dietrich Feist for their open discussions of my study and for assistance with GGG.

Many thanks are due to all of the LERMA staff: Christian Rouillé for maintaining the electronics of the solar tracking, Patrick Marie-Jeanne for building cell supports, Nora Roger for the help with administrative issues, Corinne Boursier, Thomas Zanon, Hadj Elandaloussi, and all LERMA scientists, administrative and computer support staff, as well as the direction of the laboratory.

I would further like to acknowledge my thesis reviewers and the members of jury: Maud Rotger, Thorsten Warneke, Michel Ramonet, Martine De Mazière and Laurence Picon.

I could not have written the thesis without the support of all my friends: Antont Malmygin, Arthur Minakhmetov, Alex Tikan, Asya Shakhmametova, Giorgio Maltese, Ivan Prokofiev, Ksenia Nagonova, Levon Lastname, Marina Ivanicenko, Marina Smirnova, Natalia Butinova and Sergey Dmitriev for their support and making my stay here colourful. Finally, I thank my family and my girlfriend Maria Drobyshevskaia for their love and support.

Bibliography

[1] lecture in ERCA winter school F., Cordon: Fundamentals of atmospheric dynamics, 2017. 1, 123

[2] Ipcc: Climate change 2007: Synthesis report. a contribution of working groups i, ii and iii to the fourth assessment report of the intergovernmental panel on climate change. *IPCC, Geneva,*, 2007. 3, 4, 5, 123

[3] G. A. Schmidt, R. A. Ruedy, R. L. Miller, and A. A. Lacis. Attribution of the present-day total greenhouse effect,. *Journal of Geophysical Research: Atmospheres*, 115:D20106, 2010. doi: 10.1029/2010JD014287. 4, 5

[4] Ipcc: Climate change 2001: Synthesis report. a contribution of working groups i, ii and iii to the third assessment report of the intergovernmental panel on climate change. *Cambridge University Press*, 2001. 4

[5] Le Quéré C., Raupach M., R., Canadell J., G., Marland G., Bopp L., Ciais P., Conway T., J., Doney S., C., Feely R., A., Foster P., Friedlingstein P., Gurney K., Houghton R., A., House J., I., Huntingford C., Levy P., E., Lomas M., R., Majkut J., Metzl N., Ometto J., P., Peters G., P., Prentice I., C., Randerson J., T., Running S., W., Sarmiento J., L., Schuster U., Sitch S., Takahashi T., Viovy N., van der Werf G., R., and Woodward F., I. Trends in the sources and sinks of carbon dioxide. *Nature Geoscience*, 2:831–836, 2009. doi: 10.1038/ngeo689. 6, 7

[6] D. Wunch, G. C. Toon, J.-F. L. Blavier, R. A. Washenfelder, J. Notholt, B. J. Connor, D. W. T. Griffith, V. Sherlock, and P. O. Wennberg. The total carbon column observing network. *Philosophical Transactions of the Royal Society A: Mathematical, Physical and Engineering Sciences*, 369:2087–2112, 2011. doi: 10.1098/rsta.2010.0240. URL http://rsta.royalsocietypublishing.org/content/369/1943/2087.abstract. 7, 44, 46, 47, 57, 93, 125

[7] Sussmann R., Forster F., Rettinger M., and Bousquet P. Renewed methane increase for five years (2007-2011) observed by solar ftir spectrometry. *Atmospheric Chemistry and Physics*, 12(11):4885, 2012. doi: 10.5194/acp-12-4885-2012. 7

[8] Keppel-Aleks G., Wennberg P., O., and Schneider T. Sources of variations in total column carbon dioxide. *Atmospheric Chemistry and Physics*, 11(8):3581–3593, 2011. doi: 10.5194/acp-11-3581-2011.

[9] Keppel-Aleks G., Wennberg P., O., Washenfelder R., A., Wunch D., Schneider T., Toon G., C., Andres R., J., Blavier J.-F., Connor B., Davis K., J., Desai A., R., Messerschmidt J., Notholt J., Roehl C., M., Sherlock V., Stephens B., B., Vay1 S., A., and Wofsy S., C. The imprint of surface uxes and transport on variations in total column carbon dioxide. *Biogeosciences*, 9(3):875–891, 2012. doi: 10.5194/bg-9-875-2012.

[10] Chevallier F., Deutscher N., M., Conway T., J., Ciais P., Ciattaglia L., Dohe S., Frohlich M., Gomez-Pelaez A., J., Griffith D., Hase F., Haszpra L., Krummel P., Kyro E., Labuschagne C., Langenfelds R., Machida T., Maignan F., Matsueda H., Morino I., Notholt J., Ramonet M., Sawa Y., Schmidt M., Sherlock V., Steele P., Strong K., Sussmann R., Wennberg P., Wofsy S., Worthy D., Wunch D., and Zimnoch M. Global co2 fluxes inferred from surface air-sample measurements and from tccon retrievals of the co2 total column. *Geophysical Research Letters*, 38(24):1–5, 2011. doi: 10.1029/2011GL049899.

[11] Guerlet S., Basu S., Butz A., Krol M., Hahne P., Houweling S., Hasekamp O., P., and Aben I. Reduced carbon uptake during the 2010 northern hemisphere summer from gosat. *Geophysical Research Letters*, 40:2378–2383, 2013. doi: 10.1002/grl.50402.

[12] Wunch D., Wennberg P., O., Messerschmidt J., Parazoo N., C., Toon G., C., Deutscher N., M., Keppel-Aleks G., Roehl C., M., Randerson J., T., Warneke T., and Notholt J. The covariation of northern hemisphere summertime co2 with surface temperature in boreal regions. *Atmospheric Chemistry and Physics*, 13(18):9447–9459, 2013. doi: 10.5194/acp-13-9447-2013.

[13] Deutscher N., M., Sherlock3 V., Mikaloff Fletcher S., E., T. Griffith D., W., Notholt J., Macatangay R., Connor B., J., Robinson J., Shiona H., Velazco V., A., Wang Y., Wennberg P., O., and Wunch D. Drivers of column-average co2 variability at southern hemispheric total carbon column observing network sites. *Atmospheric Chemistry and Physics*, 14:9883–9901, 2014. doi: 10.5194/acp-14-9883-2014. 7

[14] Wunch et al. D. Comparisons of the orbiting carbon observatory-2 (oco-2) xco2 measurements with tccon. *Atmospheric Measurement Techniques*, 10:2209–2238, 2017. doi: 10.5194/amt-10-2209-2017. 7, 90

[15] Morino I., Uchino O., Inoue M., Yoshida Y., Yokota T., Wennberg P., O., Toon G., C., Wunch D., Roehl C., M., Notholt J., Warneke T., Messerschmidt J., T. Griffith D., W., Deutscher N., M., Sherlock V., Connor B., Robinson J., Sussmann R., and Rettinger M. Preliminary validation of column-averaged volume mixing ratios of carbon dioxide and methane retrieved from gosat short-wavelength infrared spectra. *Atmospheric Measurement Techniques*, 4(6):1061–1076, 2011. doi: 10.5194/amt-4-1061-2011.

[16] Wunch D., Wennberg P., O., Toon G., C., Connor B., J., Fisher B., Osterman G., B., Frankenberg C., Mandrake L., O'Dell C., Ahonen P., Biraud S., C., Castano R., Cressie N., Crisp D., Deutscher N., M., Eldering A., Fisher M., L., T. Griffith D., W., Gunson M., Heikkinen P., Keppel-Aleks G., Kyro E., Lindenmaier R., Macatangay R., Mendonca J., Messerschmidt J., Miller C., E., Morino I., Notholt J., Oyafuso F., A., Rettinger M., Robinson J., Roehl C., M., Salawitch R., J., Sherlock V., Strong K.,

Sussmann R., Tanaka T., Thompson D., R., Uchino O., Warneke T., and Wofsy S., C. A method for evaluating bias in global measurements of co2 total columns from space. *Atmospheric Chemistry and Physics*, 11(23):12317–12337, 2011. doi: 10.5194/acp-11-12317-2011.

[17] Butz A., Guerlet S., Hasekamp O., Schepers D., Galli A., Aben I., Frankenberg C., Hartmann J.-M., Tran H., Kuze A., Keppel-Aleks G., Toon G., Wunch D., Wennberg P., Deutscher N., Griffith D., Macatangay R., Messerschmidt J., Notholt J., and Warneke T. Toward accurate co2 and ch4 observations from gosat. *Geophysical Research Letters*, 38(14):2–7, 2011. doi: 10.1029/2011GL047888.

[18] Schneising O., Bergamaschi P., Bovensmann H., Buchwitz M., Burrows J., P., Deutscher N., M., T. Griffith D., W., Heymann J., Macatangay R., Messerschmidt J., Notholt J., Rettinger M., Reuter M., Sussmann R., Velazco V., A., Warneke T., Wennberg P., O., and Wunch D. Atmospheric greenhouse gases retrieved from sciamachy: comparison to ground-based fts measurements and model results. *Atmospheric Chemistry and Physics*, 12(3):1527–1540, 2012. doi: 10.5194/acp-12-1527-2012.

[19] Schepers D., Guerlet S., Butz A., Landgraf J., Frankenberg C., Hasekamp O., Blavier J.-F., Deutscher N., M., T. Griffith D., W., Hase F., Kyro E., Morino I., Scherlock V., Sussmann R., and A. Aben E., A. Methane retrievals from greenhouse gases observing satellite (gosat) shortwave infrared measurements: Performance comparison of proxy and physics retrieval algorithms. *Journal of Geophysical Research*, 117(D10):1–14, 2012. doi: 10.1029/2012JD017549.

[20] Reuter M., Bosch H., Bovensmann H., Bril A., Buchwitz M., Butz A., Burrows J., P., O'Dell C., W., Guerlet S., Hasekamp O., Heymann J., Kikuchi N., Oshchepkov S., Parker R., Pfeifer S., Schneising O., Yokota T., and Yoshida Y. A joint effort to deliver satellite retrieved atmospheric co2 concentrations for surface ux inversions: the ensemble median algorithm emma. *Atmospheric Chemistry and Physics*, 13(4):1771–1780, 2013. doi: 10.5194/acp-13-1771-2013. 7

[21] Peter R. Griffiths, James A. De Haseth, and James D. Winefordner. *Fourier Transform Infrared Spectrometry, 2nd Edition*. 2007. 9, 12, 13, 33, 123

[22] M. Gisi, F. Hase, S. Dohe, and T. Blumenstock. Camtracker: a new camera controlled high precision solar tracker system for ftir-spectrometers. *Atmospheric Measurement techniques*, 4:47–54, 2011. doi: 10.5194/amt-4-47-2011. 18, 19, 123

[23] Hase F., Blumenstock T., and C. Paton-Walsh. Analysis of the instrumental line shape of high-resolution fourier transform ir spectrometers with gas cell measurements and new retrieval software. *Applied Optics*, 38:3417–3422, 1999. doi: 10.1364/AO.38.003417. 20, 27

[24] F. Hase. Improved instrumental line shape monitoring for the ground-based, high-resolution ftir spectrometers of the network for the detection of atmospheric composition change. *Atmospheric Measurement Techniques*, 5:603–610, 2012. doi: 10.5194/amt-5-603-2012. URL www.atmos-meas-tech.net/5/603/2012/. 20, 25, 27

[25] Sun Y., Palm M., Liu C., Hase F., Griffith D., Weinzierl C., Petri C., Wang W., and Notholt J. The influence of instrumental line shape degradation on ndacc gas retrievals: total column and profile. *Atmospheric Measurement Techniques*, 11:2879–2896, 2018. doi: 10.5194/amt-11-2879-2018. 23, 124

[26] J. W. Hannigan. Ndacc irwg: Evolution of ground-based global trace gas infrared remote sensing. *Imaging and Applied Optics, Optical Society of America*, 2011. doi: 10.1364/FTS.2011.FMC1. URL https://www.osapublishing.org/abstract.cfm?uri=FTS-2011-FMC1. 25, 93

[27] Hase F. Ndacc-irwg cell exercise: status and further steps, 2017. 27, 124

[28] Werle P., Mucke R., and Slemr F. The limits of signal averaging in atmospheric trace-gas monitoring by tunable diode-laser absorption spectroscopy (tdlas). *Applied Physics B*, 57:131–139, 1993. doi: 10.1007/BF00425997. 31

[29] C.D. Rodgeres. *Inverse Methods for Atmospheric Sounding: Theory and Practice*. 2000. 36, 43

[30] D. Wunch, G. C. Toon, V. Sherlock, N. M. Deutscher, X. Liu, D. G. Feist, and P. O. Wennberg. The total carbon column observing network's ggg2014 data version. 2015. doi: 10.14291/tccon.ggg2014.documentation.R0/1221662. 37, 45, 55, 95, 125

[31] G. Keppel-Aleks, G. C. Toon, P. O. Wennberg, and N. M. Deutscher. Reducing the impact of source brightness fluctuations on spectra obtained by fourier-transform spectrometry. *Applied Optics*, 46(21):4774–4779, 2007. doi: 10.1364/AO.46.004774. 37

[32] Kalnay E., Kanamitsu M., Kistler R., Collins W., Deaven D., Gandin L., Iredell M., Saha S., White G., Woollen J., Zhua Y., Chelliah M., Ebisuzaki W., Higgins W., Janowiak J., Mo K., C., Ropelewski C., Wang J., Leetmaa A., Reynolds R., Jenne R., and Joseph D. The ncep/ncar 40-year reanalysis project. *Bulletin of the American Meteorological Society,*, 77:437–472, 1996. doi: 10.1175/1520-0477. 38

[33] G. C. Toon. The jpl mkiv interferometer. *Optics and Photonics News*, 2(10):19. doi: 10.1364/OPN.2.10.000019. 38

[34] Karion A., Sweeney C., Tans P., and Newberger T. Aircore: An innovative atmospheric sampling system,. *Journal of Atmospheric and Oceanic Technology*, 27(11):1839–1853, 2010. doi: 10.1175/2010JTECHA1448.1. 38

[35] C. Daube Jr., B., Boering K., A., Andrews A., E., and Wofsy S., C. A high-precision fast response airborne co2 analyzer for in situ sampling from the surface to the middle stratosphere. *Journal of Atmospheric and Oceanic Technology*, 19(10):1532–1543, 2002. doi: 10.1175/1520-0426. 38

[36] S. C. Wofsy. Hiaper pole-to-pole observations (hippo):
ne-grained, global-scale measurements of climatically important atmospheric gases and aerosols. *Philosophical Transactions of the Royal Society - Series A: Mathematical, Physical and Engineering Sciences*, 369(1943):2073–2086, 2011. doi: 10.1098/rsta.2010.0313. 38

[37] Pan L., L., Bowman K., P., Atlas E., L., Wofsy S., C., Zhang F., Bresch J., F., Ridley B., A., Pittman J., V., Homeyer C., R., Romashkin P., and Cooper W., A. The stratosphere-troposphere analyses of regional transport 2008 experiment. *Bulletin of the American Meteorological Society*, 91(3):327–342, 2010. doi: 10.1175/2009BAMS2865.1. 38

[38] Singh H., B., Brune W., H., Crawford J., H., Jacob D., J., and Russell P., B. Overview of the summer 2004 intercontinental chemical transport experiment-north america (intex-a). *Journal of Geophysical Research: Atmospheres*, 111(24), 2006. doi: 10.1029/2006JD007905. 38

[39] Messerschmidt J., . Geibel M., C, Blumenstock T., Chen2 H., Deutscher N., M., Engel A., Feist D., G., Gerbig C., Gisi M., Hase F., Katrynski K., Kolle O., Lavric J., V., Notholt J., Palm M., Ramonet M., Rettinger M., Schmidt M., Sussmann R., Toon G., C., Truong F., Warneke T., Wennberg P., O., Wunch D., and Xueref-Remy I. Calibration of tccon column-averaged co2: the first aircraft campaign over european tccon sites. *Atmospheric Chemistry and Physics*, 11(21):10765–10777, 2011. doi: 10.5194/acp-11-10765-2011. URL https://www.atmos-chem-phys.net/11/10765/2011/. 38

[40] C. Geibel M. and et al. Calibration of column-averaged ch4 over european tccon fts sites with airborne in-situ measurements,. *Atmospheric Chemistry and Physics*, 12: 8763–8775, 2012. doi: 10.5194/acp-12-8763-2012. 38

[41] Bernath P., F. Atmospheric chemistry experiment (ace): Mission overview. *Geophysical Research Letters*, 32(15):1–5, 2005. doi: 10.1029/2005GL022386. 38

[42] Irion F., W. Atmospheric trace molecule spectroscopy (atmos) experiment version 3 data retrievals. *Applied Optics*, 41(33):6968, 2002. doi: 10.1364/AO.41.006968. 38

[43] Toon G., C. Solar line list for ggg2014, line list for ggg2014. *TCCON data archive, hosted by the Carbon Dioxide Information Analysis Center, Oak Ridge National Laboratory, Oak Ridge, Tennessee*, 2014. doi: 10.14291/tccon.ggg2014.solar.R0/1221658. 41

[44] Rothman et al L., S. The hitran 2008 molecular spectroscopic database. *Journal of Quantitative Spectroscopy and Radiative Transfer*, 110:533–572, 2009. doi: 10.1016/j.jqsrt.2009.02.013. 41

[45] Rothman et al. L., S. The hitran2012 molecular spectroscopic database. *Journal of Quantitative Spectroscopy and Radiative Transfer*, 130:4–50, 2013. doi: 10.1016/j.jqsrt.2013.07.002.

[46] Gordon et al. I., E. The hitran2016 molecular spectroscopic database. *Journal of Quantitative Spectroscopy and Radiative Transfer*, 203:3–69, 2017. doi: 10.1016/j.jqsrt.2017.06.038. 41

[47] Toon G., C. Telluric line list for ggg2014. *TCCON data archive, hosted by the Carbon Dioxide Information Analysis Center, Oak Ridge National Laboratory, Oak Ridge, Tennessee*, 2014. doi: 10.14291/tccon.ggg2014.atm.R0/1221656. 41

[48] Wunch et al. D. Calibration of the total carbon column observing network using aircraft pro

le data. *Atmospheric Measurement Techniques*, 3(5):1351–1362, 2010. doi: 10.5194/amt-3-1351-2010. 45

[49] Té Y., Jeseck P., Payan S., Pépin I., and Camy-Peyret C. The fourier transform spectrometer of the université pierre et marie curie qualair platform. *Review of Scientific Instruments*, 81(10):103102, 2010. doi: 10.1063/1.3488357. 49

[50] Gordon I., E., Kassi S., Campargue A., and Toon G., C. First identification of the electric quadrupole transitions of oxygen in solar and laboratory spectra, journal of quantitative spectroscopy and radiative transfer. *Journal of Quantitative Spectroscopy and Radiative Transfer*, 111:1174, 2010. doi: 10.1016/j.jqsrt.2010.01.008. 53

[51] Feist D., G., Arnold S., G., Hase F., and Ponge D. Rugged optical mirrors for fourier transform spectrometers operated in harsh environments. *Atmospheric Measurement Techniques*, 9:2381–2391, 2016. doi: 10.5194/amt-9-2381-2016. URL www.atmos-meas-tech.net/9/2381/2016/. 62

[52] Insee: La population légale de l'ile-de-france au 1er janvier 2010, no. 298, 2012. 69

[53] Xueref-Remy I., E. Dieudonné, Vuillemin C., Lopez M., Lac C., Schmidt M., Delmotte M., Chevallier F., Ravetta F., Perrussel O., Ciais P., Bréon F.-M., Broquet G., Ramonet M., Spain T., G., , and Ampe C. Diurnal, synoptic and seasonal variability of atmospheric co2 in the paris megacity area. *Atmospheric Chemistry and Physics*, 18: 3335–3362, 2018. doi: 10.5194/acp-18-3335-2018. 69, 88

[54] Klein A., Ancellet G., Ravetta F., Thomas J., L., and Pazmino A. Characterizing the seasonal cycle and vertical structure of ozone in paris, france using four years of ground based lidar measurements in the lowermost troposphere. *Atmospheric Environment*, 167:603–615, 2017. doi: 10.1016/j.atmosenv.2017.08.016. 70, 85

[55] Busch K., W. and Busch M., A. *Cavity ring-down spectroscopy: An ultratrace absorption measurement technique*. 1997. 71

[56] C. Frankenberg, R. Pollock, R. A. M. Lee, R. Rosenberg, J.-F. Blavier, D. Crisp, C. W. O'Dell, G. B. Osterman, P. O. Roehl, C.and Wennberg, and D.: Wunch. The orbiting carbon observatory (oco-2): spectrometer performance evaluation using pre-launch direct sun measurements,. *Atmos. Meas. Tech.,*, 8:301–313, 2015. doi: 10.5194/amt-8-301-2015,2015. 93

[57] Morino I., Uchino O., Inoue M., Yoshida Y., Yokota T., O. Wennberg P., C. Toon G., Wunch D., M. Roehl C., Notholt J., Warneke T., Messerschmidt J., T. Griffith D., W., M. Deutscher N., Sherlock V., Connor B., Robinson J., Sussmann R., and Rettinger M. Preliminary validation of columnaveraged volume mixing ratios of carbon dioxide and methane retrieved from gosat short-wavelength infrared spectra. *Atmospheric Measurement Techniques*, 4:1061–1076, 2011. doi: 10.5194/amt-4-1061-2011. 93

[58] Taylor T., E., O'Dell C., W., Frankenberg C., Partain P., T., Cronk H., Q., Savtchenko A., Nelson R., R., Rosenthal E., J., Chang A., Y., Fisher B., Osterman G., B., Pollock R., H., Crisp D., Eldering A., and Gunson M., R. Orbiting carbon observatory-2 (oco-2) cloud screening algorithms: validation against collocated modis and caliop data.

Atmospheric Measurement Techniques, 9:973–989, 2016. doi: 10.5194/amt-9-973-2016. 93

[59] M. Frey, M. K. Sha, F. Hase, M. Kiel, T Blumenstock, R Harig, G. Surawicz, N. M. Deutscher, K. Shiomi, J. Franklin, H Bösch, J. Chen, M. Grutter, H. Ohyama, Y. Sun, A. Butz, G. M. Tsidu, D. Ene, D Wunch, Z. Cao, O. Garcia, M. Ramonet, F. Vogel, and J. Orphal. Building the collaborative carbon column observing network (coccon): Long term stability and ensemble performance of the em27/sun fourier transform spectrometer. 93, 94

[60] F. Hase, M. Frey, T. Blumenstock, J. Grob, M. Kiel, R. Kohlhepp, G. Mengistu Tsidu, K. Schäfer, M. K. Sha, and J. Orphal. Application of portable ftir spectrometers for detecting greenhouse gas emissions of the major city berlin. *Atmospheric Measurement Techniques*, 8:3059–3068, 2015. doi: 10.5194/amt-8-3059-2015. URL https://www.atmos-meas-tech.net/8/3059/2015/. 94

[61] Klappenbach F., Bertleff M., Kostinek J., Hase F., Blumenstock T., Agusti-Panareda A., Razinger M., and Butz A. Accurate mobile remote sensing of xco2 and xch4 latitudinal transects from aboard a research vessel. *Atmospheric Measurement Techniques*, 8:5023–5038, 2015. doi: 10.5194/amt-8-5023-2015.

[62] Wang W., Tian Y., Liu C., Sun Y., Liu W., Xie P., Liu J., Xu J., Morino I., Velazco V., A., T. Griffith D., W., Notholt J., and Warneke T. Investigating the performance of a greenhouse gas observatory in hefei, china. *Atmospheric Measurement Techniques*, 10:2627–2643, 2017. doi: 10.5194/amt-10-2627-2017. 94

[63] J. K. Hedelius, C. Viatte, D. Wunch, C. M. Roehl, G. C. Toon, J. Chen, T. Jones, S. C. Wofsy, J. E. Franklin, H. Parker, M. K. Dubey, , and P. O. Wennberg. Assessment of errors and biases in retrievals of xco2 , xch4 , xco, and xn2o from a 0.5 cm^{-1} resolution solar-viewing spectrometer. *Atmospheric Measurement Techniques*, 9:3527–3546, 2016. doi: 10.5194/amt-9-3527-2016,. 94

[64] Chen J., Viatte C., Hedelius J., K., Jones T., Franklin J., E., Parker H., Gottlieb E., W., Wennberg P., O., Dubey M., K., and Wofsy S., C. Differential column measurements using compact solar-tracking spectrometers. *Atmos. Chem. Phys.*, 16:8479–8498, 2016. doi: 10.5194/acp-16-8479-2016. 94, 100

[65] M. Gisi, F. Hase, S. Dohe, T. Blumenstock, A. Simon2, and A. Keens. Xco2-measurements with a tabletop fts using solar absorption spectroscopy. *Atmospheric Measurement Techniques*, 5:2969–2980,, 2012. doi: 10.5194/amt-5-2969-2012. 94

[66] Hase F., Frey M., Kiel M., Blumenstock T., Harig R., Keens A., and Orphal J. Addition of a channel for xco observations to a portable ftir spectrometer for greenhouse gas measurements. *Atmospheric Measurement Techniques*, 9:2303–2313, 2016. doi: 10.5194/amt-9-2303-2016. 95

[67] F. Hase, J. Hannigan, M. T. Coffey, A. Goldman, M. Höpfner, N. Jones, C. P. Rinsland, and S. Wood. Intercomparison of retrieval codes used for the analysis of high-resolution, ground-based ftir measurements. *Journal of Quantitative Spectroscopy and Radiative Transfer,*, 87:25–52, 2004. doi: 10.1016/j.jqsrt.2003.12.008. 95

[68] Rodgers C., D. and Connor B., J. Intercomparison of remote sounding instruments. *Journal of Geophysical Research*, 108:4116, 2003. doi: doi:10.1029/2002JD002299. 110

List of Figures

List of Tables